IMT School for Advanced Studies, Lucca

Lucca, Italy

Modeling and Simulation of a Class of Nonlinear Coupled Reaction-Diffusion Problems for Green Applications

PhD Program in Computer, Decision, and System Science

XXIX Cycle

By

Pietro Lenarda

2017

The dissertation of Pietro Lenarda is approved.

Program Coordinator: Prof. Rocco De Nicola, IMT School for Advanced Studies Lucca

Supervisor: Prof. Marco Paggi, IMT School for Advanced Studies Lucca

The dissertation of Pietro Lenarda has been reviewed by:

Prof. Mario Di Paola, University of Palermo

Prof. Giorgio Zavarise, University of Salento

IMT School for Advanced Studies, Lucca

2017

Contents

Acknowledgements

The author would like to acknowledge the European Research Council for the support to the ERC Starting Grant "Multi-field and multi-scale Computational Approach to Design and Durability of PhotoVoltaic Modules" - CA2PVM, under the European Union's Seventh Framework Programme (FP/2007-2013)/ERC Grant Agreement n. 306622, which has partially supported the present research. The author would also like to acknowledge Prof. Ricardo Ruiz-Baier from the University of Oxford, for the opportunity to learn novel techniques and methods for numerical simulations in multi-physics during a visiting period to the Mathematical Institute of Oxford. Finally, I would like to express my thanks to my thesis advisor, Prof. Marco Paggi, who has inspired me in my studies .

Vita

November 4, 1986	Born, Florence, Italy
2010	Bachelor's Degree in Mathematics University of Florence
2013	Master in Applied Mathemathics University of Florence

Publications

1. P. Lenarda, M. Paggi, "A geometrical multi-scale numerical method for coupled hygro- thermo-mechanical problems in photovoltaic laminates," in *Computational Mechanics*, vol. 57, pp.947–963, 2016.
2. P. Lenarda, M. Paggi, "A fully implicit thermo-visco-elastic finite element formulation for thermo-rheologically complex polymers based on fractional calculus," in *Proceedings of the 11th Congress on Thermal Stresses, June 5-9, 2016, Salerno, Italy*, pp.150–154, ISBN: 978-88-99509-14-9, 2016.
3. M. Gagliardi, P. Lenarda, M. Paggi, "A reaction-diffusion formulation to simulate EVA polymer degradation in environmental and accelerated ageing conditions Solar Energy Materials and Solar Cells," in *Solar Energy Materials and Solar Cells*, in publication.
4. A. Gandolfi, P. Lenarda, "A note on Gibbs and Markov random fields with constraints and their moments," in *Mathematics and Mechanics of Complex Systems*, in publication.
5. P. Lenarda, R. Ruiz-Baier, M. Paggi "Partitioned coupling of advection-diffusion-reaction systems and Brinkman flows," in *Journal of Computational Physics*, under review.

Abstract

The present research regards the development of novel numerical methods for the solution of a large class of problems in the field of generalized thermo-diffusion in visco-elasticity and in advection-reaction-diffusion systems in incompressible Brinkman flows. Challenges in these complex physico-mathematical problems regard the strong nonlinearities involved, as well as the presence of dynamical behaviours characterized by very different time scales. To deal with these problems efficiently, splitting-operator time integration techniques are explored in order to decouple the dynamics of the various physical phenomena and compared with fully monolithic strategies. The analysis has played a new incisive role to make simulations and predictions in many applicative problems in which a multi-physic approach is needed to capture fully coupled effects. Applications are the simulation of the thermo-rheologically complex behaviour of the relaxation properties of materials with memory, the chemical degradation process due to aging and moisture diffusion in polymers, bioconvection in porous media of oxytactic bacteria and fingering instabilities of exothermic fronts in incompressible viscous fluids.

Chapter 1

Introduction and state of the art

1.1 Splitting methods for coupled multi-field problems

Time stepping algorithms for coupled problems in multi-physics can be divided in two classes (Gei11; FA92): (1) Fully monolithic schemes, in which the time stepping algorithm is applied to the full evolution problem and in general, if an implicit scheme is applied, they do guarantee unconditional stability of the solution. (2) Staggered schemes, in which the coupled system is partitioned according to the different coupled fields and each sub-problem is solved separately.

Despite their unconditional stability property, monolithic schemes can lead to very large non-symmetric systems and do not take advantage of the different time scales involved in the problem. Staggered schemes are aimed to circumvent this drawback. On the other hand, operator-splitting is not always possible, especially if the coupling between the physical phenomenon described by two or more systems is too strong. In this case, the monolithic approach is the only possible feasible method.

Consider an abstract evolution problem of the form:

$$\partial_t \boldsymbol{\chi} = A\boldsymbol{\chi} \tag{1.1.1}$$

where A is a differential linear or nonlinear operator applied to the vector $\boldsymbol{\chi} = (\boldsymbol{\chi}_1, \boldsymbol{\chi}_2)^T$. Suppose that the dynamics can be splitted in a sum $A\boldsymbol{\chi} = A_1\boldsymbol{\chi}_1 + A_2\boldsymbol{\chi}_2$. The operators A_1 and A_2 define the sub-problems: $\partial_t \boldsymbol{\chi}_1 = A_1\boldsymbol{\chi}_1$ and $\partial_t \boldsymbol{\chi}_2 = A_2\boldsymbol{\chi}_2$. A straightforward splitting strategy to solve numerically Eq. (1.1.1) at each time step t^{n+1} consists in:

1. Given $\boldsymbol{\chi}^n$ at time t^n, solve the sub-problem for $\boldsymbol{\chi}_1^{n+1}$ defined by:

$$\frac{\boldsymbol{\chi}_1^{n+1} - \boldsymbol{\chi}_1^n}{\Delta t} = A_1\boldsymbol{\chi}_1^{n+1}. \tag{1.1.2}$$

2. Given $\boldsymbol{\chi}_1^{n+1}$ the solution of (1.1.2), solve the sub-problem for $\boldsymbol{\chi}_2^{n+1}$

$$\frac{\boldsymbol{\chi}_2^{n+1} - \boldsymbol{\chi}_2^n}{\Delta t} = A_2\boldsymbol{\chi}_2^{n+1}. \tag{1.1.3}$$

Depending on the specific dynamical structure of each sub-problem, suitable solvers can be employed, so that they can be joined together to form the global solution algorithms. Unfortunately, the expense in adopting a splitting scheme instead of solving the fully monolithic problem is that this strategy can lead to conditional stability only. In some cases the unconditional stability can be obtained as well. As an example, consider the coupled system of linear thermo-elasticity:

$$\begin{aligned} &\rho\frac{\partial^2 \boldsymbol{u}}{\partial t^2} - \operatorname{div}\left(\mathbf{C}\boldsymbol{\varepsilon}(\mathbf{u}) - \beta(T - T_0)\,\mathbf{I}\right) = \mathbf{0}, \\ &\rho c\frac{\partial T}{\partial t} + T_0\beta \operatorname{div}\left(\frac{\partial \boldsymbol{u}}{\partial t}\right) = k\Delta T, \end{aligned} \tag{1.1.4}$$

where $\boldsymbol{u}$ is the displacement field, T is the temperature inside the material, ρ is the density of the material, $\mathbf{C}$ is the linear elasticity tensor, ε is the strain tensor for small displacements, T_0 is the initial temperature, β is the coupling parameter, c is the heat capacity and k is the thermal conductivity of the material and finally the symbol Δ stands for the Laplacian operator. Setting the state vector $\boldsymbol{\chi} = (\dot{\boldsymbol{u}}, \boldsymbol{u}, T)^T$, the operatior A

defining the dynamics is given by:

$$A\boldsymbol{\chi} = \begin{pmatrix} \dot{\mathbf{u}} \\ \frac{1}{\rho}\text{div}\left(\mathbf{C}\boldsymbol{\varepsilon}(\mathbf{u}) - \beta(T - T_0)\,\mathbf{I}\right) \\ \frac{k}{c}\Delta T - \frac{\beta}{c}\,\text{div}\left(\dot{\mathbf{u}}\right) \end{pmatrix}. \tag{1.1.5}$$

The operator A can be splitted in the sum $A\boldsymbol{\chi} = A_1\boldsymbol{\chi}_1 + A_2\boldsymbol{\chi}_2$, where:

$$A_1\boldsymbol{\chi}_1 = \begin{pmatrix} \dot{\mathbf{u}} \\ \frac{1}{\rho}\text{div}\left(\mathbf{C}\boldsymbol{\varepsilon}(\mathbf{u}) - \beta\theta\,\mathbf{I}\right) \\ -\frac{\beta}{c}\,\text{div}\left(\dot{\mathbf{u}}\right) \end{pmatrix},\ A_2\boldsymbol{\chi}_2 = \begin{pmatrix} \mathbf{0} \\ \mathbf{0} \\ \frac{k}{c}\Delta T \end{pmatrix}, \tag{1.1.6}$$

and this leads to two sub-problems of the form (1.1) to be solved sequentially. Simo and Armero proved in (FA92) that choosing unconditionally stable algorithms to solve each sub-problem definend by A_1 and A_2, the global algorithm is unconditionally stable.

Splitting schemes can be constructed for coupled problems exhibiting multiple time scales (Gei11). As an example, consider a nonlinear coupled reaction-diffusion problem defined as:

$$\begin{aligned} \frac{\partial u_1}{\partial t} - \text{div}\left(k(u_1, u_2)\nabla u_1\right) = 0, \\ \frac{\partial u_2}{\partial t} - \text{div}\left(\frac{1}{\varepsilon}k(u_1, u_2)\nabla u_2\right) = 0, \end{aligned} \tag{1.1.7}$$

where the diffusion matrix is given by:

$$\boldsymbol{D}(\mathbf{u}) = \begin{pmatrix} k(u_1, u_2) & 0 \\ 0 & \frac{1}{\varepsilon}k(u_1, u_2) \end{pmatrix},$$

being $\varepsilon \ll 1$ so that the diffusion process involving u_2 (fast dynamics) is much faster than that of u_1 (slow dynamics). In other words, the diffusion process of u_2 is almost stationary as compared to u_1. The formalization of this physical observation leads to the following splitting:

1. Given u_1^n, solve the stationary problem for the fast variable u_2^{n+1}:

$$-\text{div}\left(\frac{1}{\varepsilon}k(u_1^n, u_2^{n+1})\nabla u_2^{n+1}\right) = 0 \tag{1.1.8}$$

2. Then solve for the problem for the slow variable u_1^{n+1}:

$$\frac{u_1^{n+1} - u_1^n}{\Delta t} - \text{div}\left(k(u_1^{n+1}, u_2^{n+1})\nabla u_1^{n+1}\right) = 0 \tag{1.1.9}$$

1.2 Thermo-diffusion in visco-elasticity with applications to photovoltaics

The research activity in the field of visco-elasticity is due to the large scale utilization of polymeric materials in industial applications. The first part of this dissertation is focused on studing a class of coupled problems in the field of generalized thermo-diffusion in visco-elasticity, with particular focus on photovoltaic (PV) materials. Typical PV modules are laminates made of a thick glass superstrate, an encapsulating polymer (usually ethylene vinyl acetate, EVA), a layer of interconnected Silicon solar cells, another layer of EVA, and finally a polymeric protective backsheet. The polymer Ethylene Vinyl Acetate (EVA) is used to encapsulate Silicon solar cells and protect them from moisture effects and from thermo-mechanical loading. In standard qualification tests, PV modules are exposed to severe ranges of temperatures between $40°\text{C}$ and $85°\text{C}$ and 85% of air humidity, so that an accurate modelling of the thermo-diffusive behaviour of polymers is needed to efficiently predict the stress and deformation as well as the diffusion of moisture and the chemical degradation process inside the material.

The mathematical theory of thermo-elasticity has a long story dating back from the work of Nowacki (Now86). Afterwards various authors as Gurtin (GFA10) and Sherief (She04) derived governing equations of generalized thermo-diffusion in which the fields of temperature and diffusion of matter are coupled with linear elasticity. The mechanical behaviour of polymers is characterized by a relaxation modulus of power-law type induced by the so called memory effect. In materials with memeory, the current state of stress not only depends on the current time, but on the whole deformation history up to the current time. Classical Maxwell or Kelvin-Voigt rheological models used so far generally assume that the relaxation modulus is a sum of several Maxwell

arms called a Prony series (Bow09). In order to approximate the experimentally observed power-law trend, a huge number of arms (and thus of model parameters) has to be taken into account. To significantly simplify the task of parameters identification, modelling the visco-elastic behaviour via fractional derivatives has been proved to be very effective (Mai10; MDP13; MDP11).

On the other hand, polymers like EVA display a strong thermo-visco-elastic constitutive response, with a variation of the elastic modulus of up to three orders of magnitude depending on temperature.

In treating problems involving polymers, it is a commmon assumption the so called time-temperature superposition principle (GM10; Chr13). This principle states that all the relaxation functions at any temperature T can directly be obtained from the same master curve at base temperature, T_{ref}, shifted in the time axis by a quantity a_T. This quantity is a material parameter and must be determined by fitting from experimental data (GN94; GM10; Chr13). Unfortunately, for materials like EVA, this fitting leads to poor results showing that the time-temperature superposition principle does not apply (PDS$^+$11; EU10). This is due to the fact that the EVA polymer contains semicristalline parts and its microstructure changes with temperature, udergoing phase transitions. Those materials are called thermo-rheologically complex (Bag91). Moreover, the EVA polymer suffers of thermo-photo-oxidative degradation, due to the prolonged exposure of photovoltaic (PV) installations to UV light, environmental agents and the high working temperature of the PV module leading to a deterioration of the optical properties of the encapsulant (yellowing and browning) and to permeability to moisture.

The theory of thermo-visco-elasticity in presence of mass transfer deals with the dynamics of a linear visco-elastic structure coupled with heat transfer and the diffusion of a number of chemical species. The coupled system of thermo-diffusion in visco-elasticity takes place inside a bounded domain $\Omega \subset \mathbb{R}^3$ occupied by the material body in its undeformed configuration. Let $\boldsymbol{u} = (u_1, u_2, u_3)^T$, T and $\boldsymbol{c} = (c_1, \ldots, c_m)$ be respectively the displacement field, temperature and a vector of m chemical species diffusing inside the volume during the time interval

$0 \leq t \leq t_f$. The equations of generalized thermo-visco-elastic diffusion are (cfr. (GFA10; She04; Chr13)):

$$\begin{aligned}
&\rho \frac{\partial^2 \boldsymbol{u}}{\partial t^2} - \mathbf{div}(\boldsymbol{\sigma}) = \rho \boldsymbol{F}, \\
&\rho c \frac{\partial T}{\partial t} + T_0 \beta \operatorname{div}\left(\frac{\partial \boldsymbol{u}}{\partial t}\right) + T_0 \boldsymbol{a}_1 \cdot \frac{\partial \boldsymbol{c}}{\partial t} = k \Delta T + Q, \\
&\frac{\partial \boldsymbol{c}}{\partial t} - \mathbf{div}\left(\boldsymbol{D} \nabla \boldsymbol{c}\right) + \boldsymbol{\beta} \Delta \operatorname{div}(\boldsymbol{u}) + \boldsymbol{a}_2 \Delta T = \boldsymbol{G},
\end{aligned} \tag{1.2.1}$$

where ρ is the density of the material, $\boldsymbol{F} = (F_1, F_2, F_3)^T$ is a body force vector, c is the heat capacity of the material, β is the thermal stress coupling factor, T_0 is the initial temperature, $\boldsymbol{a}_1, \boldsymbol{a}_2$ are the coupling vector between temperature and concentration, k is the thermal conductivity, $Q(\boldsymbol{c}, T)$ is the heat generated by chemical reactions, $\boldsymbol{\beta} = (\beta_1, \ldots, \beta_m)^T$ is the coupling vector between concentration and stress , $\boldsymbol{D}$ is the diffusion matrix and $\boldsymbol{G}(\boldsymbol{c}) = (G_1(\boldsymbol{c}), \ldots, G_m(\boldsymbol{c}))^T$ is the reaction vector containing the kinetics of the chemical species.

Assuming that the material is isotropic, the stress tensor is given by (see (GFA10), (She04), (Chr13)):

$$\boldsymbol{\sigma}(\boldsymbol{c}, T) = \int_0^t \mathbf{C}\left(\tau(t-s, T)\right) \dot{\boldsymbol{\varepsilon}}(s) \mathrm{d}s - (\beta(T - T_0) - \boldsymbol{\beta} \cdot \boldsymbol{c})\mathbf{I}, \tag{1.2.2}$$

where $\boldsymbol{\varepsilon}$ is the infinitesimal strain tensor, $\mathbf{C}$ is the fourth order visco-elasticity tensor and the function $\tau(t, T)$ is an internal variable depending on time and temperature and assuming the phisyical dimensions of a (reduced) time, taking into account relaxation effects on the material properties due to temperature.

The first two equations in (1.2.1) together with the constitutive relation (1.2.2) define the dynamics of a thermo-visco-elastic body (She04), (Chr13). The second and third equations in (1.2.1) represent a coupled system for temperature and the m diffusing species (moisture, oxygen, etc.) inside the volume. The generated heat $Q(\boldsymbol{c}, T)$, the diffusion matrix $\boldsymbol{D}(\boldsymbol{c}, T)$ and the reaction vector $\boldsymbol{G}(\boldsymbol{c}, T)$ depend both on temperature and the concentration vector $\boldsymbol{c}$ leading to a nonlinear reaction-diffusion system.

In all the applications in the sequel of this dissertation, it will be assumed that $\boldsymbol{a}_1, \boldsymbol{a}_2, \boldsymbol{\beta} \approx \mathbf{0}$, so that the stress tensor is weakely coupled with the vector $\boldsymbol{c}$ of chemical species. As a result, the first and the third equations in (1.2.1) are basically uncoupled. The reason for this assumption is that equations in (1.2.1) will be employed in modelling materials that are typically used as encapsulants in PV modules for preventing infiltration of moisture ingress from the environment, so that the mass transfer process does not influence the mechanical deformation of the body.

An important feature of the problems that are going to be studied in the first part of this dissertation is that the set of equations (1.2.1) presents very different time scales. In general, the thermo-mechanical process is typically much faster than the reaction-diffusion dynamics involving the chemical species, whose products manifest a significant contribution in long times scenarios. This physical consideration allows using several splitting numerical techniques as it will be shown later on.

In Chapter 2, the partial differential equations describing a thermo-viscoelastic structure are presented in the framework of fractional calculus. Using the theory of Mittag-Leffler special functions (see (Mai10; RS11)), explicit expressions of the time and temperature dependency of the material properties characterizing the relaxation behaviour of the polymer in three dimensions and entering the visco-elasticity tensor $\mathbf{C}$ are derived. Moreover, it will be provided a new constitutive formulation to model thermo-rheological complexity, where the time- temperature superposition principle does not apply. To this purpose, it will be defined a new material function $\tau(t, T)$, depending on time and temperature history, taking into account the change in the microstructure of the polymer caused by temperature variations. The proposed model, numerically discretized by the Grünwald-Letnikov approximation (Mai10; RS11; AS02), is implemented within a finite element framework. Numerical examples are given to show the capability of the numerical model to represent the relaxation behaviour of material properties of polymers induced by thermal effects.

In Chapter 3 a computational framework for the simulation of cou-

pled thermo-diffusive problems in photovoltaic laminates is proposed. The governing equations describing the thermo-visco-elastic response of a laminate structure made of linear elastic homogeneous and isotropic layers separated by polymeric thermo-visco-elastic laminae are derived. The polymeric layers are modelled using zero-thickness internal interfaces with suitable traction-separation relations accounting for the thermo-visco-elastic properties of EVA (see (RB13)). While the coupled thermo-mechanical problem takes place in the three-dimensional space of the laminate, moisture diffusion occurs in a two-dimensional domain represented by the polymeric layers. A geometrical multi-scale splitting solution strategy is pursued by solving the partial differential equations governing heat transfer and thermo-elasticity in the three-dimensional space and the partial differential equation for moisture diffusion in the two dimensional domain. The thermo-elastic problem, which is much faster than moisture diffusion, is solved first via a fully implicit solution scheme in space and time. Temperature T obtained by solving the 3D thermo-mechanical probem is then used to calculate the diffusivity $D(T)$ of a 2D diffusion problem for moisture. The application of the proposed method to photovoltaic modules shows that moisture diffusion with a temperature dependent diffusivity is a much slower process than in the case of a constant diffusion coefficient (Kem14).

In Chapter 4 it is introduced a mathematical model to study the degradation process of the EVA polymer from the chemical view-point. This can be formulated as a reaction-diffusion problem involving temperature T and a vector of chemical species $\boldsymbol{c}$ of the form:

$$\begin{aligned} \rho c \frac{\partial T}{\partial t} - k\Delta T &= Q(\boldsymbol{c}, T), \\ \frac{\partial \boldsymbol{c}}{\partial t} - \mathbf{div}\left(\boldsymbol{D}\left(\boldsymbol{c}, T\right)\nabla \boldsymbol{c}\right) &= \boldsymbol{G}(\boldsymbol{c}, T). \end{aligned} \tag{1.2.3}$$

A computational framework based on the finite element method is proposed to simulate the chemical reactions and diffusion processes occurring in Poly(ethylene-co-vinyl acetate) (EVA) due to aging. The derived finite element procedure, specifically distinguished for the case of environmental degradation or accelerated aging, represents a comprehensive

tool for the prediction of the spatio-temporal evolution of the chemical species in the encapsulant, and the assessment of the lost of physico-chemical properties. The method allows to quantitatively compare the degradation resulting from any environmental condition to that from accelerated aging tests, providing a method to design new testing protocols tailored for specific climate zones.

1.3 Advection-reaction-diffusion systems in Brinkman flows

The second part of this thesis deals with the equations describing a stationary incompressible viscous flow (such as Stokes-Darcy, or Brinkman equations) coupled with an advection-reaction diffusion systems (JK13a; HA13; CBW14). A fairly large class of problems in science and engineering assume such a particular structure, as it is one of the basic forms of representing systems where physical, biological, and chemical processes exhibit a remarkable interaction. Notable examples are the density fingering of exothermic fronts in Hele-Shaw cells (SK04), where hydrodynamic instabilities are strongly influenced by the chemical reactions taking place at different spatial and temporal scales; convection-driven Turing patterns generated using Schnackenberg-Darcy models (MM97); reversible reactive flow and viscous fingering in chromatographic separation (HA13; LP94); plankton dynamics (C.L01); forced-convective heat and mass transfer in fibrous porous materials (CBW14); or the bioconvection in porous suspensions of oxytactic bacteria (VA16; HP96; JK13a). Phenomena of this kind are also relevant in so-called doubly-diffusive flows (Ac13; JK13b; LP00; QSM16), where convective effects are driven by two different density gradients having diverse rates of diffusion.

The coupled system of interest takes place in a bounded domain $\Omega \subset \mathbb{R}^3$, It can be derived from basic principles of mass, momentum, and energy conservation, and it is written in terms of the fluid velocity $\boldsymbol{u} = (u_1, \ldots, u_d)^T$, the rescaled vorticity $\boldsymbol{\omega}$ (vector $(\omega_1, \omega_2, \omega_3)^T$ if $d = 3$, or scalar ω if $d = 2$), the pressure p, and a vector $\boldsymbol{c} = (c_1, \ldots, c_m)^T$ of volumetric fraction or total dissolved concentration of m distinct substances:

For a.e. $(\boldsymbol{x}, t) \in \Omega_T := \Omega \times [0, T]$,

$$\begin{aligned} \partial_t \boldsymbol{c} + (\boldsymbol{u} \cdot \nabla)\boldsymbol{c} - \mathbf{div}(\boldsymbol{D}(\boldsymbol{c})\nabla \boldsymbol{c}) &= \boldsymbol{G}(\boldsymbol{c}), \\ \sigma \boldsymbol{u} + \sqrt{\mu}\, \mathbf{curl}\, \boldsymbol{\omega} + \nabla p &= \rho \boldsymbol{F}(\boldsymbol{c}), \\ \boldsymbol{\omega} &= \sqrt{\mu}\, \mathbf{curl}\, \boldsymbol{u}, \\ \operatorname{div} \boldsymbol{u} &= 0, \end{aligned} \tag{1.3.1}$$

where ρ, μ are respectively the fluid density and viscosity, σ is inverse permeability tensor, $\boldsymbol{F}$ represents the force exerted by the species on the fluid motion, encoding also external forces, $\boldsymbol{D}$ is a (generally nonlinear) cross-diffusion matrix, and $\boldsymbol{G}$ contains the reaction kinetics (representing production and degradation) of the species. The first and second equations in (1.3.1) are typically called generalized Stokes or Brinkman problem for a viscous incompressible fluid (see for instance (Gat14)). The convective term $(\boldsymbol{u} \cdot \nabla)\, \boldsymbol{c}$ is a vector whose components are:

$$\left((\boldsymbol{u} \cdot \nabla)\, \boldsymbol{c}\right)_I = \sum_{J=1}^{3} u_J \frac{\partial c_I}{\partial x_J}, \quad 1 \leq I \leq m. \tag{1.3.2}$$

In Chapter 5 it is presented a partitioned algorithm aimed at extending the capabilities of existing solvers for the simulation of advection-diffusion-reaction systems and incompressible flow. The space discretization of the governing equations is based on mixed finite element methods defined over unstructured meshes, whereas the time integration hinges on an operator splitting strategy that exploits the differences in scales between the reaction, advection, and diffusion processes, considering the system as a number of sequentially linked sets of partial differential, and algebraic equations. The flow solver presents the advantage that all unknowns in the system (here vorticity, velocity, and pressure) can be fully decoupled and thus the overall scheme turns out to be very attractive from the computational perspective. The robustness of the proposed method is illustrated with a series of numerical tests in 2D and 3D, relevant in the modelling of bacterial bioconvection and Boussinesq systems.

Chapter 2

Fractional models in thermo-visco-elasticity

The theory of visco-elasticity deals with the description of materials that exhibit a combination of elastic (able to recover the original shape after stress application) and viscous (deformation-preserving after stress removal) behaviour. Quantitative description of such materials involves a strain-stress relation that depends on time. The classical linearized model leads to an integro-differential equation in which the elastic stress tensor σ is a convolution product of the strain ε, which encodes the deformation history of the material up to the current time, with an appropriate memory kernel $E(t)$ (in one dimension), representing the relaxation mechanism:

$$\sigma(t) = \int_0^t E(t-s)\dot{\varepsilon}(s)\,\mathrm{d}s. \tag{2.0.1}$$

The visco-elastic response characteristics of a material are determined often using creep and relaxation tests. In a relaxation test, a constant strain ε_0 is applied quasi-statically to a uniaxial tensile bar at zero time, if a visco-elastic material (which is usually a polymer) is loaded in the described manner, the stress σ needed to maintain the constant strain will decrease with time exhibiting a typical power-law behaviour. The relaxation modulus of the polymer is defined as $E(t) = \sigma(t)/\varepsilon_0$. Another

fundamental characterization test for viscoe-lastic materials is the creep test in which a uniaxial tensile bar is loaded with a constant stress σ_0 at zero time. Again, the load is applied quasi-statically or in such a manner as to avoid inertia effects and the material is assumed to have no prior history. In this case, the strain ε under the constant load increases with time and the test defines a new quantity called the creep compliance $J(t) = \varepsilon(t)/\sigma_0$.

Various mathematical models have been proposed and used to represent the visco-elastic material functions analytically. The simplest mechanical models for viscoelastic behavior consist of two elements: a spring for elastic behavior and a damper for viscous behavior. Spring and damper elements can be combined in a variety of arrangements to produce a simulated viscoelastic response. Early models due to Maxwell and Kelvin combine a linear spring in series or in parallel with a Newtonian damper (see (Bow09)):

$$k + \eta \frac{D\sigma}{Dt} = k\eta \frac{D\varepsilon}{Dt} \qquad \text{(Maxwell)},$$
$$\sigma = k\varepsilon + \eta \frac{D\varepsilon}{Dt} \qquad \text{(Kelvin-Voigt)}.$$

Other basic arrangements include the three-parameter solid and the four-parameter fluid. A more versatile model is obtained by connecting a number N of Maxwell elements (arms) in series and adding a spring in parallel, leading to relaxation function of the form of a Prony series:

$$E(t) = E_0 + \sum_{i=1}^{n} E_i \exp(-t/\tau_i), \tag{2.0.2}$$

where $E_i, \tau_i > 0$ are constants to be determined from data. It has to be pointed out that constants E_i, τ_i in the Prony series has to be fitted from real data obtained from realxation tests. This is not a straight forward task because it involves the solution of a constrained optimization problem (PDS$^+$11; EU10).

Fractional calculus has been proved to be very effective in modelling the power-law time-dependency of the relaxation behavior of polymers, with an easier parameters estimation as compared to generalized Maxwell

rheological models (MP15; MDP11; EL99). The pioneer in application of fractional calculus to the analysis of viscoelasticity, as noted by Bagley and Torvik (Bag91), was Nutting, who established in 1921 that for many composite materials the relationship between the stress and the deformation is described by an equation of the form:

$$\sigma(t) = At^{-\alpha}\varepsilon(t), \qquad 0 \leq \alpha \leq 1. \tag{2.0.3}$$

If the relaxation modulus $E(t)$ in Eq. (2.0.1) is assumed to be a fractional kernel function depending on parametres $A > 0$, $0 \leq \alpha \leq 1$ of the type:

$$E(t) = A\, t^{-\alpha}/\Gamma(1-\alpha), \tag{2.0.4}$$

where $\Gamma(x)$ is the Euler gamma function. In this case the constitutive relation (2.0.1) reduces to an elastic spring for $\alpha = 0$ or to a dashpot for $\alpha = 1$, suggesting that visco-elasticity is something in between those two constituive models. This is the reason why the stress-strain relation (2.0.1) is usually called a spring-pot element (Koe84; AS02) (see Fig. 1). The fractional derivative of a function $f(t)$ of order $0 \leq \alpha \leq 1$ is defined

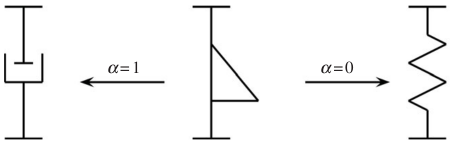

Figure 1: Schematic representation of a spring-pot element for $1 < \alpha < 1$.

as (Mai10):

$$D^{\alpha} f(t) = \frac{1}{\Gamma(1-\alpha)} \int_0^t (t-s)^{-\alpha} \dot{f}(s)\, \mathrm{d}s. \tag{2.0.5}$$

Adopting this notation, the constitutive relation (2.0.1) can be rewritten in terms of fractional derivative as ((AE03; Koe84; Fab14; DLWZ15)):

$$\sigma(t) = AD^{\alpha}\varepsilon(t). \tag{2.0.6}$$

In three dimensions the material functions characterizing completely the response of a visco-elastic solid are the Young modulus $E(t)$, the

bulk modulus $K(t)$ and the shear modulus $G(t)$. The Young modulus is considered to be of fractional type (2.0.4) as in (MP15). Following (HS96), the assumption of constant bulk modulus $K(t) \equiv K$ is made. This is because polymer materials are known to show a predominant visco-elastic behaviour in shear deformation rather than in volumetric expansion. The remaining shear modulus $G(t)$ is found via elastic visco-elastic correspondence principle and inverse Laplace transform using the Mittag-Leffler special functions (SMH11).

On the other hand, polymers display a strong thermo-visco-elastic constitutive response, with a variation of the material properties of up to three orders of magnitude depending on temperature (MP15), (EU10), (PDS$^+$11). In treating problems involving polymers it is a commmon assumption the so-called time-temperature superposition principle (Bow09; GM10; FL02; GN94). This principle states that all the material visco-elastic functions at any temperature T can directly be obtained from the same curve, the so-called mastercurve, at base temperature T_{ref} shifted in the time axis by a quantity a_T. This quantity is a material parameter and must be determined by fitting from experimental data. Unfortunately, for a large class of materials this fitting leads to poor results showing that the time-temperature superposition principle does not apply (EU10; PDS$^+$11). Those materials are called thermo-rheologically complex (EL99), (GM10).

Later on in this Chapter it will be provided a new constitutive formulation to model thermo-rheological complexity, where the time-temperature superposition principle is substitued by a new material function $\tau(t, T)$, dependending on time and temperature history, taking into account the change in the microstructure of the polymer caused by temperature variations which is responsable of the shifting of the material function.

2.1 Constitutive equations in three dimensions

Let us consider a material occupying a region $R \subset \mathbb{R}^3$ in the three-dimensional space. Let $u_I(x_1, x_2, x_3, t)$, $1 \leq I \leq 3$ be the components

of the displacement field. Let:

$$\varepsilon_{IJ} = \frac{1}{2}\left(\frac{\partial u_I}{\partial x_J} + \frac{\partial u_J}{\partial x_I}\right), \quad 1 \leq I, J \leq 3 \tag{2.1.1}$$

be the infinitesimal strain tensor. It is typical of polymers to show a visco-elastic behavior mostly in shear rather than in dilatation. Assume that the material is isotropic, then decomposing the overall stress tensor σ_{IJ} into its deviatoric and hydrostatic parts, a visco-elastic behavior only for the deviatoric part it is considered. The split of the stress tensor σ_{IJ} reads:

$$S_{IJ}(t) = 2\int_0^t G(t-s)\frac{\partial e_{IJ}(s)}{\partial t}\,\mathrm{d}s, \quad \sigma_{JJ}(t) = 3K\varepsilon_{JJ} \tag{2.1.2}$$

where $S_{IJ} = \sigma_{IJ} - \sigma_{KK}\delta_{IJ}/\ 3$ and $e_{IJ} = \varepsilon_{IJ} - \varepsilon_{KK}\delta_{IJ}/\ 3$ are the deviatoric components of the stress and strain tensors, $G(t)$ is the shear modulus and $K(t) \equiv K$ is the constant bulk modulus. The visco-elastic constitutive model (2.1.2) is of Kelvin-Voigt type.

In the solution of the three-dimensional visco-elastic problem, it is necessary to know the actual mathematical expression of the three material functions, the shear, bulk and Young modulus G, K, E and their dependency on time. Following (MP15), a Young modulus of fractional type is considered:

$$E(t) = A\ t^{-\alpha}/\Gamma(1-\alpha), \quad 0 \leq \alpha \leq 1. \tag{2.1.3}$$

Given the espression of the Young modulus $E(t)$, an explicit time-dependency of the shear modulus $G(t)$ is now obtained.

Let f be a function and denote with $\mathcal{L}[f]$ its Laplace transform. The s-multiplied Laplace transform given by $s \cdot \mathcal{L}[f]$ is denoted as $\overline{f}^*(s)$. The elastic-viscoelastic correspondence principle (Bri08) states that, in the Laplace domain, the shear modulus is given by:

$$\overline{G}^*(s) = \frac{3\overline{E}^*(s)\overline{K}^*(s)}{9\overline{K}(s) - \overline{E}^*(s)}, \tag{2.1.4}$$

Then, because $K(t) \equiv K$ and $E(t)$ is given by (2.1.3), in the Laplace

domain $\overline{K}^*(s) = K/s$ and $\overline{E}^*(s) = A\ s^{\alpha-1}$. Substituting these espressions in Eq. (2.1.4) and taking the inverse Laplace transform, leads to:

$$G(t)/3 = -E_\alpha\left[-9Kt^\alpha/A\right] \tag{2.1.5}$$

where:

$$E_\alpha[x] = \sum_{k=0}^{\infty} \frac{x^k}{\Gamma(\alpha k + 1)} \tag{2.1.6}$$

is the Mittag-Leffler special function of order α (see (Mai10), (SMH11)). Since this function does not have a closed-form expression, for numerical purposes the asymptotic approximation is introduced:

$$E_\alpha[-\lambda t^{-\alpha}] \approx \begin{cases} 1 - \lambda \dfrac{t^\alpha}{\Gamma(1+\alpha)}, & t \to 0^+, \\ \dfrac{t^{-\alpha}}{\lambda\,\Gamma(1-\alpha)}, & t \to +\infty, \end{cases} \tag{2.1.7}$$

valid for any λ. From this expression (2.1.7) the formula found by Pipkin in (Pip12) is recovered:

$$G(t) \approx E(t)/3, \quad t \to +\infty, \tag{2.1.8}$$

which will be used in the sequel as the expression for the time-dependent shear modulus.

2.2 Limits of applicability of the t-t superposition principle

In treating problems involving polymers, the so-called time-temperature superposition principle is a commmon assumption. This principle states that all the relaxation functions $E(t,T), G(t,T)$ and $K(t,T)$ at any temperature T can directly be obtained from the material functions at base temperature T_{ref}, by replacing the current time t with a shift function a_T, which is a material property of the material and must, in general, be determined experimentally (GN94; Chr13; KF12):

$$E(t,T) = E(t/a_T, T_{ref}). \tag{2.2.1}$$

This is equivalent to say that, for any fixed temperature T, the relaxation curve $t \mapsto E(t,T)$ is obtained from the same master curve at a base temperature T_{ref}, shifted along the horizontal axis by a quantity a_T in a log time scale. The shift factor a_T is usually described by the WLF (Williams-Landel-Ferry) equation (FW52; Voi14):

$$\log(a_T) = \frac{-C_1(T - T_g)}{C_2 + (T - T_g)}, \tag{2.2.2}$$

where C_1, C_2 are constants and T_g is the glass transition temperature. Espression (2.2.2) is known to be valid only for $T > T_g$.

Materials where the shifting results in a satisfactory mastercurve are called thermo-rheologically simple. Unfortunately, this is not the case for materials like EVA (Ethylene-Vynil-Acetate), which is a copolymer containing semicrystalline parts and whose microstructure changes with temperature, udergoing several phase transitions (UE11),(MP15) . Those materials are called thermo-rheologically complex (Bag91).

The relaxation curves of the Young modulus $E(t,T)$ for Ethylen-Vynil-Acetate (EVA) at different temperatures in a log-log scale are shown in Fig. 2 (a) (MP15; PDS$^+$11). It can be noticed that the straight lines have different slopes in the temperature range under consideration, so that an horizontal shifting of the material function $E(t,T)$ for different temperatures T does not result in a satisfactory overlap. This result suggests that the shift factor a_T for the EVA material, as assumed by the time-temperature principle and described by (2.2.2), is not well defined. This point is confirmed looking at Figure 2(b) where the fitting of the shift factor (2.2.2) for Ethylene-Vynil-Acetate taken from (UE11) shows very poor result.

From this considerations it is evident that the time-temperature superposition principle does not apply for materials like EVA.

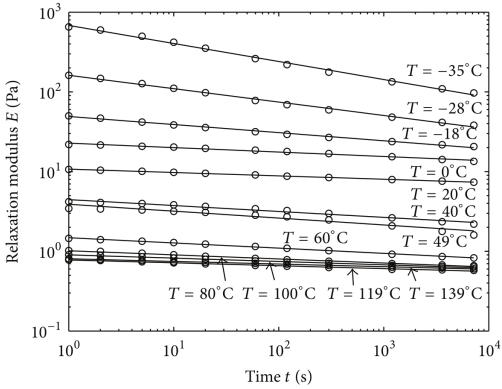

(a) Young modulus $E(t, T)$

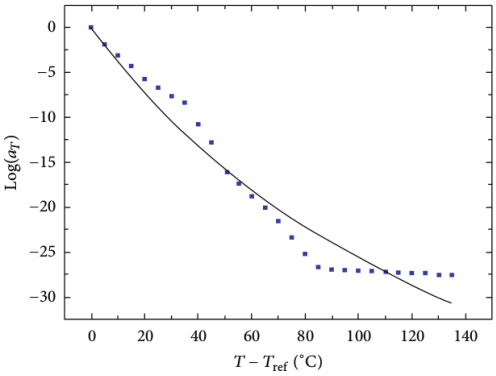

(b) Shift factor a_T

Figure 2: (a) Plots over time in a log-log scale of the Young modulus $E(t, T)$ obtained from relaxation tests at different temperatures in a range between $-35^\circ C$ and $139^\circ C$. (b) Fitting of the shift factor a_T (continuous line) for EVA (Etylen-Vynil-Acetate) using the WLF equation (2.2.2) (dot line).

2.3 A new model for thermo-rheological complexity

Following (MP15) a temperature dependency of the Young modulus is assumed as:

$$E(t,T) = A(T)t^{-\alpha(T)}/\,\Gamma(1-\alpha(T)), \tag{2.3.1}$$

where the material parameters $0 \leq \alpha(T) \leq 1$ and $A(T) \geq 0$ are now temperature dependent. Functions $\alpha(T)$ and $A(T)$ can be determined from Eq. (2.3.1), fitting data from uniaxial relaxation tests conducted for different temperatures. Using the asymptotic representation of the shear modulus as in (2.1.8) and (2.3.1) and substituing it in the first line of (2.1.2), leads to the following integral, describing the relaxation behavior of the material properties induced by thermal effects:

$$\frac{A(T)}{\Gamma(1-\alpha(T))}\int_0^t (t-s)^{-\alpha(T)}\frac{\partial e_{IJ}}{\partial t}(s)\,\mathrm{d}s. \tag{2.3.2}$$

This espression is not convenient for applications because both $\alpha(T)$ and $A(T)$ change continuously with temperature T and time t during the process, while we want to find an espression similar to (2.3.2) but having constant values of α and A as long as the internal micro-stucture of the polymer remains the same.

To this purpose a thermal material clock function is defined and an espression similar to (2.3.2), which is suitable for applications, is introduced.

Consider an arbitrary temperature history $T(t)$, depending on the thermo-visco-elastic process, let $\delta > 0$ be a given threshold. Let $\tau = \tau(t,T)$ be a function which is always smaller or equal to the current time t, which has the role of monitoring the temperature history inside the material. This function is nothing but a counter taking discrete values $0 = \tau_0, \ldots, \tau_k, \ldots$, that ticks when the temperature variation exceeds the threshold δ. At the beginning of the process $\tau = \tau_0 = 0$ and it remains zero untill the temperature variation inside the material does not exceeds δ. After that moment, the clock ticks and τ is set equal to a new value

$\tau = \tau_1$. In general, during the evolution of the process, there can be several of those temperature jumps, so that the value $\tau(t,T)$ at any time t is defined recursively as:

$$\begin{cases} \tau_0 & = 0 \\ \tau_k & = \inf_{\tau_{k-1} \le t' \le t} \left\{ |T(t') - T(\tau_{k-1})| > \delta \right\}. \end{cases} \tag{2.3.3}$$

Consider the reduced time defined as: $\tau(t,T) = \tau_k \chi_{[\tau_k,t)}(t)$, where $\chi_{(a,b)}$ is the indicator function of interval (a,b). The function $\tau(t,T)$ is a step function constant inside each interval $[\tau_{k-1},\tau_k]$. Define the modified material functions $A^\tau = A(T(\tau)) = A(\tau_k)\chi_{[\tau_k,t)}$ and $\alpha^\tau = \alpha(T(\tau)) = \alpha(\tau_k)\chi_{[\tau_k,t)}$ which are constants inside each interval $[\tau_{k-1},\tau_k]$. The modified relaxation kernel $g^\tau_{A,\alpha}(t)$ is defined as:

$$g^\tau_{A,\alpha}(t) = A^\tau (t-\tau)^{-\alpha^\tau}/\Gamma(1-\alpha^\tau). \tag{2.3.4}$$

This physical observation suggests that the correct formulation of the thermo-visco-elastic relaxation process (2.3.2) is well described by the following fractional-thermal derivative:

$$\mathcal{D}(A^\tau, \alpha^\tau, e_{IJ})(t) = \int_0^t g^\tau_{A,\alpha}(t-s)\dot{e}_{IJ}(s)\,\mathrm{d}s \tag{2.3.5}$$

Formula (2.3.5) basically says that when the variation of temperature inside the material exceeds the given threshold δ and the thermal clock $\tau = \tau_k$ ticks, the relaxation process is shifted backwards in time of a quantity $t - \tau_k$ and restarts with new parameters evaluated at $\alpha(T(\tau_k))$ and $A(T(\tau_k))$ for all subsequent times (see Fig. 2.3). This is because the material has experienced a phase transition and temperature has affected so significantely its internal microstructure to change dramatically its material properties. Using equation (2.1.2) and the approximation of the shear modulus in (2.1.8), the relaxation process for a thermo-rheologically complex material can be written as:

$$S_{IJ}(t) = \frac{2}{3}\int_0^t g^\tau_{A,\alpha}(t-s)\dot{e}_{IJ}(s)\,\mathrm{d}s = \frac{2}{3}\mathcal{D}(A^\tau, \alpha^\tau, e_{IJ})(t). \tag{2.3.6}$$

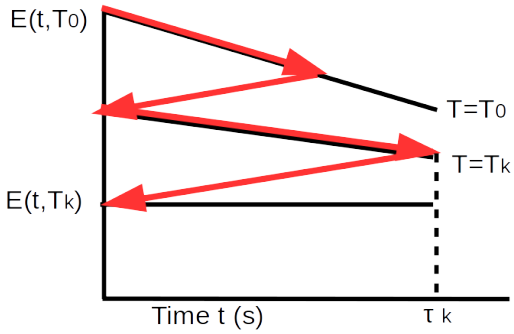

Figure 3: Schematic representation of the relaxation process of the material function $E(t,T)$ depending on the thermal history in a thermo-rheologically complex material.

Notice that if the process is adiabatic, i.e. the temperature $T(t)$ remains constant equal to the initial temperature T_0, during the time interval $[0,t_f]$, then $\alpha^\tau \equiv \alpha(T_0) \equiv \alpha$ and $A^\tau \equiv A(T_0) \equiv A$ are constants, the thermal clock is $\tau(t) \equiv 0$, so that $\mathcal{D}(A^\tau, \alpha^\tau, e_{IJ})(t)$ reduces to the usual fractional derivative:

$$AD^\alpha e_{IJ}(t) = \frac{A}{\Gamma(1-\alpha)} \int_0^t (t-s)^{-\alpha} \dot{e}_{IJ}(s)\, \mathrm{d}s. \tag{2.3.7}$$

As a concluding remark, the problem of defineing a reasonable way to estimate the threshold δ is adressed. This parameter defines a temperature interval in which the material properties A and α are constants. Looking at Fig. 2(a) it can be noticed that the slopes of the straight lines are the same in different temperature intervals, i.e., in $[-135°C, -28°C]$, $[-18°C, 20°C]$, $[40°C, 139°C]$. Each of those class of temperature intervals identify different values of α and A and a threshold δ can be defined accordingly.

2.4 Strong formulation of the coupled thermo-visco-elastic problem

Consider formulae (2.1.2) and (2.3.6) adding thermal effects, we can write the deviatoric and hydrostatic parts of the stress tensor as:

$$S_{IJ}(t,T) = \frac{2}{3}\mathcal{D}(A^\tau, \alpha^\tau, e_{IJ})(t), \tag{2.4.1}$$

$$\sigma_{JJ}(t,T) = 3K\varepsilon_{JJ} - 3\beta(T - T_0), \tag{2.4.2}$$

where β is the coupling thermal stress factor and T_0 is the initial tempertaure inside the material. Accordingly, the overall stress tensor is given by:

$$\sigma_{IJ}(t,T) = \frac{2}{3}\mathcal{D}(A^\tau, \alpha^\tau, e_{IJ})(t) + (K\varepsilon_{JJ} - \beta(T - T_0))\,\delta_{IJ}. \tag{2.4.3}$$

The balance of linear momentum takes the form:

$$\rho\frac{\partial^2 u_I}{\partial t^2} - \sigma_{IJ,J} = 0, \qquad \text{in } R \times [0, t_f],\ 1 \le I \le 3, \tag{2.4.4}$$

where ρ is the density of the material. As far as we concern the heat conduction process, the standard Fourier law is assumed for the heat flux q_I:

$$q_I = -k\frac{\partial T}{\partial x_I}, \quad 1 \le I \le 3 \tag{2.4.5}$$

where k is the thermal conductivity. Accordingly, the heat conduction equation reads:

$$k\nabla^2 T = \rho c\frac{\partial T}{\partial t} + \beta T_0\frac{\partial \varepsilon_{KK}}{\partial t}, \qquad \text{in } R \times [0, t_f],\ 1 \le I \le 3, \tag{2.4.6}$$

where c is the thermal conductivity of the material. Equations (2.4.4) and (2.4.6) represent the system of coupled linear thermo-viscoelasticity (see (KM12), (EEB15)).

2.5 Weak formulation

The weak form corresponding to the equation of linear momentum (2.4.4) is derived by multiplying it by a virtual displacement δv_I and integrat-

ing the result on the domain R. Applying the divergence theorem, we obtain:

$$\int_R \rho \frac{\partial^2 u_I}{\partial t^2} \delta v_I \, \mathrm{d}V + \int_R K \varepsilon_{KK} \delta \varepsilon_{IJ} \delta_{IJ} \, \mathrm{d}V + \int_R \frac{2}{3} \mathcal{D}(A^\tau, \alpha^\tau) e_{IJ} \delta \varepsilon_{IJ} \, \mathrm{d}V - \int_R \beta \delta \varepsilon_{IJ} \delta_{IJ} (T - T_0) \, \mathrm{d}V = \int_{\partial_N R^u} t_I \delta v_I \, \mathrm{d}A, \tag{2.5.1}$$

where the last integral takes into account the traction t_I imposed on $\partial_N R^u$ the Neumann part of the domain. Analogously, the weak form corresponding to the heat conduction partial differential equation (2.4.6) is obtained by multiplying it for a test function δT and integrating the result over R:

$$\int_R k \frac{\partial T}{\partial x_I} \frac{\partial \delta T}{\partial x_I} \, \mathrm{d}V + \int_R \rho c \frac{\partial T}{\partial t} \delta T \, \mathrm{d}V + \int_R \beta T_0 \frac{\partial \varepsilon_{IJ}}{\partial t} \delta_{IJ} \delta T \, \mathrm{d}V + \int_{\partial_N R^\theta} q_n \delta T \, \mathrm{d}A = 0, \tag{2.5.2}$$

where the q_n is the imposed normal heat flux $\partial T / \partial n = q_n$ imposed on the Neumann part of the domain $\partial_N R^\theta$.

2.6 Finite element formulation

Consider a decomposition of the domain R into a finite number of elements and let $\{\Phi_k(\xi_1, \xi_2, \xi_3)\}_{k=1}^{N_e}$ a basis of shape functions in a reference coordinate system $-1 \leq \xi_1, \xi_2, \xi_3 \leq +1$. At the element level, the displacement components and temperature are interpolated as:

$$u_I(x_1, x_2, x_3, t) = \sum_{k=1}^{N_e} \Phi_k(\xi_1, \xi_2, \xi_3) U_{kI}(t), \quad 1 \leq I \leq 3 \tag{2.6.1}$$

$$T(x_1, x_2, x_3, t) - T_0(x_1, x_2, x_3) = \sum_{k=1}^{N_e} \Phi_k(\xi_1, \xi_2, \xi_3) \Theta_k(t). \tag{2.6.2}$$

Setting nodal displacement and temperature vectors as:

$$\begin{aligned} \{U_e\} &= (U_{11}, U_{12}, U_{13}, \ldots, U_{1N_e}, U_{2N_e}, U_{3N_e})^T \\ \{\Theta_e\} &= (\Theta_1, \ldots, \Theta_{N_e})^T \end{aligned} \tag{2.6.3}$$

after substituing those expressions into the weak forms, the discretized weak forms become:

$$\sum_e \{\delta U_e\}^{\mathrm{T}}[M_e^{uu}]\frac{D^2\{U_e\}}{Dt^2} + \sum_e \{\delta U_e\}^{\mathrm{T}}[K_e^{uu}]\{U_e\} + \sum_e \{\delta U_e\}^{\mathrm{T}}[G_e^{u\theta}]\mathcal{D}(A^\tau,\alpha^\tau)\{U_e\} + \sum_e \{\delta U_e\}^{\mathrm{T}}[C_e^{u\theta}]\{\Theta_e\} = \sum_e \{\delta U_e\}^{\mathrm{T}}\{\bar{T}_e^u\},$$

$$\sum_e \{\delta \Theta_e\}^{\mathrm{T}}[K_e^{\theta\theta}]\{\Theta_e\} + \sum_e \{\delta \Theta_e\}^{\mathrm{T}}[C_e^{u\theta}]\frac{D\{\Theta_e\}}{Dt} + \sum_e \{\delta \Theta_e\}^{\mathrm{T}}[C_e^{u\theta}]\frac{D\{U_e\}}{Dt} + \sum_e \{\delta \Theta_e\}^{\mathrm{T}}\{\bar{Q}_e^\theta\} = 0.$$

If we adopt a fully monolithic approach to solve the coupled thermo-visco-elasticity problem, the generalized displacement vector is:

$$\{\Delta_e\} = (U_{11}, U_{12}, U_{13}, \Theta_1, \ldots, U_{1N_e}, U_{2N_e}, U_{3N_e}, \Theta_{N_e})^T, \tag{2.6.4}$$

then discretizing the time interval $[0, t_f]$ into $0 = t^0 \leq \cdots \leq t^n \leq t^N = t_f$ where $t^{n+1} = t^n + \Delta t$ the fully monolithic system of equations is:

$$[M]\frac{D^2}{Dt^2}\{\Delta\}^{n+1} + [C]\frac{D}{Dt}\{\Delta\}^{n+1} + [G]\mathcal{D}(A^\tau,\alpha^\tau)\{\Delta\}^{n+1} + [K]\{\Delta\}^{n+1} = \{F\}^{n+1} \tag{2.6.5}$$

where the global matrices and vectors result from the usual assembling of matrices at the element level. $[M]$ is the mass matrix, $[C]$ is the coupling thermo-mechanical matrix, $[G]$ and $[K]$ are the shear and bulk matrices and $\{F\}^{n+1}$ is the load vector.

2.7 Grünwald-Letnikov approximation

The problem of approximating the fractional derivative $\mathcal{D}(A^\tau,\alpha^\tau)\{\Delta\}^{n+1}$ is now adressed. Let $f(t)$ be a function defined in an interval $[0, T]$ and let $0 = t^0 \leq \cdots \leq t^n \leq t^N = T$ be a partition of $[0, T]$, where $t^{n+1} = t^n + \Delta t$.

Racalling the so called Grünwald-Letnikov approximation of the fractional derivative $D^\alpha f(t^{n+1})$ of order $0 \leq \alpha \leq 1$ of a f function (see also (AS02) (RS11), (Mai10), (MDP11), (WS01)):

$$\begin{aligned} D^\alpha f(t^{n+1}) \approx & (\Delta t)^{-\alpha} \sum_{j=0}^{n} c_{j+1}(\alpha) f(t^{n+1-j}) = \\ & (\Delta t)^{-\alpha} \left(f(t^1), \ldots, f(t^{n+1}) \right) \begin{pmatrix} c_{n+1}(\alpha) \\ \vdots \\ c_1(\alpha) \end{pmatrix}, \end{aligned} \tag{2.7.1}$$

where the coefficients $c_j(\alpha)$ are defined by the recursive formula:

$$c_j(\alpha) = \begin{cases} \dfrac{(j-1-\alpha)}{j} c_{j-1}(\alpha) & \text{if } j > 1 \\ 1 & \text{if } j = 1. \end{cases}$$

Coefficients (2.7) have the properties that $c_j(\alpha) < c_{j+1}(\alpha) < 0$ for $j > 1$ and $\lim_{j \to \infty} c_j(\alpha) = 0$. Notice that the dimensions of vectors in (2.7.1) are increasing with n. Each value $f(t^n)$ up to time t^{n+1} is contribuing to the final value of $D^\alpha f(t^{n+1})$, but the influence of the coefficients is weaker in the past rather than in the present and the initial value $f(t^0)$ is multiplied by $c_{n+1}(\alpha)$, which is tending to zero as n grows. This property of the Grünwald-Letnikov approximation is called memory effect.

With this set up the fractional-thermal derivative $\mathcal{D}(A^\tau, \alpha^\tau)\{\Delta\}^{n+1}$ is approximated as:

$$\mathcal{D}(A^\tau, \alpha^\tau)\{\Delta\}^{n+1} \approx A(T^m) \Delta t^{-\alpha(T^m)} \left(\{\Delta\}^{n+1} + \mathcal{F}_T^m \{\Delta\}^n \right) \tag{2.7.2}$$

where $m \leq n$ is an history variable depending on the current time t^n and temperature T^n, taking values $m_0 < m_1 < \cdots < m_k$, defined recursively as $m_0 = 0$ and:

$$m_k = \begin{cases} m_{k-1} & \text{if } |T^n - T^{n-1}| < \delta, \\ n & \text{otherwise,} \end{cases}$$

and the operator $\mathcal{F}_T^m \{\Delta\}^n$, collecting the displacement history up to time

n, is given by:

$$\mathcal{F}_T^m\{\Delta\}^n = \begin{cases} \sum_{j=m}^{n} c_{n+2-j}(\alpha(T^m))\{\Delta\}^j, & \text{if } m < n \\ \{0\}, & \text{if } m = n. \end{cases} \tag{2.7.3}$$

Notice that the last term in the sum (2.7.3) is $c_2(\alpha(T^m))\{\Delta\}^n$, because $c_1(\alpha(T^m)) = 1$ is associated to the unknown vector $\{\Delta\}^{n+1}$. When the process begins the sum starts to pile up following the Günwald approximation with material functions $A(T^0)$ and $\alpha(T^0)$ evaluated at the starting temperature T^0, untill the condition $|T^n - T^{n-1}| > \delta$ is verified. After that moment, m is setted equal to n and the process restarts with new material parameters $A(T^n)$ and $\alpha(T^n)$.

When the process is adiabatic, i.e. the temperature is constant during time, then $m = 0$ for all t^n and $A = A(T^0)$, $\alpha = \alpha(T^0)$, so that the approximation of the thermal-fractional derivative $\mathcal{D}(A^\tau, \alpha^\tau)\{\Delta\}^{n+1}$ reduces to $AD^\alpha\{\Delta\}^{n+1}$ the usual Günwald-Letnikov approximation, namely:

$$AD^\alpha\{\Delta\}^{n+1} \approx A(\Delta t)^{-\alpha}\left[\{\Delta\}^1|\dots|\{\Delta\}^{n+1}\right]\begin{pmatrix} c_{n+1}(\alpha) \\ \vdots \\ c_1(\alpha) \end{pmatrix}. \tag{2.7.4}$$

It is evident that the displacement history must be stored in a matrix that is increasing in the number of columns and represents the memory of the material.

2.8 Temporal discretization

Substituing the approximation of the fractional-thermal derivative given in (2.7.2) and (2.7.3) in (2.6.5) at time t^{n+1} we obtain:

$$[M]\frac{D^2\{\Delta\}^{n+1}}{Dt^2} + [C]\frac{D\{\Delta\}^{n+1}}{Dt} + [\overline{K}]^m\{\Delta\}^{n+1} = \{F\}^{n+1} - \{F_V\}^m, \tag{2.8.1}$$

where the modified stiffness matrix is:

$$[\overline{K}]^m = (\Delta t)^{-\alpha(T^m)}[G] + [K],$$

and the additional visco-elastic load vector is:

$$\{F_V\}^m = A(T^m)(\Delta t)^{-\alpha(T^m)}[G]\mathcal{F}_T^m\{\Delta\}^n.$$

The effect of $\{F_V\}^m$ is that of an additional forcing term containing the memory effect of the material and changes in temperature history stored in the thermal history variable m.

The Newmark β-γ method can now be employed to approximate the first and second order time derivatives in (2.8.1):

$$\frac{D^2\{\Delta\}^{n+1}}{Dt^2} = \frac{1}{\beta\Delta t^2}\left(\{\Delta\}^n - \{\Delta\}^{n-1}\right) - \frac{1}{\beta\Delta t}\frac{D\{\Delta\}^{n+1}}{Dt} - \left(\frac{1}{2\beta} - 1\right)\frac{D^2\{\Delta\}^{n-1}}{Dt^2}$$

$$\frac{D\{\Delta\}^{n+1}}{Dt} = \frac{D\{\Delta\}^n}{Dt} + \Delta t\left((1-\gamma)\frac{D^2\{\Delta\}^{n-1}}{Dt^2} + \gamma\frac{D^2\{\Delta\}^n}{Dt^2}\right).$$

For values $\alpha = 1/2$ and $\beta = 1/4$ this method is known to be unconditionally stable.

In the case of adiabatic process, $m \equiv 0$ and α, A are independent of T^n then the modified stiffness matrix for the pure visco-elastic problem has the form: $[\overline{K}] = (\Delta t)^{-\alpha}[G] + [K]$ and the additional visco-elastic load vector $\{F_V\}^n$ is given by:

$$\{F_V\}^n = A(\Delta t)^{-\alpha}[G]\left(\sum_{j=1}^{n} c_{j+1}(\alpha)\{\Delta\}^{n+1-j}\right), \tag{2.8.2}$$

the resulting discretized problem for the displacement $\{U\}^{n+1}$ without thermal effects is:

$$[M]\frac{D^2\{U\}^{n+1}}{Dt^2} + [\overline{K}]\{U\}^{n+1} = \{F\}^{n+1} - \{F_V\}^m, \tag{2.8.3}$$

where the thermo-elasticity coupling matrix $[C]$ is zero. Note that (2.8.3) is nothing but a modified linear elastic problem.

2.9 Numerical experiments

In this section several experiments in one and two dimensions are considered to test the thermo-visco-elastic model introduced in previous sections.

2.9.1 Free vibrations of a visco-elastic rod

Consider the problem of finding the vertical displacement $u(x)$ of a one dimensional visco-elastic vibrating rod clamped at the ends $u(0) = u(L) = 0$ and subjected to an initial sinusoidal prerturbation $u_0(x) = \sin(\pi x)$ at time $t = 0$ and then left free to its own vibration without any external force or traction imposed. The motion of the rod is governed by the equation (2.9.1) to be solved in space $0 \leq x \leq L$ and time $0 \leq t \leq t_f$:

$$\rho u_{tt} - \frac{\partial}{\partial x}\left(\frac{A}{\Gamma(1-\alpha)}\int_0^t (t-s)^{-\alpha} u_{xt}(s)\,\mathrm{d}s\right) = 0, \tag{2.9.1}$$

where ρ is the density of the rod and $A > 0$ and $0 \leq \alpha \leq 1$ are visco-elastic material parameters. Notice that for $\alpha = 0$ this problem reduces to the usual wave equation in one dimension for a linear elastic rod:

$$\rho u_{tt} - A u_{xx} = 0. \tag{2.9.2}$$

In the case $\alpha = 0$, the mechanical energy of the system is:

$$E(t) = \frac{1}{2}\int_0^L \left[\rho\left(\frac{\partial u}{\partial t}\right)^2 + A\left(\frac{\partial u}{\partial x}\right)^2\right]\,\mathrm{d}x. \tag{2.9.3}$$

A global property of the solution of this problem when $\alpha = 0$ is that $\dot{E}(t) = 0$, i.e. the mechanical energy is conserved. Every numerical method applied to solve the problem (2.9.1) must be able to represent this global property of the solution in the linear elastic limit $\alpha = 0$. Let $h = 1/25$ be the spatial mesh size, $N = 100$ the number of vertices of the mesh and $\{\Phi_a(x)\}_{a=1}^N$ a basis of linear triangular lagrangian shape functions then the global mass matrix $[M] \in \mathbb{R}^{N\times N}$ and stiffness matrix

$[K] \in \mathbb{R}^{N\times N}$ are explicitely given by the tridiagonal matrices:

$$[M] = \rho \begin{pmatrix} \frac{2h}{3} & \frac{h}{6} & \dots & 0 \\ \frac{h}{6} & \frac{2h}{3} & \dots & 0 \\ \vdots & \vdots & \ddots & \vdots \\ 0 & 0 & \dots & \frac{2h}{3} \end{pmatrix}, [K] = A \begin{pmatrix} \frac{2}{h} & -\frac{1}{h} & \dots & 0 \\ -\frac{1}{h} & \frac{2}{h} & \dots & 0 \\ \vdots & \vdots & \ddots & \vdots \\ 0 & 0 & \dots & \frac{2}{h} \end{pmatrix}, \tag{2.9.4}$$

leading to the differential system for the nodal displacement vector $\{U\} = (U_1, \dots, U_N)^T$:

$$[M]\frac{D^2\{U\}}{Dt^2} + [K]D^\alpha\{U\} = \{0\}. \tag{2.9.5}$$

In Figure 5 is shown the evolution in space and time of the numerical solution of the equation (2.9.1) for $\rho = A = 1$, $L = 5$, $t_f = 4$ and for two different values $\alpha = 0$ and $\alpha = 0.3$ using the Newmark method $\beta = 1/2$ $\gamma = 1/4$ and a time-step $\Delta t = 1/200$. Figure 4 shows the evolution over time of the solution $u(1/2, t)$. In the visco-elastic case $\alpha = 0.3$ the

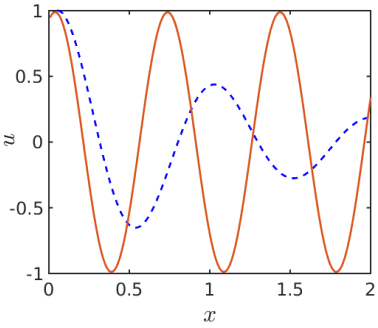

Figure 4: Temporal evolution of the vertical displacement in problem (2.9.1) $u(1/2, t)$ for $\alpha = 0$ (continuous line) and $\alpha = 0.3$ (dashed line).

Grünwald-Letnikov approximation of the fractional derivative $D^\alpha\{U\}$ is used, this leads to the formation of a pseudo-load vector $\{\overline{F}\}^n$ which represents the dislacement history up to the current time. This residual load vector has the effect of dissipating the mechanical energy of the system, according to the memeory effect of the material.

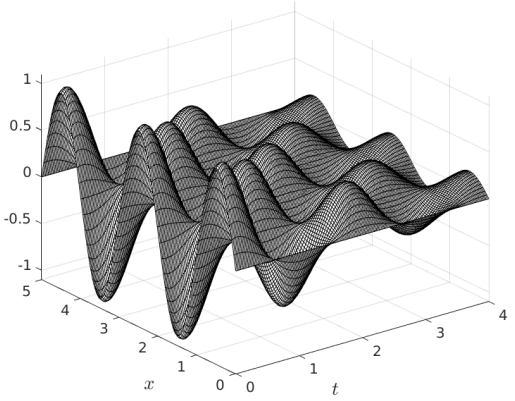

(a) Plot of $u(x,t)$ for $\alpha = 0.3$

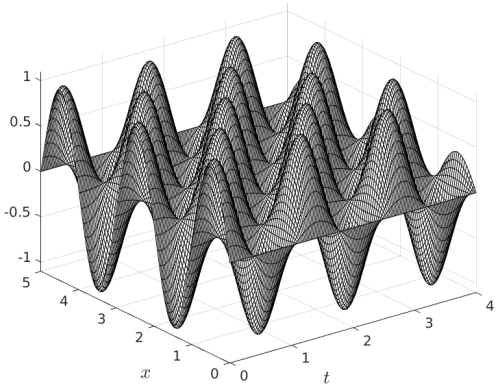

(b) Plot of $u(x,t)$ for $\alpha = 0$

Figure 5: Numerical solutions in space and time of the 1 dimensional visco-elastic wave equation (2.9.1) for different values of the fractional exponent α. For $\alpha = 0$ (linear elastic limit) the mechanical energy is conserved, while it is dissipated in the visco-elastic case $\alpha = 0.3$.

2.9.2 Dynamical response of a visco-elastic beam

Consider the dynamic response of a visco-elastic beam in a state of plane strain occupying a region $\Omega = [0, L] \times [0, H]$ in the undeformed configuration, clamped on later sides at $x = 0$ and $x = L$ and subjected to a traction vector $\bar{\mathbf{t}} = (0, -10)^T$ applied at the bottom side of the rectangle $\partial\Omega_B$. The problem in strong form can be written as: Find the displacement field $\mathbf{u} = (u_x, u_y)^T$ such that:

$$\begin{cases} \rho \dfrac{\partial^2 \mathbf{u}}{\partial t^2} - \operatorname{div}(\boldsymbol{\sigma}(\mathbf{u})) = \mathbf{0} & \text{in } \Omega \times [0, T] \\ \mathbf{u} = \mathbf{0} & \text{in } \Gamma_D \times (0, T] \\ \boldsymbol{\sigma}^T(\mathbf{u})\mathbf{n} = \bar{\mathbf{t}} & \text{in } \Gamma_N \times [0, T] \\ \mathbf{u}(0) = \mathbf{0},\ \dot{\mathbf{u}}(0) = \mathbf{0} & \text{in } \Omega \end{cases} \tag{2.9.6}$$

where $\mathbf{n}$ is the outward unit normal vector to $\partial\Omega$ and $\bar{\mathbf{t}}$ assigned surface traction. The stress $\boldsymbol{\sigma} = (\sigma_x, \sigma_y, \sigma_{xy})^T$ and strain $\boldsymbol{\varepsilon} = (\varepsilon_x, \varepsilon_y, \varepsilon_{xy})^T$ are related as:

$$\boldsymbol{\sigma}(\mathbf{u}) = A\mathbf{G}D^{\alpha}\boldsymbol{\varepsilon}(\mathbf{u}(t)) + K\mathbf{I}\boldsymbol{\varepsilon}(\mathbf{u}), \tag{2.9.7}$$

where matrices $\mathbf{G}$ and $\mathbf{I}$ are given by:

$$\mathbf{G} = \begin{pmatrix} \frac{4}{3} & -\frac{2}{3} & 0 \\ -\frac{2}{3} & \frac{4}{3} & 0 \\ 0 & 0 & 0 \end{pmatrix}, \quad \mathbf{I} = \begin{pmatrix} 1 & 1 & 0 \\ 1 & 1 & 0 \\ 0 & 0 & 0 \end{pmatrix}.$$

The material parameters for the simulations are $L = 10$, $H = 2$, $\rho = 10$, $K = 1000$, $A = 100$. The solution of this problem has been computed numerically for different values of $\alpha = \{0.1, 0.03, 0.05, 0.07\}$. The variational formulation of the problem, using the Grünewald-Letnikov approximation of the fractional derivative and a simple central difference scheme for the second order time derivative is as follows. Given $\boldsymbol{u}^{n-1}$

and $\boldsymbol{u}^n$, find $\boldsymbol{u}^{n+1}$ such that for all test function $\boldsymbol{v}$:

$$\int_\Omega \frac{\boldsymbol{u}^{n+1} - 2\boldsymbol{u}^n - \boldsymbol{u}^{n-1}}{\Delta t^2} \cdot \boldsymbol{v} + \int_\Omega \left((\Delta t)^{-\alpha} A\mathbf{G} + K\,\mathbf{I}\right) \boldsymbol{\varepsilon}(\boldsymbol{u}^{n+1}) : \boldsymbol{\varepsilon}(\boldsymbol{v}) =$$
$$\int_{\partial\Omega_B} \overline{\mathbf{t}} \cdot \boldsymbol{v} - (\Delta t)^{-\alpha} \int_\Omega A\mathbf{G} \left(\sum_{j=1}^{n} c_{j+1}(\alpha) \boldsymbol{\varepsilon}(\boldsymbol{u}^{n+1-j}) \right) : \boldsymbol{\varepsilon}(\boldsymbol{v}) \tag{2.9.8}$$

For a small time-step $\Delta t = 0.02$ the central difference scheme is stable. Snapshots of the displacement field are shown in Figure 6.

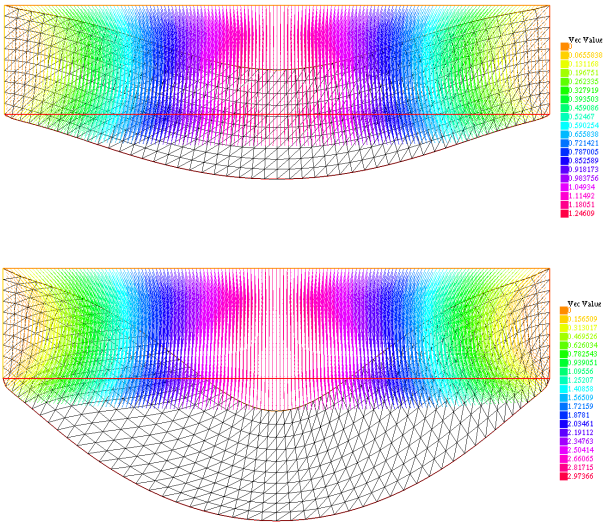

Figure 6: Displacement field $\boldsymbol{u} = (u_1, u_2)^T$ and deformed mesh at times $t = 1$ and $t = 2.5$.

In Figure 7 is reported the dynamical response of the vertical component u_y of the displacement field over time of the point $(L/2, H/2)$ in the undeformed configuration. As α increases, leaving the linear elastic limit $\alpha = 0$, the oscillations are damped and the relaxation is faster.

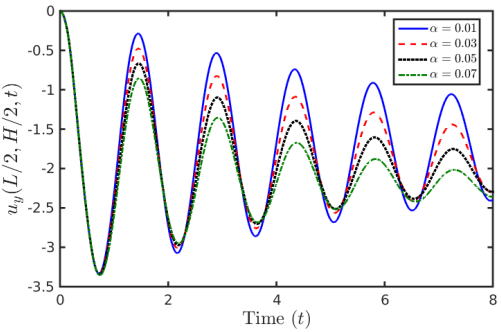

Figure 7: Plot over time of the dynamical reponse of the vertical displacement $u_y(L/2, H/2, t)$ for different values of $\alpha = \{0.01, 0.03, 0.05, 0.07\}$.

2.9.3 Creep and Creep-recovery test

One of the fundamental methods used to characterize the visco-elastic time-dependent behavior of a polymer is the creep test. In a creep test, a constant stress σ_0 is applied quasi-statically to a uniaxial tensile bar at zero time and held constant, as shown in Fig. 8.

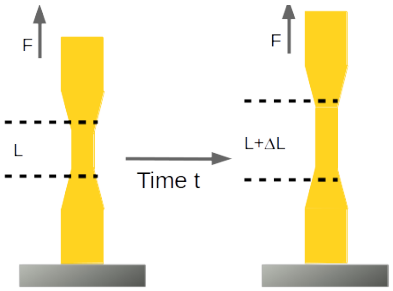

Figure 8: Schematic representation of a creep test.

The strain, under the constant load, increases with time up to a constant value ε_0. A specimen of size $H \times L$ is clamped on the bottom side and a traction $\mathbf{F} = (0, 160)^T$ is applied on the top of the beam setting $\sigma_0 = |\mathbf{F}|$. The inertia of the beam is neglected. Parametres for the simulation are $H = 0.02$, $L = 0.06$, $A = 10$, $K = 100$. Different values of

the fractional exponent are considered: $\alpha = \{0.01, 0.02, 0.03, 0.04\}$. Fig. 9(a) shows the strain response to a creep test. An equally important task of a constant stress test is to understand the resulting strain variation if the stress is removed. In this case the traction $\mathbf{F}$ is suddenly removed after a certain period. Results of the strain corresponding to the creep test recovey are shown in Fig. 9(b) for different values of the fractional exponent α.

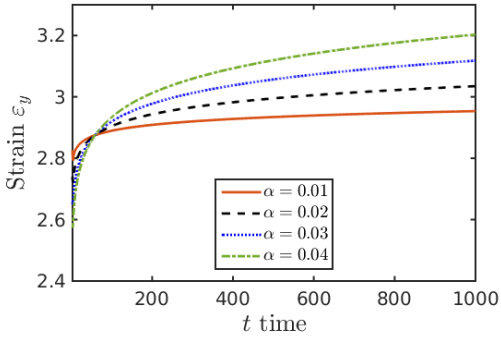

(a) Strain ε_y in a creep test.

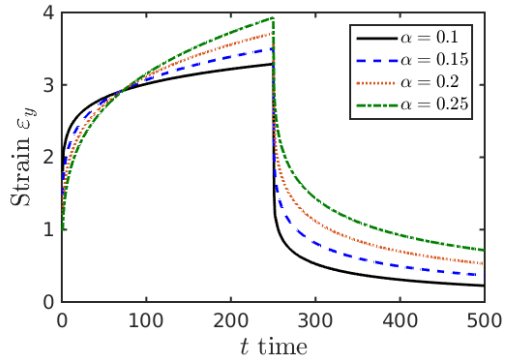

(b) Strain ε_y in a creep recovery test.

Figure 9: Numerical results of the creep and creep recovery test for different values of α.

2.9.4 Temperature behavior of the relaxation modulus

The variation of modulus with temperature can be determined from relaxation tests conducted at different constant temperatures. Material parameters for the numerical simulation at different temperatures $\alpha(T)$ and $A(T)$ are taken from (MP15) and are reported in Table 2:

Table 1: Material parameters for the rlaxation test

Temperature $T\ (^\circ C)$	$\alpha(T)$	$A(T)\ (s^\alpha)$
-35	0.226	814.7
-18	0.1015	52
0	0.05566	23
20	0.04227	11.04
40	0.07417	4.668
49	0.08634	4.116
60	0.06542	1.544

In the numerical experiment a specimen of lateral size $L = 0.02$m and vertical size $H = 0.06$m is subjected to a constant traction $\sigma_0 = 200$ N on the top size of the specimen. During the process the temperature is held constant. The Young modulus is:

$$E(t) = \sigma_0/\varepsilon_y(t). \tag{2.9.9}$$

Since this process is adiabatic we used the Grünwald-Letnikov approximation of the fractional derivative with constant coefficients α and A. Results of the relaxation curves obtained numerically are reported in Fig. 10 and are in good agreement with the experimental ones in 2 (a).

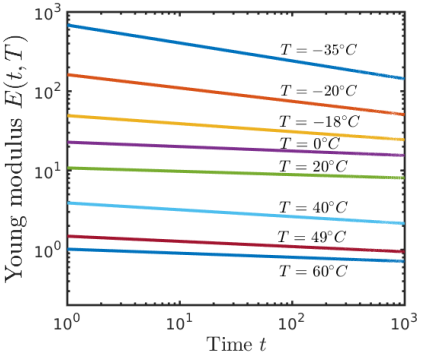

Figure 10: Numerical evaluation from relaxation tests of the relaxation behavior of the Young modulus at different temperatures T between $-35°C$ and $60°C$.

2.9.5 Coupled thermo-visco-elastic problem

As last example we consider a problem of coupled thermo-visco-elasticity. Let $[0,1] \times [0,1]$ be a square domain occupied in its undeformed configuration by a visco-elastic material in a state of plane strain. The displacement $\boldsymbol{u} = (u_x, u_y)^T$ is such that u_x is zero on the right hand side. Loading is provided by a transient thermal analysis in which the left side has a specified temperature $T_{left} = 1$ suddenly applied at time zero and held constant. The governing equations to be solved in $\Omega \times [0,T]$ is given by:

$$\begin{aligned} \rho c \, \frac{\partial T}{\partial t} + T_0 \beta \, \mathrm{div} \left(\frac{\partial \mathbf{u}}{\partial t} \right) &= k \Delta T \\ -\mathrm{div}(\boldsymbol{\sigma}(\mathbf{u}, T)) &= 0 \end{aligned} \tag{2.9.10}$$

where $\boldsymbol{\sigma}$ is the thermal stress:

$$\boldsymbol{\sigma}(\mathbf{u}, T) = \mathbf{G}\mathcal{D}(A^\tau, \alpha^\tau, \boldsymbol{\varepsilon}(\mathbf{u}))(t) + K\mathbf{I}\boldsymbol{\varepsilon}(\mathbf{u}) - \beta \mathbf{1}(T - T_0), \tag{2.9.11}$$

where $\mathcal{D}(A^\tau, \alpha^\tau, \boldsymbol{\varepsilon}(\mathbf{u}))(t)$ is the fractional-thermal derivative describing the relaxation behavior induced by heat conduction defined in (2.3.6), $\mathbf{1}$ is the vector $(1,1,0)^T$ and $\mathbf{G}$, $\mathbf{I}$ are matrices introduced in (2.9.2). Param-

eters used in the simulation are:

$$T_0 = 0.1, \beta = 0.25, k = 10, c = 1, \rho = 10, K = 300.$$

The material functions $A(T)$ and $\alpha(T)$ are fitted from (MP15) as:

$$A(T) = \begin{cases} 40.773 \exp(-0.056T), & \text{if } T \leq 49°C \\ 4.9444 \exp(-0.015T), & \text{if } T > 49°C \end{cases}$$
$$\alpha(T) = \begin{cases} 3 \times 10^{-9}T^4 - 7 \times 10^{-7}T^3 + 7 \times 10^{-5}T^2 \\ -0.0014 \times T + 0.0513, \quad \text{if } T \leq 49°C \\ -1 \times 10^{-7}T^3 + 4 \times 10^{-5}T^2 \\ -0.005 \times T + 0.2435, \quad \text{if } T > 49°C \end{cases} \tag{2.9.12}$$

and their plots are reported in Figure 11. The singularity at $T \approx 49°C$ shows that, crossing this value, the material exibits a phase transition. The parameter δ is chosen to be equal to 0.1 We consider a quasi-static

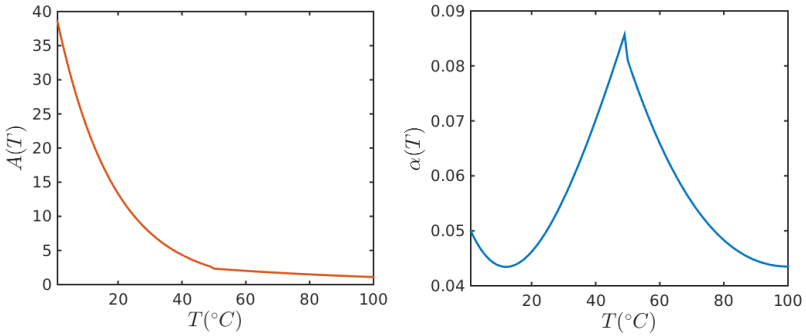

(a) Plot of $A(T)$. (b) Plot of $\alpha(T)$.

Figure 11: Material functions $A(T)$ and $\alpha(T)$ resulting from best fitting and used in the simulation.

case for the mechanical part and employ an Euler backward scheme for the thermal part in which $\Delta t = 0.005$. We can use a splitting technique to solve this problem dividing each temporal solution phase into a purely visco-elastic phase and into a thermal phase. (1) Given temperature T^n at time t^n, let $m_k \leq n$ be the current value of the thermal clock. The

visco-elastic problem consists in: Find the displacement $\boldsymbol{u}^{n+1}$, such that for all virtual displacement $\boldsymbol{v}$ is satisfied

$$\int_\Omega \left((\Delta t)^{-\alpha(T^{m_k})} A(T^{m_k})\mathbf{G} + K\,\mathbf{I}\right) \boldsymbol{\varepsilon}(\boldsymbol{u}^{n+1}) : \boldsymbol{\varepsilon}(\boldsymbol{v}) = \int_\Omega \beta T^n \,\mathrm{div}\,\boldsymbol{v} - (\Delta t)^{-\alpha} \int_\Omega A(T^{m_k})\mathbf{G} \left(\sum_{j=m_k}^{n} c_{n+2-j}(\alpha(T^{m_k}))\boldsymbol{\varepsilon}(\boldsymbol{u}^j) \right) : \boldsymbol{\varepsilon}(\boldsymbol{v}), \tag{2.9.13}$$

(2) Then, given $\boldsymbol{u}^{n+1}$ solution of the previous problem, we find temperature T^{n+1} such that for each test function δT solving the heat conduction equation:

$$\int_\Omega \rho c \frac{T^{n+1} - T^n}{\Delta t}\delta T + \int_\Omega k \nabla T^{n+1} \cdot \nabla \delta T + \int_\Omega \beta T_0 \,\mathrm{div}\left(\frac{\boldsymbol{u}^{n+1} - \boldsymbol{u}^n}{\Delta t}\right)\delta T = 0$$

In Figure 12 are shown the contour plots of temperature $T(x, y, t)$ and the horizontal component $\sigma_x(x, y, t)$ of the stress tensor for the initial and final time. The temperature is diffusing linearly propagating inside the region from the left lateral side of the square.

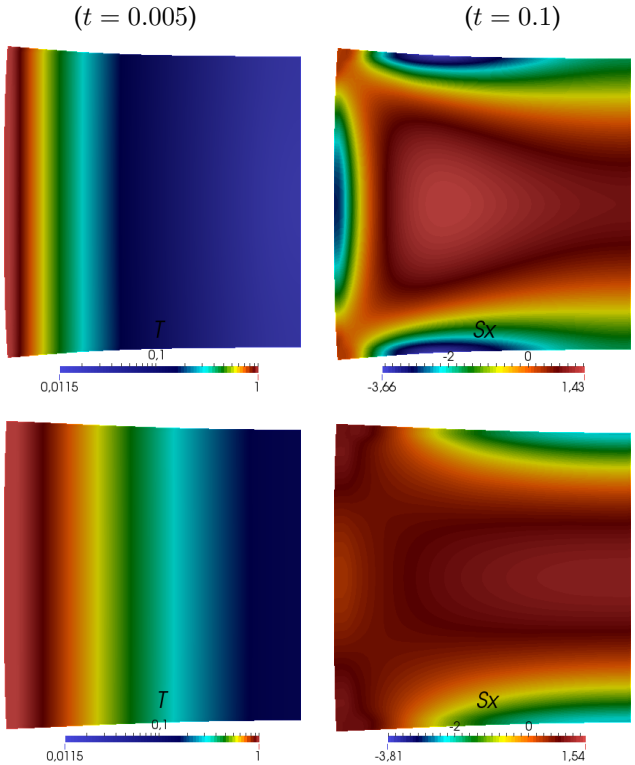

(c) $T(x, y)$ (d) $\sigma_x(x, y)$

Figure 12: Contour plots of the temperature and the horizontal component σ_x of the displacement at initial time $t = 0.005$ and final time $t = 0.1$.

Chapter 3

Thermo-diffusive problems in photovoltaics

Typical photovoltaic (PV) modules are laminates made of a thick glass superstrate, an encapsulating polymer (usually ethylene vinyl acetate, EVA), a layer of interconnected Silicon solar cells separated by few centimeters of EVA in their plane, another layer of EVA, and finally a polymeric protective backsheet (see Fig.13). EVA provides protection of cells and interconnections but it is permeable to moisture, which diffuses from the backsheet and percolates along the surface of the solar cells. Moisture induces chemical oxidation of the grid line deposited on the surface of the solar cells, separating it from Silicon giving rise to electrically inactive areas and power-loss. This phenomenon has been reported in damp heat tests in (MVI12) prescribed by the international qualification standards (61215), where PV modules were exposed to a very aggressive environment at constant $85°$C temperature and 85% of air humidity. For these reasons, an accurate modelling of the EVA is crucial to determine the lifetime of a PV module, moisture diffusion, chemical reactions induced by moisture, as well as its reduction of cohesive energy promoting delamination of the layers. The EVA polymer displays a strong thermo-visco-elastic constitutive response, as experimentally reported in (UE11; MP11), with a variation of the elastic modulus of up to three or-

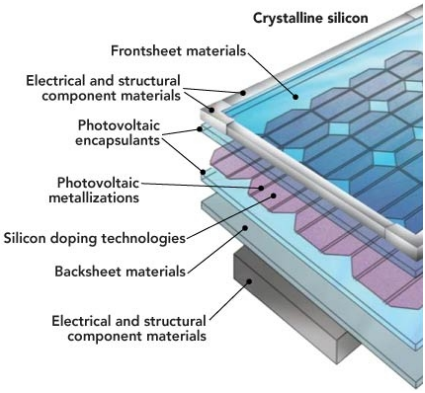

Figure 13: Sketch of a PV module.

ders of magnitude depending on temperature. Generalized Maxwell rheological models used so far generally provide exponential type relations for the relaxation modulus and, in order to approximate the experimentally observed power-law trend, a huge number of elements (and thus of model parameters) has be taken into account. To significantly simplify the task of parameters identification, modelling the visco-elastic behaviour via fractional derivatives has been proved to be very effective (Mai10; MDP13; MDP11). For rheologically complex polymers as EVA, whose microstructure changes with temperature, the fractional calculus formulation in (MP15) allows the use of only two temperature dependent parameters for its complete description.

A proper modelling of these coupled nonlinear phenomena, requires a comprehensive computational framework where coupled thermoelastic and heat conduction problems are accurately solved at the module level in the three-dimensional space. Then, moisture diffusion inside the EVA layers has to be simulated by considering the dependency on the temperature and the thermo-elastic fields via the diffusive constitutive equations. So far, the state-of-the-art simulations on moisture diffusion in (Kem14) consider the EVA layer only and treat diffusion as a one dimensional problem without updating the diffusivity of the material

based on the actual temperature of the system.

To shed light into the above issues, and provide a comprehensive physical modelling and computational framework for the study of these phenomena, a geometrical multiscale approach is pursued by following the seminal work in (AQ03) for biophysical systems. Starting from the evidence that moisture diffusion takes place in a physical domain with a lower dimension with respect to that of the thermo-mechanical and heat conduction problems, two different finite element models are used in parallel. The coupled thermo-mechanical and heat conduction problems are solved in the three-dimensional setting (or in the two-dimensional one in the case of a cross-section of the PV module). As a further simplification, the EVA encapsulant layers are modelled as zero-thickness interfaces, whose thermo-visco-elastic constitutive response is taken into account by a novel thermo-viscoelastic cohesive zone model. As compared to other cohesive zone model formulations available in the literature (RB13; GA15), the present model is based on a fractional calculus formulation able to simulate rheologically complex materials.

The thermo-elastic problem, which is much faster than moisture diffusion, is solved first via a fully implicit solution scheme in space and time. Temperature and relative displacements computed in the Gauss points along the encapsulant interfaces are then projected to the nodes of another finite element model specific for the solution of moisture diffusion. This second model is used to discretize the domain where moisture diffusion takes place. In particular, it is represented by the mid-surfaces of the encapsulant layers and of the channel cracks through Silicon, see Fig.14.

3.1 Variational framework

In this section is presented the variational framework describing moisture diffusion and the thermo-visco-elastic response of a laminate made of linear elastic homogeneous and isotropic layers separated by polymeric thermo-visco-elastic laminae. In these laminates, moisture diffusion takes place in the polymeric layers, which progressively percolates

from the free edges and from the backsheet towards the centre of the solar cells. EVA layers used to protect Silicon solar cells are permeable to moisture, which is one of the major concerns for the degradation of the electrical output of the PV module over time. Due to moisture diffusion, the adhesive properties of EVA progressively degrade and the corresponding layers may experience a lack of cohesion leading to separation of the backsheet from the Silicon cells, or between the Silicon cells from the glass superstrate. In order to efficiently simulate cohesive degradation of EVA and delamination, we propose to treat the polymeric layers as zero-thickness internal interfaces with suitable traction-separation relations accounting for the thermo-visco-elastic properties of EVA.

Let assume that the laminate occupies a volume $\Omega = \cup_{m=1}^{n} R(m) \subset \mathbb{R}^3$ in the reference undeformed configuration, where each layer is geometrically identified by $R(m) = [0, a] \times [0, b] \times [z_{m-1}, z_m]$, with $z_0 = 0$, $z_m = z_{m-1} + h_m$, being $a, b >> h_m$ for $m = 1, \ldots, n$. Moreover, let model a generic polymeric layer of thickness h between laminae $R(p) = R_-$ and $R(p+1) = R_+$ $(1 \leq p \leq n)$ as a plane surface $S(p) = \{(x_1, x_2, z_p) \ : 0 \leq x_1 \leq a, 0 \leq x_2 \leq b\}$, see Fig.14.

The position of each material point inside Ω is identified by the coordinate vector $\mathbf{x} = (x_1, x_2, x_3)$ in a three-dimensional cartesian orthonormal frame $\{\mathbf{e}_1, \mathbf{e}_2, \mathbf{e}_3\}$. Let $u_I(x_1, x_2, x_3, t)$ $(I = 1, 2, 3)$ and $\theta(x_1, x_2, x_3, t)$ $= T(x_1, x_2, x_3, t) - T_0$ be the displacement field and temperature variation from a reference one, T_0, inside the material during the time interval $0 \leq t \leq t_f$. The index I is denoting the component of the displacement field along the corresponding coordinate.

3.1.1 Thermo-mechanical formulation of the layers

The global dynamics of each material layer $R(m)$ obeys the equations of coupled linear isotropic thermo-elasticity (see e.g. (Now86)). The Cauchy thermal stress tensor is defined for each layer m as:

$$\sigma_{IJ} = C^m_{IJKL}\varepsilon_{KL} - \beta^m \theta \delta_{IJ}, \ 1 \leq I, J, K, L \leq 3 \tag{3.1.1}$$

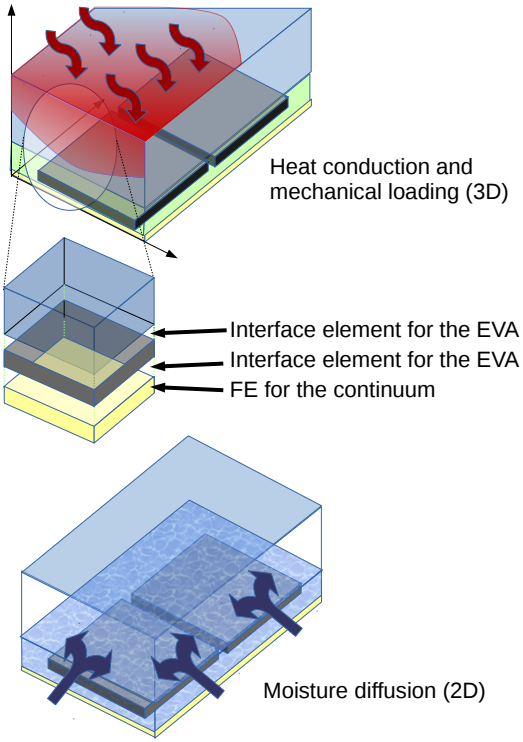

(a) 3D laminate models

Figure 14: Proposed finite element model.

where the Einstein summation notation has been adopted. Here, C^m_{IJKL} is the fourth order elastic constitutive tensor, and β^m is the coupling thermal factor related to the thermal expansion coefficient α^m. The infinitesimal strain tensor is:

$$\varepsilon_{IJ} = \frac{1}{2}\left(\frac{\partial u_I}{\partial x_J} + \frac{\partial u_J}{\partial x_I}\right), \; 1 \leq I, J \leq 3 \tag{3.1.2}$$

The balance of linear momentum in each layer $R(m) \times [0, t_f]$ is given

by:

$$\rho^m \frac{\partial^2 u_I}{\partial t^2} - \frac{\partial}{\partial x_J}\left(C^m_{IJKL}\varepsilon_{KL} - \beta^m \theta \delta_{IJ}\right) = 0\ ,\ I = 1,2,3 \tag{3.1.3}$$

where ρ^m is the density of the m-th material.

Let be q_I the heat flux inside each layer $R(m)$, and assume that it is related to the temperature variation θ by the Fourier law:

$$q_I = -k^m \frac{\partial \theta}{\partial x_I},\ 1 \leq I \leq 3 \tag{3.1.4}$$

where $k^m > 0$ is the thermal conductivity of the m-th material. Hence, the heat transfer partial differential equation is given by:

$$k^m \nabla^2 \theta = \rho^m c^m \frac{\partial \theta}{\partial t} + T_0 \beta^m \frac{\partial \varepsilon_{KK}}{\partial t} \quad \text{in } R(m) \times [0, t_f] \tag{3.1.5}$$

where c^m is the heat capacity of the m-th material.

3.1.2 Thermo-visco-elastic polymeric interfaces

Under the assumption of replacing each polymeric layer by a zero-thickness imperfect interface, we allow u_I and the temperature θ to be discontinuous across the interface separating R_- from R_+. We therefore define the jumps on $S(p)$ as:

$$[[u_I]](x_1, x_2) = u_I^+(x_1, x_2) - u_I^-(x_1, x_2), \quad 1 \leq I \leq 3, \tag{3.1.6a}$$

$$[[\theta]](x_1, x_2) = \theta^+(x_1, x_2) - \theta^-(x_1, x_2) \tag{3.1.6b}$$

where $u_I^{\pm}(x_1, x_2) = u_I^{\pm}(x_1, x_2, z_p^{\pm})$ and $\theta_I^{\pm}(x_1, x_2) = \theta_I^{\pm}(x_1, x_2, z_p^{\pm})$. The average temperature across the interface is given by:

$$\langle \theta \rangle (x_1, x_2) = \frac{1}{2}\left[\theta^+(x_1, x_2) + \theta^-(x_1, x_2)\right] \tag{3.1.7}$$

Quantities $[[u_I]]$ and $[[\theta]]$ play the role of internal variables describing the debonding process along the interface containing $S(p)$ during time $[0, t_f]$.

Hence, the coupled thermo-elastic model given in the previous section for the continuum layers is enriched by adding the presence of a

cohesive traction field and a heat flux normal to $S(p)$. The relations between those fields and $[[u_I]]$, $[[\theta]]$ are provided by the constitutive relations for the interface. By assuming the continuity of the traction vector t_I $(1 \leq I \leq 3)$, we set:

$$t_I = \begin{cases} K_I\left(t, \langle\theta\rangle\right)[[u_I]], & \text{if } [[u_I]] \in J_I \\ 0, & \text{if } [[u_I]] \notin J_I \end{cases} \tag{3.1.8}$$

where $J_I = (-\delta_I^c, +\delta_I^c)$ for $I = 1, 2$ and $J_3 = (0, \delta_3^c)$. The components t_1 and t_2 represent Mode II and Mode III cohesive tractions, i.e., contained in the plane surface $S(p)$, whereas t_3 corresponds to the Mode I cohesive traction, i.e. associated to the unit vector $\mathbf{n} = \mathbf{e}_3$.

Equation (3.1.8) for $I = 3$ corresponds to a tension cut-off traction-separation curve, suggesting that the interface is not able to transfer tractions when the critical opening displacement δ_3^c is achieved. A similar brittle behavior is assumed for Mode II and Mode III (see Fig.15).

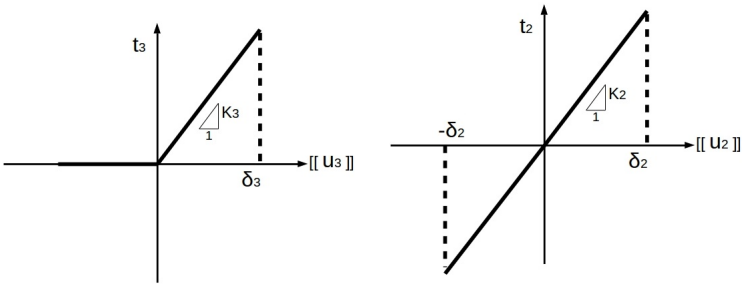

(a) Mode I (b) Mode II

Figure 15: Cohesive traction-separation relations.

In order to obtain a structural response of the interface equivalent to that of the real EVA layers, the modulus K_3 of the zero-thickness interface is related to the stiffness of the layer in the direction $\mathbf{n}$, i.e., it can be evaluated as the ratio between the EVA Young's modulus, E_{EVA}, and the EVA thickness, h_{EVA}. Similarly, the shear response is matched by selecting $K_1 = K_2 = E_{\text{EVA}}/\left[2(1 + \nu_{\text{EVA}})\right]$.

Since polymers have a thermo-visco-elastic constitutive behavior, the stiffnesses K_I has to depend upon the average temperature $\langle\theta\rangle$ and time t. Instead of using a Prony series representation, a fractional calculus approach (Mai10; MDP13), is herein adopted to synthetically characterize those dependencies, which has been proved in (MP15) to be more effective for parameters identification. Accordingly, we define K_3 as follows:

$$K_3(t,T) = \frac{a(T)\, f(t,T)^{-\alpha(T)}}{h\Gamma(1-\alpha(T))} \tag{3.1.9}$$

for functions $0 < a, \alpha < 1$ and $\Gamma(t)$ is the Euler gamma function defined as:

$$\Gamma(t) = \int_0^\infty e^{-x} x^{t-1} \mathrm{d}x \tag{3.1.10}$$

Function $f(t,T)$ is a history dependent function of time and temperature used to model thermo-rheologically complex materials where the principle of time-temperature superposition does not apply. This is due to a modification of the internal microstructure of the polymer driven by a temperature change above a threshold. Hence, $f(t,T)$ is equal to the current time t minus the time t_0 corresponding to such a microstructure modification.

At the interface, we remark that cohesive tractions are continuous and opposing to each other, viz.:

$$\begin{aligned} t_I = t_I^+ &= C^{(+)}_{IJKL}\varepsilon^+_{KL}|_{x_3=z_p^+} n_J = -C^{(-)}_{IJKL}\varepsilon^-_{KL}|_{x_3=z_p^-} n_J \\ &= -t_I^- \end{aligned} \tag{3.1.11}$$

As far as heat conduction is concerned, we assume that the heat flux across the interfaces is oriented along the direction orthogonal to the surface $S(p)$, which is a reasonable approximation for thin polymeric layers. Hence, $q_1 = q_2 = 0$ and $q = q_3$ is given by:

$$q = \begin{cases} -\kappa_0 \left(1 - \dfrac{[[u_3]]}{\delta_3^c}\right) \langle\theta\rangle & \text{if } [[u_3]] \in J_3 \\ 0 & \text{if } [[u_3]] \notin J_3 \end{cases} \tag{3.1.12}$$

where κ_0 is the thermal conductivity of the interface without decohesion, i.e., for $[[u_3]] = 0$. Note that the heat flux is assumed to be a decreasing function of the normal gap.

Also in this case, continuity of heat flux at the interface is preserved, viz.:

$$\begin{aligned} q = q_3^+(x_1, x_2) &= -k^{(+)} \frac{\partial \theta^+}{\partial x_3}|_{x_3=z_p^+} = k^{(-)} \frac{\partial \theta^-}{\partial x_3}|_{x_3=z_p^-} \\ &= -q_3^-(x_1, x_2) \end{aligned} \tag{3.1.13}$$

3.1.3 Moisture diffusion along polymeric interfaces

Durability tests of PV modules inside a climate chamber are characterized by temperature and moisture dependent on time and according to specified ramps. In these composites, moisture diffusion takes place along the layers of the polymeric encapsulant, or along channel cracks in Silicon. Since their thickness is very small, it is also possible to neglect the moisture flux in the direction orthogonal to the EVA layers. Under these assumptions, moisture diffusion can be modelled as a diffusion process taking place over the mid-surface of a generic encapsulant layer, which corresponds to $S(p)$.

Hence, the aim of the numerical method reduces to simulate and predict diffusion of water content $c(x_1, x_2, t)$ along the encapsulant mid-surface $S(p)$ for each point and time.

The following initial and boundary value problem can be considered, where an imposed water content c^* is imposed on the boundary:

$$\begin{cases} \dfrac{\partial c}{\partial t}(x_1, x_2, t) - D\nabla^2 c(x_1, x_2, t) = 0 & \text{in } S(p) \times [0, t_f] \\ c(x_1, x_2, 0) = 0 & \text{in } S(p) \\ c(x_1, x_2, t) = c^* & \text{in } \partial S(p) \times [0, t_f] \end{cases} \tag{3.1.14}$$

where D is the encapsulant diffusivity.

It is worth noting that the diffusion problem takes place in dimension 2, while the thermo-mechanical problem is three-dimensional. it is also remarkable to notice that these physical problems are characterized by very different time scales. The characteristic velocity of thermal diffusion is in fact ruled by the ratio $k^m/(\rho^m c^m)$, while that of moisture diffusion is given by the diffusivity D. Considering characteristic values for EVA,

the ratio between the velocities of the two phenomena is:

$$\left(k^m/(\rho^m c^m)\right)/D \approx 10^6, \qquad \forall m = 1, \ldots, n$$

so that heat transfer is about six order of magnitude faster than moisture diffusion. From this observation, we can state that moisture diffusion is dependent on heat transfer and not viceversa. Hence, the diffusivity of the encapsulant has to be considered as temperature dependent and, based on the experimental evidence, of Arrhenyus type can be used to model it (Kem14):

$$D = \begin{cases} A \exp\left(-E_a/(\langle\theta\rangle\, R)\right), & \text{if } [[u_3]] \leq \delta_3^c \\ A \exp\left(-E_a/(\langle\theta\rangle\, R)\right) \dfrac{[[u_3]]}{\delta_3^c}, & \text{if } [[u_3]] > \delta_3^c \end{cases} \tag{3.1.15}$$

In order to take into account the effect of a possible debonding of the encapsulant, which would enhance moisture diffusion, D is assumed to be a linear increasing function of the normal gap $[[u_3]]$, for $[[u_3]]$ larger than δ_3^c.

Due to the very different time scales of the diffusion processes, a staggered solution scheme is proposed, where the average temperature and the crack opening computed from the solution of the coupled thermo-mechanical problem are passed as input to the diffusion process by a suitable update of the value of D.

3.2 Weak forms

The partial differential equations governing the dynamic equilibrium of the body, Eq. (3.1.3), and heat conduction, Eq. (3.1.5), for each layer $R(m)$ $(m = 1, \ldots, n)$ and the constitutive relations for the interfaces, Eqs. (3.1.8) and (3.1.12) for each $S(p)$, define an initial boundary value problem describing the debonding of a thermo-mechanical layered PV panel with thermo-visco-elastic polymeric interfaces.

Let be t_I^* and u_I^* the surface traction and the prescribed boundary

displacement such that:

$$C_{IJKL}\varepsilon_{KL}(u_M)n_J = t_I^* \quad \text{in } \partial_N R^u \times [0, t_f],$$
$$u_I = u_I^* \quad \text{in } \partial_D R^u \times [0, t_f]$$

and $q^* = q_I^* n_I$, and θ^* the imposed normal heat flux and the imposed temperature at the boundaries such that:

$$\frac{\partial \theta}{\partial n} = q^* \quad \text{in } \partial_N R^\theta \times [0, t_f],$$
$$\theta = \theta^* \quad \text{in } \partial_D R^\theta \times [0, t_f]$$

where the indices ∂_D and ∂_N denote the Dirichlet and the Neumann portions of the boundary ∂R.

The weak form corresponding to Eq.(3.1.3) is obtained by multiplying it for a virtual displacement δv_I having a virtual gap $[[\delta v_I]]$ along $S(p)$ and by integrating the result on each domain $R(m)$. After applying the divergence theorem as customary and by dropping the index m to simplify notation, we obtain:

$$\begin{aligned} &\int_R \rho \frac{\partial^2 u_I}{\partial t^2} \delta v_I \mathrm{d}V + \int_R C_{IJKL}\varepsilon_{KL}\delta\varepsilon_{IJ}\mathrm{d}V - \\ &\int_R \beta \delta\varepsilon_{IJ}\delta_{IJ}\theta \mathrm{d}V = \int_{\partial_N R^u} t_I^* \delta v_I \mathrm{d}A + \int_{S(p)} t_I [[\delta v_I]] \mathrm{d}A \end{aligned} \tag{3.2.1}$$

Analogously, the weak form corresponding to Eq.(3.1.5) is obtained by multiplying it for a test function $\delta\theta$ having a gap $[[\delta\theta]]$ on $S(p)$ and by integrating the result on each domain $R(m)$. After some calculation and dropping the index m to simplify notation, we get:

$$\begin{aligned} &\int_R k \frac{\partial \theta}{\partial x_I}\frac{\partial \theta}{\partial x_I}\mathrm{d}V + \int_R \rho c \frac{\partial \theta}{\partial t}\delta\theta \mathrm{d}V + \\ &\int_R \beta \frac{\partial \varepsilon_{IJ}}{\partial t}\delta_{IJ}\delta\theta \mathrm{d}V + \int_{\partial_N R^\theta} q^* \delta\theta \mathrm{d}A + \int_{S(p)} q[[\delta\theta]] = 0 \end{aligned} \tag{3.2.2}$$

As far as moisture diffusion is concerned, the corresponding weak form is constructed by multiplying Eq.(3.1.14) by a test function δc. After

integration by parts we have that the concentration $c(x_1, x_2, t)$ solves the following equation for all the admissible δc and $\forall t \in [0, t_f]$:

$$\int_{S(p)} D \frac{\partial c}{\partial x_I} \frac{\partial \delta c}{\partial x_I} \mathrm{d}A + \int_{S(p)} \delta c \frac{\partial c}{\partial t} \mathrm{d}A = 0 \tag{3.2.3}$$

3.3 Finite element discretization

3.3.1 Discretized weak forms for the thermo-elastic and heat conduction problems

According to the finite element method, the domain R is discretized into a finite number of bulk R_e and interface $\tilde{S}_e$ elements so that:

$$R \approx \bigcup_e R_e \cup \bigcup_e \tilde{S}_e \tag{3.3.1}$$

We also introduce for the purpose of numerical integration the mid-plane surface $S(p) \approx \cup_e S_e$, where S_e is the middle surface of each interface element $\tilde{S}_e$.

The class of interface elements considered here consists of two surface elements coincident with the facets of the bulk elements used to discretize the continuum that are bricks or tetrahedra. For consistency between interfaces and bulk, the same order of interpolation is used.

In the case of 2D simulations on cross-sections of a laminate, the present formulation still holds, provided that bulk elements are represented by quadrilateral or triangular plain strain finite elements and interface elements are given by two opposing lines. Again, the same interpolation order has to be used.

By introducing the shape functions, the finite element approximation for the bulk reads:

$$U_K(x_1, x_2, x_3, t) = \sum_{a=1}^{N(e)} \Phi_a(\xi_1, \xi_2, \xi_3) U_{aK}(t), \quad 1 \leq K \leq 3$$

$$\Theta(x_1, x_2, x_3, t) = \sum_{a=1}^{N(e)} \Phi_a(\xi_1, \xi_2, \xi_3) \Theta_a(t)$$

being $\{\Phi_a(\xi_1,\xi_2,\xi_3)\}_{a=1}^{N(e)}$ defined in the natural reference system $-1 \leq \xi_1,\xi_2,\xi_3 \leq +1$, where $N(e)$ is the number of element nodes, which is equal to 8 for a $3D$ linear brick element, or 4 for a $2D$ linear 4-node plane strain element.

Similarly, for the interface elements, the gaps are approximated as:

$$[[U_J]](x_1,x_2,t) = \sum_{a=1}^{S(e)} \sum_{b=1}^{2S(e)} \Psi_a(\xi_1,\xi_2)\Delta_{aJbK}U_{bK}(t), \quad 1 \leq J \leq 3$$

$$[[\Theta]](x_1,x_2,t) = \sum_{a=1}^{S(e)} \sum_{b=1}^{2S(e)} \Psi_a(\xi_1,\xi_2)\Delta_{ab}\Theta_b(t)$$

where the shape functions $\{\Psi_1(\xi_1,\xi_2)\}_{a=1}^{S(e)}$ are defined along the mid-surface plane in the natural reference system $-1 \leq \xi_1,\xi_2 \leq +1$ and $2S(e)$ is the number of nodes of the interface element which is equal to 8 for a $3D$ interface element compatible with bricks, or 4 for a $2D$ interface element compatible with plane strain elements. The nodal displacement vector is:

$$(U_{11},U_{12},U_{13},\ldots,U_{2S(e)1},U_{2S(e)2},U_{2S(e)3})^{\mathrm{T}} = (U^+_{11},U^+_{12},U^+_{13},\ldots,$$
$$U^+_{S(e)1},U^+_{S(e)2},U^+_{S(e)3},U^-_{11},U^-_{12},U^-_{13},\ldots,U^-_{S(e)1},U^-_{S(e)2},U^-_{S(e)3})^{\mathrm{T}}$$

and the temperature vector is:

$$(\Theta_1,\ldots,\Theta_{2S(e)})^{\mathrm{T}} = (\Theta^+_1,\ldots,\Theta^+_{S(e)},\ldots,\Theta^-_1,\ldots,\Theta^-_{S(e)})^{\mathrm{T}}.$$

The operator $[\Delta_e]_{aIbJ}$ applied to the nodal displacements of the interface element leads to the relative opening displacement between the $(+)$ and the $(-)$ interface flanks, i.e., $[\Delta_e]_{aIbJ}U_{bJ} = [[U_{aI}]]$ $(1 \leq a \leq S_e,\ 1 \leq b \leq 2S_e,\ 1 \leq I,J \leq 3)$.

Similarly, the operator $[\Delta_e]_{ab}$ applied to the nodal temperatures of the interface element leads to the temperature jumps between the $(+)$ and the $(-)$ interface flanks, i.e., $[\Delta_e]_{ab}\Theta_a = [[\Theta_a]]$ $(1 \leq a \leq S_e,\ 1 \leq b \leq 2S_e)$. Analogous expressions hold for the test functions δU_K, $[[\delta U_K]]$, $\delta\Theta$, and $[[\delta\Theta]]$.

After introducing these expressions in the weak form (3.2.1), its discretized version is obtained:

$$\sum_e \int_{R_e} \rho \Phi_b \Phi_a \frac{\partial^2 U_{bI}}{\partial t^2} \delta U_{aI} \mathrm{d}V + \sum_e \int_{R_e} C_{IJKL} \frac{\partial \Phi_b}{\partial x_L} \frac{\partial \Phi_a}{\partial x_J} U_{bK} \delta U_{aI} \mathrm{d}V -$$
$$\sum_e \int_{R_e} \Phi_a \beta \delta_{KL} \frac{\partial \Phi_b}{\partial x_L} \Theta_a \delta U_{bK} \mathrm{d}V = \sum_e \int_{S_e} t_J \Psi_a \Delta_{aJbK} \delta U_{bK} \mathrm{d}A +$$
$$\sum_e \int_{\partial R_e} t_I^* \Phi_a \delta U_{aI} \mathrm{d}A \tag{3.3.2}$$

Similarly, the discretized weak form (3.2.2) is:

$$\sum_e \int_{R_e} \rho c \Phi_a \Phi_b \frac{\partial \Theta_a}{\partial t} \delta \Theta_b \mathrm{d}V + \sum_e \int_{R_e} k \frac{\partial \Phi_a}{\partial x_L} \frac{\partial \Phi_b}{\partial x_L} \Theta_a \delta \Theta_b \mathrm{d}V +$$
$$\sum_e \int_{\partial R_e} q^* \Phi_a \delta \Theta_a \mathrm{d}A + \sum_e \int_{R_e} T_0 \beta \delta_{KL} \frac{\partial \Phi_b}{\partial x_L} \frac{\partial U_{bK}}{\partial t} \Phi_a \delta \Theta_a \mathrm{d}V + \tag{3.3.3}$$
$$\sum_e \int_{S_e} q \Psi_a \Delta_{ac} \delta \Theta_c \mathrm{d}A = 0$$

In matrix form, the previous discretized weak forms become:

$$\sum_e \{\delta U_e\}^T [M_e^{uu}] \frac{D^2\{U_e\}}{Dt^2} + \sum_e \{\delta U_e\}^T [K_e^{u\theta}] \{U_e\} +$$
$$\sum_e \{\delta U_e\}^T [C_e^{u\theta}] \{\Theta_e\} = \sum_e \{\delta U_e\}^T \{F_e^u\} + \sum_e \{\delta U_e\}^T \{f_e^u\} \tag{3.3.4}$$

$$\sum_e \{\delta \Theta_e\}^T [K_e^{\theta\theta}] \{\Theta_e\} + \sum_e \{\delta \Theta_e\}^T [C_e^{u\theta}] \frac{D\{\Theta_e\}}{Dt} +$$
$$\sum_e \{\delta \Theta_e\}^T [C_e^{u\theta}] \frac{D\{U_e\}}{Dt} + \sum_e \{\delta \Theta_e\}^T \{F_e^\theta\} + \sum_e \{\delta \Theta_e\}^T \{f_e^\theta\} = 0 \tag{3.3.5}$$

where $\{U_e\} = (U_{11}, U_{12}, U_{13}, \ldots, U_{1N}, U_{1N}, U_{1N})^{\mathrm{T}}$ is the nodal displacement vector and $\{\Theta_e\} = (\Theta_1, \ldots, \Theta_N)^{\mathrm{T}}$ is the nodal temperature vector, and N stands either for $N(e)$ for a bulk element, or for $2S(e)$ for an interface element. Expressions for the matrices are detailed in Appendix.

By introducing $\{\Delta_e\} = (U_{11}, U_{12}, U_{13}, \Theta_1, \ldots, U_{N1}, U_{N2}, U_{N3}, \Theta_N)^{\mathrm{T}} = [P]^{\mathrm{T}}(\{U_e\}, \{\Theta_e\})^{\mathrm{T}}$, the generalized displacement vector at the element

level with the following ordering, where N stands for either $N(e)$ for the bulk elements, or $2S(e)$ for the interface elements, is:

$$\begin{aligned}&\sum_e \{\delta\Delta_e\}^T [M_e] \frac{D^2\{\Delta_e\}}{Dt^2} + \sum_e \{\delta\Delta_e\}^T [C_e] \frac{D\{\Delta_e\}}{Dt} + \\ &\sum_e \{\delta\Delta_e\}^T [K_e]\{\Delta_e\} = \sum_e \{\delta\Delta_e\}^T \{F_e\} + \sum_e \{\delta\Delta_e\}^T \{f_e\}\end{aligned} \tag{3.3.6}$$

where the expressions for the mass, $[M_e]$, the damping, $[C_e]$, and the stiffness matrix, $[K_e]$, as well as for the load vector, $\{F_e\}$, and the interface load vector, $\{f_e\}$, are collected in the Appendix. Note that to pass from Eqs.(3.3.4) and (3.3.5) to Eq.(3.3.6), a permutation matrix $[P]$ has been used, see again Appendix for more details.

Let be $\{\Delta\}$ the global displacement vector and $[L_e]$ the localization matrix that selects the element nodal values, viz.:

$$\{\Delta_e\} = [L_e]\{\Delta\} \tag{3.3.7}$$

hence, we can recast Eq. (3.3.6):

$$\begin{aligned}&\{\delta\Delta\}^T [M] \frac{D^2\{\Delta\}}{Dt^2} + \{\delta\Delta\}^T [C] \frac{D\{\Delta\}}{Dt} + \\ &\{\delta\Delta\}^T [K]\{\Delta\} = \{\delta\Delta\}^T \{F\} + \{\delta\Delta\}^T \{f\}\end{aligned} \tag{3.3.8}$$

where the global mass, dumping and stiffness matrices and the load vector are assembled as follows:

$$\begin{aligned}&[M] = \sum_e [L_e]^T [M_e][L_e] \,, \{F\} = \sum_e [L_e]^T \{F_e\}, \\ &[K] = \sum_e [L_e]^T [K_e][L_e] \,, [C] = \sum_e [L_e]^T [C_e][L_e], \\ &\{f\} = \sum_e [L_e]^T \{f_e\}\end{aligned}$$

By simplifying the virtual variation of the test function $\{\delta\Delta\}$ and neglecting the inertial term, the thermo-mechanical problem requires the solution of the following nonlinear set of equations:

$$[C] \frac{D}{Dt}\{\Delta\} + [K]\{\Delta\} = \{F\} + \{f\}. \tag{3.3.9}$$

3.3.2 Discretized weak form of moisture diffusion

The discretization of the weak form for moisture diffusion is derived by introducing a finite element mesh of the mid-surface $S(p)$ of the encapsulant layer. In principle, since a staggered geometrical multiscale solution scheme is adopted, the spacing of the mesh used to solve moisture diffusion can be different from that used for the discretization of the thermo-elastic problem by interface elements. In that case, a projection of the nodal temperatures from the discretized thermo-elastic problem to the nodes of the mesh used to solve moisture diffusion has to be performed via a suitable interpolation scheme. In the sequel, without any loss of generality, we consider a finite element discretization for moisture diffusion coincident with the middle surface discretization of each interface element, i.e., $S(p) \approx \bigcup_e S_e$.

By introducing the shape functions Ψ_a, the water concentration in a generic point of coordinates (x_1, x_2) and at a time t is

$$C(x_1, x_2, t) = \sum_{a=1}^{S(e)} \Psi_a(\xi_1, \xi_2) C_a(t) \tag{3.3.10}$$

Introducing Eq.(3.3.10) into (3.2.3), we obtain:

$$\sum_e \int_{S_e} D C_a \frac{\partial \Psi_a}{\partial x_I} \frac{\partial \Psi_b}{\partial x_I} \delta C_b \mathrm{d}A + \sum_e \int_{S_e} \frac{\partial C_a}{\partial t} \Psi_a \Psi_b \delta C_b \mathrm{d}A = 0 \tag{3.3.11}$$

providing the following matrix form:

$$\sum_e \{\delta C\}^T [B_e] \{C_e\} + \sum_e \{\delta C_e\}^T [A_e] \frac{D}{Dt} \{C_e\} = 0 \tag{3.3.12}$$

where the expression for the matrices $[A_e]$ and $[B_e]$ is detailed in the Appendix, and $\{C_e\} = (C_1, \ldots, C_{S(e)})^{\mathrm{T}}$ is the vector collecting the nodal concentrations.

Introducing as previously the global node vector $\{C\}$ of unknowns and the localization matrix $[L_e]$ such that:

$$\{C_e\} = [L_e] \{C\} \tag{3.3.13}$$

the assembling of the global matrices leads to:

$$[B] = \sum_e [L_e]^T [D_e][L_e], \quad [A] = \sum_e [L_e]^T [A_e][L_e]$$

providing a linear system of ordinary differential equations:

$$[A]\frac{D}{Dt}\{C\} + [B(t)]\{C\} = \{0\} \tag{3.3.14}$$

Note that the matrix $[B]$ is time dependent because it contains the diffusivity D which changes with time according to (3.1.15).

3.4 Proposed numerical solution scheme

To solve numerically the system (3.3.9) resulting from the thermo-mechanical problem, we adopt an Euler backward implicit scheme so that:

$$\frac{D}{Dt}\{\Delta\}^{n+1} \approx \frac{1}{\Delta t}\left(\{\Delta\}^{n+1} - \{\Delta\}^{n}\right) \tag{3.4.1}$$

where $n = 1, 2, \ldots, N$ and $t^n = t^{n-1} + \Delta t$. Hence, Eq.(3.3.9) becomes:

$$\frac{1}{\Delta t}[D]\left(\{\Delta\}^{n+1} - \{\Delta\}^{n}\right) + [K]\{\Delta\}^{n+1} = \{F\}^{n+1} \tag{3.4.2}$$

which is a nonlinear system of equations in the unknown $\{\Delta\}^{n+1}$, where the nonlinearity relies in the load vector due to the nonlinear relations between the cohesive tractions and the displacement opening and sliding displacemets, and between the heat flux and the temperature jump at the polymeric interfaces.

This problem is solved iteratively using a Newton-Raphson scheme. At the iteration $k+1$ we have an approximation $\{\Delta\}_{(k)}^{n+1}$ for $\{\Delta\}^{n+1}$ and we seek for a better approximation $\{\Delta\}_{(k+1)}^{n+1}$ such that:

$$\{\Delta\}_{(k+1)}^{n+1} = \{\Delta\}_{(k)}^{n+1} + \{d\Delta\}_{(k)}^{n+1} \tag{3.4.3}$$

By introducing $\{\Delta\}_{(k)}^{n+1}$ into $\{F\}^{n+1}$, we obtain $\{F\}_{(k)}^{n+1}$. Linearization of $\{F\}_{(k+1)}^{n+1}$ leads to:

$$\{F\}_{(k+1)}^{n+1} = \{F\}_{(k)}^{n+1} + \left[\frac{\partial\{F\}}{\partial\{\Delta\}}\right]_{(k)}^{n+1} \{d\Delta\}_{(k)}^{n+1} \tag{3.4.4}$$

By substituting this expression back to the system (3.4.2) and rearranging the various terms, leads:

$$\left(\frac{1}{\Delta t}[C]+[K]-\left[\frac{\partial\{F\}}{\partial\{\Delta\}}\right]^{n+1}_{(k)}\right)\{d\Delta\}^{n+1}_{(k)}=- \tag{3.4.5}$$

$$\frac{1}{\Delta t}[C]\left(\{\Delta\}^{n+1}_{(k)}-\{\Delta\}^{n}\right)-[K]\{\Delta\}^{n+1}_{(k)}+\{F\}^{n+1}_{(k)} \tag{3.4.6}$$

where the left hand side is the so-called residual vector, $\{R\}^{n+1}_{(k)}$, so that we can write:

$$\left(\frac{1}{\Delta t}[C]+[K]-[T]^{n+1}_{(k)}\right)\{d\Delta\}^{n+1}_{(k)}=\{R\}^{n+1}_{(k)} \tag{3.4.7}$$

where:

$$\begin{aligned}[T]^{n+1}_{(k)}=\left[\frac{\partial\{F\}}{\partial\{\Delta\}}\right]^{n+1}_{(k)}=\sum_e[L_e]^T\left[\frac{\partial\{F_e\}}{\partial\{\Delta_e\}}\right]^{n+1}_{(k)}[L_e]=\\ \sum_e[L_e]^T\,[T_e]^{n+1}_{(k)}\,[L_e]\end{aligned} \tag{3.4.8}$$

and $[T_e]^{n+1}_{(k)}$ is given by:

$$\begin{aligned}[T_e]^{n+1}_{(k)}=&[P]^T\begin{bmatrix}[T_e^{uu}] & [T_e^{u\theta}]\\ [T_e^{\theta u}] & [T_e^{\theta\theta}]\end{bmatrix}^{n+1}_{(k)}[P]=\\ &[P]^T\begin{bmatrix}\left[\frac{\partial\{f_e^u\}}{\partial\{U_e\}}\right] & \left[\frac{\partial\{f_e^u\}}{\partial\{\Theta_e\}}\right]\\ \left[\frac{\partial\{f_e^\theta\}}{\partial\{U_e\}}\right] & \left[\frac{\partial\{f_e^\theta\}}{\partial\{\Theta_e\}}\right]\end{bmatrix}^{n+1}_{(k)}[P]\end{aligned} \tag{3.4.9}$$

The various terms entering Eq.(3.4.9) are reported in the Appendix.

Once temperature and displacements are computed at a given time step n, these nodal results are transferred to the discretized moisture diffusion problem. Its solution is then performed by using an Euler backward time integration scheme with the same partition of the temporal interval $[0,t_f]$ as for the thermo-mechanical problem. For $n=1,\dots,N$ time steps Δt, we solve the linear system of equations:

$$\left(\Delta t[B]^{n+1}+[A]\right)\{C\}^{n+1}=[A]\{C\}^n \tag{3.4.10}$$

where:

$$[B_e]_{ab}^{n+1} = \int_{S_e} D(\langle\Theta\rangle^{n+1}, [[U_3]]^{n+1}) \frac{\partial \Psi_a}{\partial x_I} \frac{\partial \Psi_b}{\partial x_I} \mathrm{d}A \tag{3.4.11}$$

are computed using the values $\langle\Theta\rangle^{n+1}, [[U_3]]^{n+1}$ obtained from the thermo-elastic problem.

The algorithm for the proposed time integration with a staggered scheme is detailed in Algorithm 1. The Newton-Raphson iteration is performed until machine precision is achieved, i.e., up to a tolerance in the norm of the residual vector $\mathrm{tol} = 1 \times 10^{-15}$.

The time-dependency of the visco-elastic constitutive equation (3.1.9) requires the use of a history variable $\{h_v\}$ for all the nodes of the finite element mesh for the thermo-mechanical problem. To model relaxation, this variable is set to zero at any change of temperature (state variable), while it is updated by the current time increment if the temperature remains constant with respect to the previous time step, within a given tolerance tol_2. This method allows the simulation of the thermo-viscoelastic behavior of polymeric materials when the temperature-time superposition principle does not apply, for instance due to a change of microstructure by varying temperature as it happens in the case of epoxy-vinil-acetate used in photovoltaics.

3.5 Application to photovoltaics

In this section we propose the simulation of the two tests prescribed by international standars (61215), namely the dump heat test and the humidity freeze test. While the former allows the complete uncoupling between the solution of the thermo-mechanical problem from moisture diffusion and a closed form solution useful for benchmarking, the latter requires the present fully-coupled solution scheme. Moreover, the role of a temperature dependent diffusion coefficient and the role of cohesive cracks in Silicon are investigated, in comparison to experimental results.

Data: ρ^m, c^m, C^m_{IJLK}, k^m, δ^c_I, α, a, k_0, h, A, E_a, R, T_0, Δt, N
Initialize: $\mathrm{tol}_1 = 1 \times 10^{-15}$, $\mathrm{tol}_2 = 0.01$, $\mathrm{norm} = 1$, $\{h_v^1\} \leftarrow \{0\}$
Result: Find $U, \Theta, [[U]], [[\Theta]], C$
Build mesh of the thermo-elastic problem and initialize boundary conditions: U_I^*, t_I^*, Θ^*, q^*;
Form load vector: $\{F\}^0$;
for $n = 1, \ldots, N$ time steps **do**
  $\{F\}^n \leftarrow \{F\}^{n+1}$;
  while $(\mathrm{norm} \geq \mathrm{tol}_1)$ **do**
    $[T]^{n+1}_{(k-1)} \leftarrow [T]^{n+1}_{(k)}$, where $[T]^{n+1}_{(k)}$ is computed based on $\{h_v^n\}$;
    $\{R\}^{n+1}_{(k-1)} \leftarrow \{R\}^{n+1}_{(k)}$;
    $\{\Delta\}^{n+1}_{(k+1)} \leftarrow \{\Delta\}^{n+1}_{(k)} + \left(\dfrac{[C]}{\Delta t} + [K] - [T]^{n+1}_{(k)}\right)^{-1} \{R\}^{n+1}_{(k)}$;
    $\mathrm{norm} \leftarrow \|\{R\}^{n+1}_{(k)}\|$
  end
  $\{U\}^n \leftarrow \{U\}^{n+1}$;
  $\{\Theta\}^n \leftarrow \{\Theta\}^{n+1}$;
  if $(\|\{\Theta\}^{n+1} - \{\Theta\}^n\| > \mathrm{tol}_2)$ **then**
    $\{h_v^{n+1}\} \leftarrow \{0\}$;
  else
    $\{h_v^{n+1}\} \leftarrow \{h_v^n\} + \{\Delta t\}$;
  end
  $[B]^n \leftarrow [B]^{n+1}(\langle\Theta\rangle^{n+1}, [[U_3]]^{n+1})$;
  $\{C\}^n \leftarrow \{C\}^{n+1}$;
end

Algorithm 1: Numerical scheme for the solution of the hygro-thermo-elastic problem with a staggered approach.

3.5.1 Damp heat test

Let us consider a laminate of span $L = 125$ cm and made of a Glass-Glass structure separated by EVA as in Fig.16. The thickness of each glass is 3 mm, while the thickness of the EVA is 0.5 mm. In this laminate, moisture is diffusing from the free edges towards the centre, since glass is not permeable to moisture.

As far as the initial and boundary conditions, let us consider the prescriptions by international standards (61215) for the damp heat test, that is, a constant temperature of $85°$ C and an air relative humidity of 85%. This relative humidity corresponds to a moisture content $c^* = 0.55$ g/cm^3 imposed at the free edges of the laminate, i.e., for $x_1 = 0$ and $x_1 = L$, where x_1 is the distance from the edge of the PV module.

Since temperature is held constant, the problem of diffusion can be solved independently from the thermo-elastic problem, considering a constant diffusivity $D = 5 \times 10^{-5}\text{cm}^2/\text{s}$ corresponding to $85°$ C. For this special case, the analytical solution to the problem was obtained in (Kem14) and it is used as a benchmark for our computational scheme:

$$c(x_1, t) = c^* - \frac{4c^*}{\pi} \sum_{k=0}^{\infty} \frac{1}{(2k+1)} \sin\left(\frac{(2k+1)\pi x_1}{L}\right) \times \exp\left(-\frac{(2k+1)^2 \pi^2 D t}{L^2}\right) \tag{3.5.1}$$

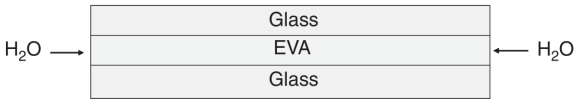

Figure 16: Sketch of the damp heat test.

After 1000 hours, the predicted moisture concentration is shown in Fig.17(a) and its distribution in the EVA layer matches exactly the reference one in Fig.17(b)

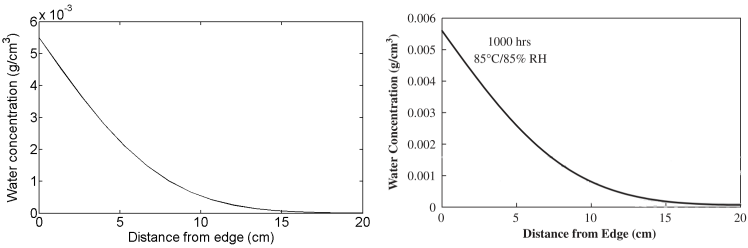

(a) (b)

Figure 17: Moisture concentration in the encapsulant after 1000 h. (a) Numerical simulation; (b) analytical solution by (Kem14).

3.5.2 Humidity freeze test

In this test requested by international standards (61215), PV modules simply supported along their edges are subjected to a cycling temperature from -40° C up to 85° C with the following ramps (see also the sketch in Fig.18):

$$\theta^*(t) = \begin{cases} \dfrac{\theta_1^*}{t_1^*} t & 0 \le t < t_1^* \\ \theta_1^* & t_1^* \le t < t_2^* \\ \theta_2^* - \dfrac{\theta_1^* - \theta_2^*}{t_3^* - t_2^*}(t_3^* - t) & t_2^* \le t < t_3^* \\ \theta_2^* & t_3^* \le t < t_4^* \\ \dfrac{\theta_2^*}{t_5^* - t_4^*}(t_5^* - t) & t_4^* \le t < t_5^* \end{cases}$$

where $\theta_1^* = 85^\circ$ C , $\theta_2^* = -40^\circ$ C, and $t_1^* = 0.5$ h, $t_2^* = 1.5$ h, $t_3^* = 2.5$ h, $t_4^* = 3.5$h, $t_5^* = 4.5$h.

The relative humidity in the air is kept constant at 85% for the range of temperatures where its control is thermodynamically feasible without condensation.

Due to a non constant temperature boundary condition, this problem is much more difficult to be simulated as compared to the damp heat test. In particular, the cohesive properties of the EVA have to be updated during the simulation, as well as its diffusivity. More specifically, as far

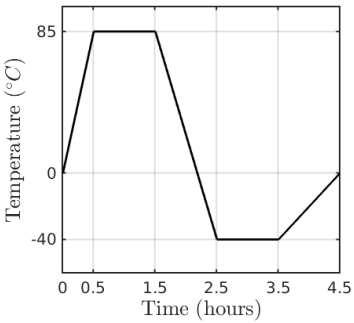

Figure 18: Temperature profile of θ^* imposed inside the climate chamber during the humidity freeze test.

as the Young's modulus of the EVA is concerned, the parameters $\alpha(T)$ and $a(T)$ are herein considered to be temperature dependent as experimentally evaluated in (MP11) and interpreted via a fractional calculus model in (MP15), see the plot for $\alpha(T)$ and $E(T)$ in Fig.19.

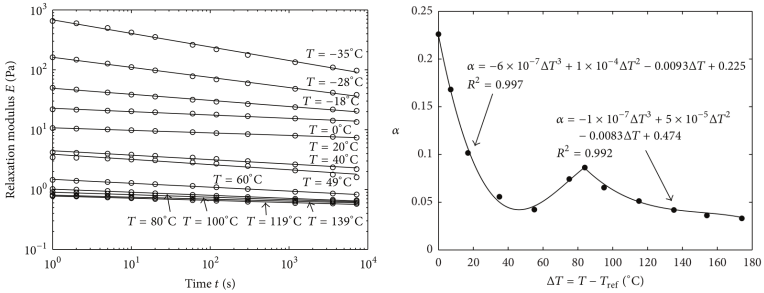

(a) (b)

Figure 19: (a) EVA relaxation modulus vs. time at various temperatures in a double logarithmic scale; (b) Temperature dependent fractional exponent $\alpha(T)$, adapted from (MP15).

Regarding the diffusive properties, we consider the expression of $D(T)$ for EVA as reported in (Kem14) and shown in Fig.20. Such trends can be fitted according to the Arrhenius type equation (3.1.15).

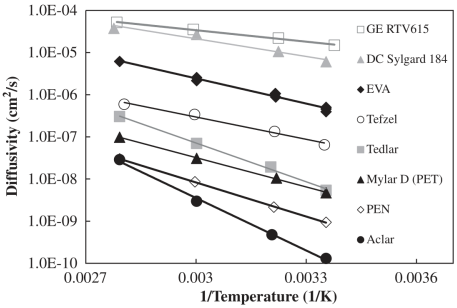

Figure 20: Diffusivity of various encapsulant materials vs. the inverse of temperature, adapted from (Kem14).

The critical crack opening, δ_3, to be assigned to the cohesive zone model can be estimated from published experimental data in (FN14a) reporting the variation of the Mode I fracture energy with temperature. Since the fracture energy G_I is the area below the traction-separation curve, the following relation holds:

$$G_I = \int_0^{\delta_3^c} t_3([[u_3]], \langle\theta\rangle) d[[u_3]] = \frac{1}{2} \frac{(\delta_3^c)^2}{h_{EVA}} E_{EVA}(t, T)$$

Hence, the $G_I(T)$ experimental data can be converted in $\delta_3^c(T)$ data based on the known temperature dependency of the Young's modulus of EVA as in Fig. 8(a), evaluated for the asymptotic condition of an infinite time. Based on these data, we obtain the correlations shown in Fig.21 and used as input for the numerical simulations.

A sketch of the cross-section of a PV mini-module simulated in the present study and containing 3 solar cells is shown in Fig.22. The lateral size of each Silicon cell is 125 mm and the the interspace between two cells is 4 mm. The module is made of a glass superstrate with thickness $h_G = 4$ mm, an encapsulating polymer layer (EVA) with thickness $h_{EVA} = 0.5$ mm, the silicon solar cell with thickness $h_{SI} = 0.166$ mm, another layer of EVA with the same thickness as the previous one, and finally a thin backsheet made of an ethylene tetrafluoroethylene core with silicon nitride coating (isovolta Icosolar T 2754), with thickness $h_{BS} = 0.1$

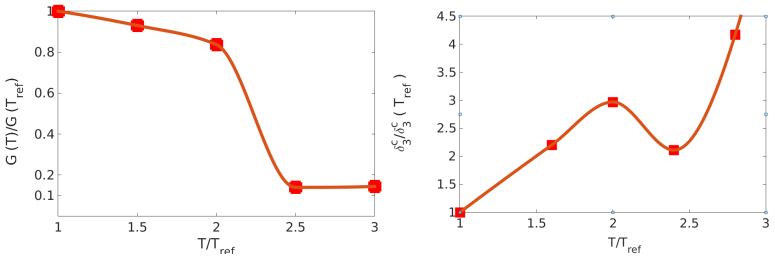

(a) (b)

Figure 21: (a) EVA cohesive energy from (FN14a); (b) Critical gap opening vs. temperature. ($T_{\text{ref}} = 25^\circ$ C).

mm. Thermal and mechanical parameters of each layer are collected in Tab.2. Since moisture penetrates from the backsheet and percolates along the interspace between solar cells, in the numerical simulations it is possible to impose a constant value of moisture concentration, c^*, directly at the boundary of each solar cell embedded in the PV module.

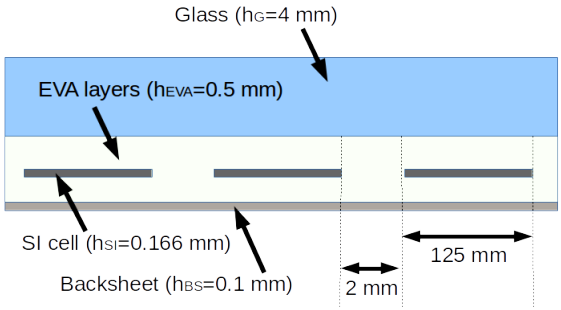

Figure 22: Sketch of the cross-section of a PV mini-module used in the simulation (not in scale).

The temperature distribution inside a portion of the PV module cross-section near one of the free boundaries is shown in the contour plots in Fig.23 for selected time steps. After the first ramp from 0° C to 85° C completed after 0.5 hours, heat has diffused inside the panel and temperature is almost uniform everywhere and equal to 85° C. During the

Table 2: Material parameters for the layers

	E GPa	α	ρ Kg/m^3	c_ε W/mK	k J/mKg
Glass	73	$8e-6$	2300	500	0.8
Si	130	$2.49e-6$	2500	715	148
B.S.	2.8	$5.04e-5$	1000	300	0.36

subsequent decreasing ramp from 85° C to -40° C, the Silicon cells and the EVA around them remain warmer than the other component. This temperature mismatch progressively shrinks during the further stage of the simulation at constant temperature θ^*. This trend is quantified in Fig.24 by plotting the temperature along a vertical line at $x_1 = 2$ mm from the free edge of the laminate, through the panel thickness.

The evolution of moisture concentration in the encapsulant vs. time by using a time-dependent diffusivity is shown in Fig.25(a). The same simulation with a constant diffusivity $D = 5 \times 10^{-5}$ cm^2/s corresponding to 85°C is shown for comparison in Fig.25(b). As it can be noticed, the proper update of the diffusivity based on the actual temperature of EVA during the simulation provides very different results from those based on a constant diffusivity. In particular, moisture diffusion is a much slower phenomenon than what expected by the approach presented in (Kem14), which is based on the use of a constant diffusivity equal to that at the maximum temperature.

(a) After 0.5 hours

(b) After 1.5 hours

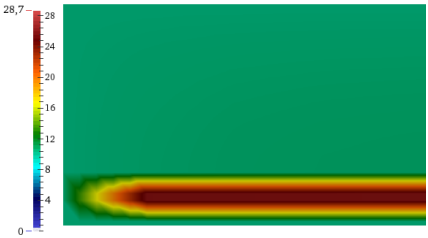

(c) After 2 hours

(d) After 2.25 hours

Figure 23: Contour plot of temperature inside the module after selected time steps.

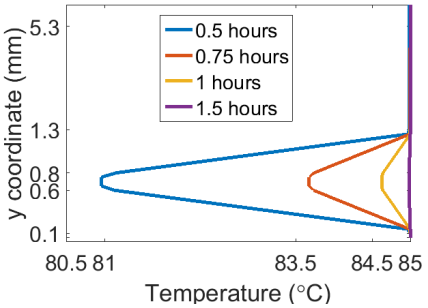

Figure 24: Evolution of temperature over a vertical line at $x_1 = 2$ mm from the lateral side, during the first ramp from $0°C$ to $85°C$.

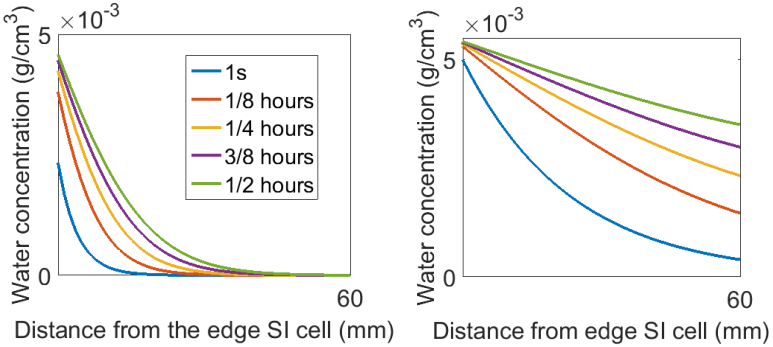

(a) D dependent on T (b) $D = D(85°C)$

Figure 25: Evolution of moisture concentration in the EVA encapsulant for an updated or a constant diffusivity.

Chapter 4

Reaction-diffusion problems in polymer degradation

Poly(ethylene-*co*-vinyl acetate) (EVA) is one of the most widely used materials for photovoltaic encapsulants, due to its chemico-physical characteristics and low cost. Although the formulation used during module lamination is stabilized with chemical additives, the EVA copolymer suffers of thermo-photo-oxidative degradation, due to the prolonged exposure of photovoltaic (PV) installations to UV light, environmental agents and the high working temperature of the PV module. After degradation, EVA polymer chains lose atoms and small molecules, such as acetic acid, and those changes at the macromolecular level lead to a deterioration of the optical properties of the encapsulant (yellowing and browning), the corrosion of electric connections and the formation of snail trails. Moreover, its permeability to moisture induces a progressive oxidation of the grid line over the solar cell surface and a reduction of mechanical adhesion and sealing (Kem06; FN14b; PL16). A thorough explanation of chemical phenomena occurring during EVA degradation, together with interesting experimental data, were provided in (Per97; Per96; FP92; BR08). However, the existing computational models describing the behavior

of EVA encapsulant in weathering conditions are mostly focusing on the analysis of water absorption and diffusion (Kem06; PH15), while no method is able to comprehensively provide the time evolution of the chemical species and all the other physical characteristics of EVA for any weathering condition. This is indeed relevant for the PV community for at least two reasons: (i) assess the impact of degradation of PV installations in climate zones other than the European one; (ii) quantitatively assess the amount of chemical degradation of EVA in accelerated aging tests and compare with real environmental conditions. Motivated by these needs, in line with the open problems foreseen by the Technical Committee of the Task 13 on *Performance and Reliability of Photovoltaic Systems* of the International Energy Agency to whom one author is member, a novel computational tool is herein proposed to predict the evolution in time of chemical reactions and diffusion of species inside the encapsulant for any generic weathering condition and relate these phenomena to the loss of properties of EVA.

4.1 Degradation phenomena in EVA copolymers and their mathematical description

Poly(ethylene-*co*-vinyl acetate) copolymers (EVA) used as encapsulant in photovoltaic modules are macromolecular materials composed of ethylene (ET) and 28-33% in weight of vinyl acetate (VAc). The initiation step in ET degradation is represented by the generation of radical species (BR) and can be schematized as follows:

$$ET \xrightarrow{k_1} R^{\bullet} + H^{\bullet}. \tag{4.1.1}$$

The formed $H^{\bullet}$ radical diffuses very slowly and it migrates towards non-crystalline regions, where can react with other radical species present in the polymer. The radical $R^{\bullet}$ is formed in the polymer backbone and therefore it does not diffuse.

Degradation can further propagate via two different and separate mechanisms. The first mechanism is due to the high reactivity of the

radical site in the backbone and to the presence of $H^{\bullet}$. The second propagation mechanism occurs in the presence of oxygen absorbed from the external environment, causing the formation of carbonyl groups in the backbone and free water molecules (RY10). Schematization of these reactions is:

$$R^{\bullet} \xrightarrow{k_2} U + H^{\bullet} \tag{4.1.2a}$$

$$R^{\bullet} + O_2 \xrightarrow{k_3} C_b + H_2O \tag{4.1.2b}$$

The products U and C_b denote the double-bonds and the carbonyl groups formed after Reaction 2 and 3 respectively.

The VAc fraction shows two different degradation mechanisms, mainly due to the lost of acetate units (LR04). Also in this case, reactions follows a radical mechanism that can lead to the formation of acetaldehyde, through a Norrish type I mechanism, or acetic acid, based on a Norrish type II mechanism (Nor10). These reactions are schematized as:

$$VAc \xrightarrow{k_4} C_b + CH_3CHO \tag{4.1.3a}$$

$$VAc \xrightarrow{k_5} U + CH_3COOH \tag{4.1.3b}$$

where C_b and U denote carbonyl groups and unsaturations formed within the backbone after Reaction 4 and 5, while CH_3CHO and CH_3COOH are small produced molecules that can diffuse.

The overall concentration of carbonyl groups formed by Reactions 3 and 4 is given by their sum, as well as the overall concentration of unsaturations, which is the sum of products of Reactions 2 and 5. Carbonyl groups formed from ET and VAc can further degrade giving chain scission:

$$\begin{aligned} C_b &\xrightarrow{k_6} C_b^{\bullet} + R_t^{\bullet} \\ C_b &\xrightarrow{k_7} C_{bt} + U_t \end{aligned} \tag{4.1.4}$$

causing a reduction of the molecular weight of the EVA polymer. Considering that the native EVA is cross-linked, products of Reactions 6 and 7 are supposed to be large molecules and thus they do not diffuse.

Finally, termination reactions occur when two free radicals react between them. In the case of EVA, radicals are formed in the backbone

polymer and are not able to diffuse, reducing the possibility to provide this kind of reactions. Thus, in this work, the termination step is neglected.

4.1.1 Mathematical description of the reaction kinetics and diffusion of species

The unknown variables of the system are the chemical species responsable for the browning process, i.e. $R^\bullet$, U, $H^\bullet$, C_b, $C_b^\bullet$, C_{bt}, O_2 and H_2O. The reactions of theese quantities are modeled through the following mechanism:

$$ET \xrightarrow{k_1} R^\bullet + H^\bullet \tag{4.1.5a}$$

$$R^\bullet \xrightarrow{k_2} U + H^\bullet \tag{4.1.5b}$$

$$R^\bullet + O_2 \xrightarrow{k_3} C_b + H_2O \tag{4.1.5c}$$

$$VAc \xrightarrow{k_4} C_b + CH_3CHO \tag{4.1.5d}$$

$$VAc \xrightarrow{k_5} U + CH_3COOH \tag{4.1.5e}$$

$$C_b \xrightarrow{k_6} C_b^\bullet + R_t^\bullet \tag{4.1.5f}$$

$$C_b \xrightarrow{k_7} C_{bt} + U_t \tag{4.1.5g}$$

The reaction rates are modeled by temperature-dependent Arrhenius type equations:

$$k_I(T) = k_I^0 \exp\left(\frac{-E_I}{RT}\right),\ I = 1, \ldots, 7. \tag{4.1.6}$$

The resulting partial differential equations including also diffusion where it is the case read:

$$\frac{\partial R^{\bullet}}{\partial t} = k_1 ET - k_2 R^{\bullet} - k_3 R^{\bullet} O_2 \tag{4.1.7a}$$

$$\frac{\partial U}{\partial t} = k_2 R^{\bullet} + k_5 VAc \tag{4.1.7b}$$

$$\frac{\partial C_b}{\partial t} = k_3 R^{\bullet} O_2 + k_4 VAc - (k_6 + k_7) C_b \tag{4.1.7c}$$

$$\frac{\partial C_b^{\bullet}}{\partial t} = k_6 C_b \tag{4.1.7d}$$

$$\frac{\partial C_{bt}}{\partial t} = k_7 C_b \tag{4.1.7e}$$

$$\frac{\partial O_2}{\partial t} - D_7 \Delta O_2 = -k_3 R^{\bullet} O_2 \tag{4.1.7f}$$

$$\frac{\partial H_2 O}{\partial t} - D_8 \Delta H_2 O = k_3 R^{\bullet} O_2 \tag{4.1.7g}$$

This set of differential equations form a reaction-diffusion (RD) system defined in the space-time domain $R \times [0, t_f]$, where R is a region occupied by (a portion) of the EVA layer. It consists of 5 non diffusive ordinary differential equations and 2 diffusive partial differential equations. The diffusivities are temperature dependent:

$$D_J(T) = D_J^0 \text{exp}\left(\frac{-E_J^d}{RT}\right), J = 6, 7. \tag{4.1.8}$$

The previous system is finally completed by the following additional reaction equations:

$$\frac{\mathrm{d}ET}{\mathrm{d}t} = -k_1 ET, \tag{4.1.9a}$$

$$\frac{\mathrm{d}VAc}{\mathrm{d}t} = -(k_3 + k_4) VAc, \tag{4.1.9b}$$

that can be solved in advance independently from the other reaction-diffusion equations, so species ET and VAc are known functions of time:

$$ET(t) = ET_0 \text{ exp}\,(-k_1 t)$$
$$VAc(t) = VAc_0 \text{ exp}\,(-(k_3 + k_4) t)$$

where ET_0 and VAc_0 are initial concentrations. Dirichlet boundary conditions for the reaction-diffusion system involving the diffusing species on the boundary $\partial R_D \times [0, t_f]$ are prescribed. Using an abstarct notation the previous system can be rewritten in vectorial form as follows:

$$\begin{aligned} \frac{\partial \mathbf{C}(t)}{\partial t} - \mathbf{div}\left(\mathbf{D}(\mathbf{C}(t))\nabla \mathbf{C}(t)\right) &= \mathbf{F}(\mathbf{C}(t)), \text{ in } R \times [0, t_f] \\ \mathbf{C}(t) &= \mathbf{G}^*(t), \text{ on } \partial R_D^{\mathbf{C}} \times [0, t_f] \\ \mathbf{C}(0) &= \mathbf{C}_0, \text{ on } R \end{aligned} \tag{4.1.10}$$

where $\mathbf{C}(t) = (C_1(t), \ldots, C_7(t))^{\mathrm{T}} = (R^{\bullet}, U, C_b, O_2, H_2O, C_b^{\bullet}, C_{bt})^{\mathrm{T}}$ is the unknown vector of species, $\mathbf{D}$ is the diffusion matrix having on its diagonal the diffusion constants $D_J(T)$, $\mathbf{F}$ is the reaction vector and $\mathbf{G}^*$ is the boundary condition vector imposed on $\partial R_D^{\mathbf{C}}$, the Dirichlet part of the domain. Multiplying the previous system (4.1.10) by a test function $\mathbf{S}$ and integrating over the domain, using the divergence theorem and the boundary condition of zero flux, the weak formulation of the reaction-diffusion system (4.1.10) is: for all $t \in [0, t_f]$ find the concentration vector $\mathbf{C}(t)$ such that it satisfies:

$$\begin{aligned} &\int_R \partial_t \mathbf{C}(t) \cdot \mathbf{S} \, \mathrm{d}V + \int_R \mathbf{D}(\mathbf{C}(t))\nabla \mathbf{C}(t) : \nabla \mathbf{S} \, \mathrm{d}V = \\ &\int_R \mathbf{F}(\mathbf{C}(t)) \cdot \mathbf{S} \, \mathrm{d}V, \quad \forall \, \mathbf{S}. \end{aligned} \tag{4.1.11}$$

4.2 Finite element discretization

The domain R occupied by the portion of EVA material is discretized into a finite number of elements $R(e)$ so that:

$$R \approx \bigcup_e R(e) \tag{4.2.1}$$

By introducing shape functions, the finite element approximation of each component of $\mathbf{C}$ the concentration vector reads:

$$C_K(x_1, x_2, x_3, t) = \sum_{a=1}^{N(e)} \Phi_a(\xi_1, \xi_2, \xi_3) C_{aK}(t), \quad 1 \leq K \leq 7,$$

where $\{\Phi_a(\xi_1, \xi_2, \xi_3)\}_{a=1}^{N(e)}$ is a basis of local linear shape functions defined in the natural reference system $-1 \leq \xi_1, \xi_2, \xi_3 \leq +1$ and $N(e)$ is the number of element nodes which is equal to 3 in the case of linear triangular Lagrange elements. After introducing this expression in the weak form, its discretized version is obtained:

$$\sum_e \int_{R(e)} \Phi_a \Phi_b \frac{\partial C_{aI}}{\partial t} S_{aI} \mathrm{d}V + \sum_e \int_{R(e)} D_{IJ}(\mathbf{C}) \frac{\partial \Phi_a}{\partial x_L} \frac{\partial \Phi_b}{\partial x_L} C_{aI} S_{bJ} \mathrm{d}V = \sum_e \int_{R(e)} F_I(\mathbf{C}) \Phi_a S_{aI} \mathrm{d}V = 0 \tag{4.2.2}$$

The expressions of matrices and vectors entering the discretized weak form (4.1.11) at the element level are:

$$[M_e]_{aIbJ} = \int_{R(e)} \Phi_b \Phi_a \mathrm{d}V, \tag{4.2.3a}$$

$$[K_e]_{aIbJ} = \int_{R(e)} D_{IJ}(\mathbf{C}) \frac{\partial \Phi_b}{\partial x_K} \frac{\partial \Phi_a}{\partial x_K} \mathrm{d}V, \tag{4.2.3b}$$

$$\{F_e\}_{aI} = \int_{R(e)} F_I(\mathbf{C}) \Phi_a \mathrm{d}V, \tag{4.2.3c}$$

where the Einstein summation notation has been adopted. Local matrices and vectors are then assembled over all elements $R(e)$ as customary to obtain global matrices and vectors leading to the differential system:

$$[M] \frac{D}{Dt} \{C\} + [K]\{C\} = \{F\} \tag{4.2.4}$$

where $[M]$ and $[K]$ result from the finite element discretisation and assembly, $\{F\}$ is the reaction vector and $\{C\}$ is the nodal concentration vector.

4.3 Proposed numerical solution scheme

Adopting an implicit Euler time integration scheme, one must solve at each time step t^n the following algebraic set of equations:

$$[M]\frac{\{C\}^{n+1}-\{C\}^n}{\Delta t}+[K]\{C\}^{n+1}=\{F\}^{n+1}. \tag{4.3.1}$$

The reaction term can be treated in an explicit manner, considering $\mathbf{F}(\mathbf{C}^n)$ instead of $\mathbf{F}(\mathbf{C}^{n+1})$.

In the case of a diffusion constitutive relation where the diffusivities of species in the polymer are functions of their concentrations, viz.:

$$\tilde{D}_J(C_J,T)=D_J(T)\;\tilde{D}_J^0\exp\left(\gamma_J C_J\right),\; J=6,7, \tag{4.3.2}$$

this leads to a diffusivity matrix $\mathbf{D}(\mathbf{C})$ which is not a constant, but it is a nonlinear function of $\mathbf{C}$. Hence, the Newton-Raphson iterative procedure with fully implicit approximation of the reaction vector is proposed to solve this problem. Setting the residual vector:

$$\{R\}^n=\frac{1}{\Delta t}[M]\left(\{C\}-\{C\}^n\right)+[K(\{C\})]\{C\}-\{F(\{C\})\}, \tag{4.3.3}$$

in components, at the element level, reads:

$$\begin{aligned}\{R_e\}^n_{aI}=&\frac{1}{\Delta t}[M_e]_{aIbJ}\left(\{C_e\}_{bJ}-\{C_e\}^n_{bJ}\right)+\\&\left(\int_{R(e)}D_{IJ}(\mathbf{C}_e^{n+1})\frac{\partial\Phi_b}{\partial x_K}\frac{\partial\Phi_a}{\partial x_K}\,\mathrm{d}V\right)\{C_e\}_{bJ}-\\&\int_{R(e)}F_I(\mathbf{C}_e^{n+1})\Phi_a\,\mathrm{d}V\end{aligned}$$

Suppose that at time iteration n is given $\{C\}^{n+1}_{(k)}$, which is an approximation of $\{C\}^{n+1}$, then it is solved the linearized system:

$$\left[\frac{\partial\{R\}}{\partial\{C\}}\right]^{n+1}_{(k)}\{\Delta C\}^{n+1}_{(k)}=-\{R\}^{n+1}_{(k)}, \tag{4.3.4}$$

where the components of the tangent operator are:

$$\left[\frac{\partial\{R_e\}^n_{aI}}{\partial\{C_e\}_{bJ}}\right] = \frac{1}{\Delta t}[M_e]_{aIbJ} + \int_{R(e)} D_{IJ}(\mathbf{C}_e^{n+1})\frac{\partial\Phi_b}{\partial x_K}\frac{\partial\Phi_a}{\partial x_K}\,\mathrm{d}V + \left(\int_{R(e)} \frac{\partial D_{IL}}{\partial C_J}(\mathbf{C}_e^{n+1})\frac{\partial\Phi_l}{\partial x_K}\frac{\partial\Phi_a}{\partial x_K}\Phi_b\,\mathrm{d}V\right)\{C_e\}_{lL} - \int_{R(e)} \frac{\partial F_I}{\partial C_J}(\mathbf{C}_e^{n+1})\Phi_a\Phi_b\,\mathrm{d}V$$

and N_h is the total number of vertices of the mesh. Given the solution of system (4.3.4), a better approximation for $\{C\}^{n+1}$ is obtained as $\{C\}^{n+1}_{(k+1)} = \{C\}^{n+1}_{(k)} + \{\Delta C\}^{n+1}_{(k)}$. This procedure is repeated until the residual norm $\|\{R\}^{n+1}_{(k)}\|$ is less than a prescribed tolerance. In the special case of a diffusion constitutive relation (4.3.2) with $\gamma_j = 0$, then the weak form (4.1.11) becomes linear.

4.4 Numerical experiments

4.4.1 Numerical scheme for the simulation of environmental degradation

In case of environmental degradation, ambient temperature $T_{\mathrm{amb}}(t)$ and relative humidity $\%RH(t)$ can be provided from real annual climate data periodically repeated to obtain profiles over 20 years, to be used as boundary conditions for the degradation simulation. These environmental data are usually provided by environmental agencies, such as Agenzia Regionale per la Protezione Ambientale (ARPA) in Italy, for different locations and with a time resolution of 1 hr.

These data, referring to the year 2010 when a very cold winter was noticed, are shown in Fig. 26. To provide a closed-form equation for the module temperature to be imposed at each time step to EVA, the experimental data are fitted according to the following expression:

$$T_{\mathrm{amb}}(t) = A_1\sin(B_1 t + C_1) + A_2\sin(B_2 t + C_2), \tag{4.4.1}$$

in order to match the sinusoidal time dependency and capture the extremal values of temperature. The module temperature can finally be

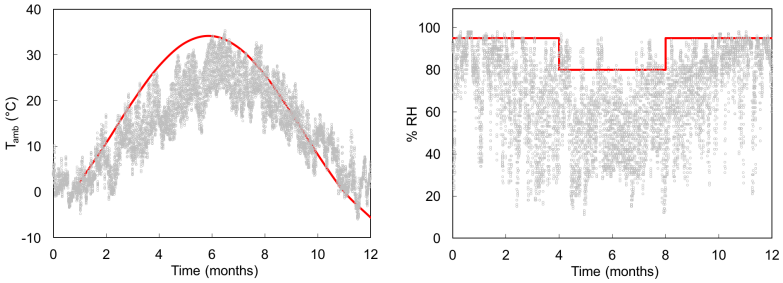

(a) Ambient temperature T_{amb} (b) Relative humidity $\%RH$

Figure 26: Experimental values and related interpolations of: (a) ambient temperature T_{amb}, (b) relative humidity percent $RH\%$.

computed from the ambient temperature as (GC14):

$$T = T_{\mathrm{amb}} + \frac{(\mathrm{NOCT} - 20) \times I_{rr}}{800}, \tag{4.4.2}$$

where T is the working temperature of the module (°C), T_{amb} is the measured external temperature (°C), $\mathrm{NOCT} = 50°\mathrm{C}$ and I_{rr} is the solar irradiance (Wm^{-1}). For practical considerations, the temperature of the EVA layer is set equal to the working temperature of the module.

On the other hand, regarding the relative humidity which displays very strong daily oscillations, two maximum values are considered as representative of the warm and cold seasons, as a worst case scenario for water uptake. Of course, any other continuous or discrete temperature and relative humidity profiles can be considered as input of the finite element algorithm, without any lack of generality.

Dirichlet boundary conditions for the reaction-diffusion system involving the diffusing species are:

$$\begin{aligned} O_2 &= O_2^*, \quad \text{on } \partial R_D^{O_2} \times [0, t_f] \\ H_2O &= S(T)\hat{\mathrm{P}}_{vp}, \quad \text{on } \partial R_D^{H_2O} \times [0, t_f] \end{aligned} \tag{4.4.3}$$

The last relation is the Henry law relating the water concentration at the boundary of the EVA layer in contact with air with the partial pressure of

the water vapour $\hat{\mathrm{P}}_{vp}$, depending on the relative humidity $\%RH(t)$. The temperature-dependent function $S(T)$ denotes the solubility:

$$S(T) = S^0 \exp\left(E_s/(RT)\right). \tag{4.4.4}$$

The geometry used for the simulation sketched in Fig. 4.4.1 presents a symmetrical, and 2- dimensional model. It is composed of a backsheet layer, followed by the encapsulation integrated with two half-sized solar cells (80 mm) which show a gap of 2 mm in between them. The atmospheric side of the back sheet layer provides the feed-in zone for the water molecules. This layer is infinitely thin and, therefore, permanently in sorption equilibrium with the air humidity of the microclimate.

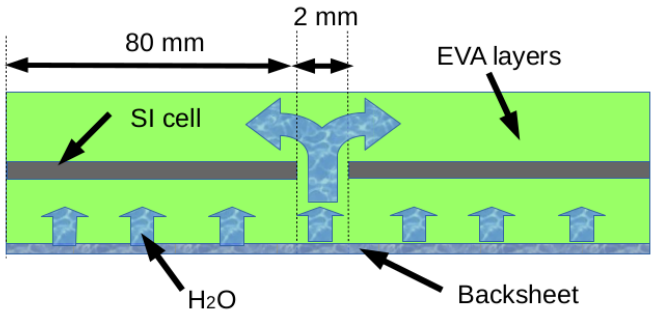

Figure 27: Sketch of the cross-section of a PV module used in the simulation (not in scale).

We solved the reaction-diffusion system (4.1.10) numerially, using the algorithm detailed in Algorithm 2. The domain R has been decomposed into 7846 finite linear triagular $\mathbb{P}_1$ elemets as shown in Figue 28.

Predicted consumption profiles of ET, VAc, C_b,... species are calculated. In Fig. 29 are reported the evolutions of concentrations ET, VAc and C_b over 20 years. Results indicate an overall degraded fraction of 0.2% after 20 years. The stepped trend is due to experimental values of temperature T, described with a sinusoidal function and influencing kinetic rates of reactions k_I.

Kinetic and diffusion parameters:
k_I^0, E_I, D_J^0, E_J^d ;
Solubility parameters: S^0, E_s
Initialize: $\{C\}^1, \text{tol}, \text{norm} = 1$
for $n = 1, \ldots, N$ time steps **do**
  Compute temperature and partial pressure
  $T^n,\ \hat{P}_{H2O}^n$;
  Kinetic constants, diffusivities and solubility
  $k_i(T^n) = k_I^0 \exp(-(E_I/(RT^n)))$;
  $D_j(T^n) = D_I^0 \exp(-(E_J^d/(RT^n)))$;
  $S(T^n) = S^0 \exp(E_s/(RT^n)))$;
  while $(\text{norm} \geq \text{tol})$ **do**
    Update reaction vector and diffusion matrix
    $\mathbf{F}_{(k)}^{n+1},\ \mathbf{D}_{(k)}^{n+1}$;
    Form the residual vector: $\{R\}_{(k)}^{n+1}$;
    Solve the linearized reaction-diffusion system:
    $\{C\}_{(k)}^{n+1} \leftarrow \{C\}_{(k)}^{n+1}$;
    $\text{norm} \leftarrow \|\{R\}_{(k)}^{n+1}\|$
  end
  Update concentration vector:
  $\{C\}^{n+1} \leftarrow \{C\}^n$;
end

Algorithm 2: Numerical scheme for the solution of the reaction-diffusion system for environmental degradation.

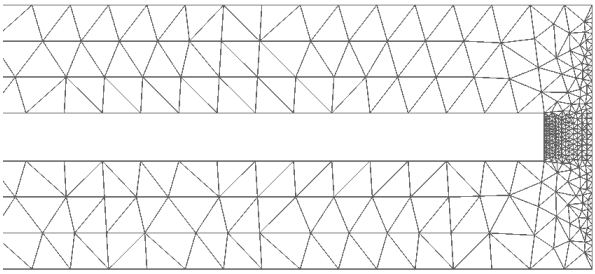

Figure 28: A zoom of the mesh used for the simulations.

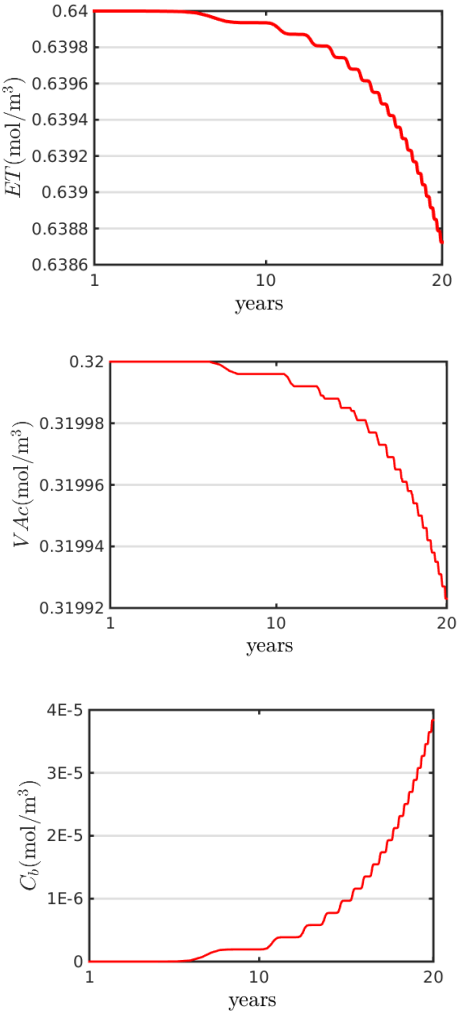

Figure 29: Change of concentration vs time of ET, VAc and C_b species in simulated environmental conditions.

Moisture uptake vs. time for a point P located in the middle of the upper left part of the region occupied by the EVA layer, is shown in

Fig.30 and presents an oscillating trend, tending towards a saturation after about 5 years. The Physical units of all the concentarions are in $[\mathrm{mol/m^{-3}}]$.

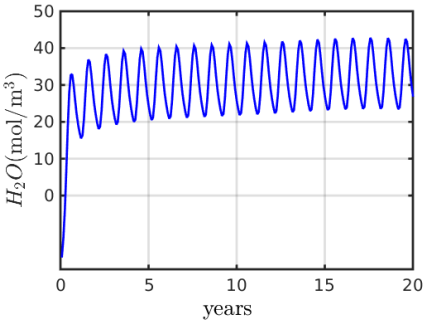

Figure 30: Evolution of the concentration of H_2O in the point P of the EVA layer for simulated environmental conditions.

The predicted values at 20 years, $R^{\bullet}(t = 20 \text{ years})$, $U(t = 20 \text{ years})$, $H^{\bullet}(t = 20 \text{ years})$, $C_b(t = 20 \text{ years})$, $C_b^{\bullet}(t = 20 \text{ years})$, $C_{bt}(t = 20 \text{ years})$, $O_2(t = 20 \text{ years})$ and $H_2O(t = 20 \text{ years})$ of the concentration vector $\mathbf{C}(t = 20 \text{ years}) = \mathbf{C}^{20 \text{ years}}$ can now be used to make prediction for the degradation process in controlled tests for durability.

4.4.2 Numerical schemes for the simulation of accelerated degradation

In the humidity-freeze test defined by the international standard IEC61215 (61215), PV modules are subjected to a cycling temperature from $-40°\mathrm{C}$ up to $85°\mathrm{C}$ according to the following ramps (see also the sketch in Fig.4.4.2):

$$T^*(t) = \begin{cases} \dfrac{T_1^*}{t_1^*}t, & 0 \le t < t_1^* \\ T_1^*, & t_1^* \le t < t_2^* \\ T_2^* - \dfrac{T_1^* - T_2^*}{t_3^* - t_2^*}(t_3^* - t), & t_2^* \le t < t_3^* \\ T_2^*, & t_3^* \le t < t_4^* \\ \dfrac{T_2^*}{t_5^* - t_4^*}(t_5^* - t), & t_4^* \le t < t_5^* \end{cases} \tag{4.4.5}$$

where $T_1^* = 85°\mathrm{C}$, $T_2^* = -40°\mathrm{C}$, and $t_1^* = 0.5$ h, $t_2^* = 1.5$ h, $t_3^* = 2.5$ h, $t_4^* = 3.5$h, $t_5^* = 4.5$h. The relative humidity in the air is kept constant

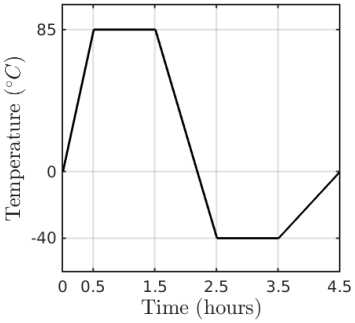

Figure 31: Profile of T^* imposed inside the climate chamber during the humidity-freeze test.

at 85% for the range of temperatures where its control is thermodynamically feasible without condensation.

In this case, temperature inside the module and especially in the EVA layer cannot be assumed homogeneous equal to the temperature inside the climate chamber, since it is rapidly varying in time. Hence, in this

case the temperature regime has to be solved and the EVA temperature has to be considered as an additional variable of the problem governed by the heat transfer diffusion equation to be coupled with the whole reaction-diffusion system:

$$\rho c \, \frac{\partial T}{\partial t} - \kappa \Delta T = Q_T(t) \, , \qquad \text{in } R \times [0, t_f] \tag{4.4.6}$$

where ρ [kg m^{-3}], κ [W m^{-1}K^{-1}] and c [J kg^{-1}K^{-1}] denote respectively the EVA density, its thermal conductivity and its heat capacity and Q_T is the internal generated heat due to reactions given by the sum of the following quantities:

$$\begin{aligned}
Q_{ET} &= \Delta H_1 k_1(T) ET, \\
Q_{R^\bullet} &= \{\Delta H_2 k_2(T) + \Delta H_3 k_3(T) O_2\} R^\bullet, \\
Q_{VAc} &= \{\Delta H_4 k_4(T) + \Delta H_5 k_5(T)\} VAc, \\
Q_{C_b} &= \{\Delta H_6 k_6(T) + \Delta H_7 k_7(T)\} C_b.
\end{aligned}$$

The model parameters ΔH_I are taken from literature.

The test geometry is the same of the environmental simulation. Boundary conditions are expressed in terms of temperature on the border of EVA, ∂R:

$$T(t) = T^*(t), \text{ in } \partial R \times [0, t_f], \tag{4.4.8}$$

where $T^*(t)$ is given by the ramps defined in Eq.(4.4.5). The characteristic velocity of the heat conduction process is ruled by the ratio $\kappa/(\rho c)$. Typical values for EVA are $\rho = 0.96$ kg/m^3, $c = 1400$ J/(kgK) and $\kappa = 0.34$ W/(mK). As compared with values of kinetic constants and diffusivities found in the literature it has to be noticed that $\kappa/(\rho c) >> k_I$ and D_J. Hence, heat conduction inside the EVA is much faster than the reaction-diffusion processes. From this observation, it is possible to split the heat conduction dynamics from the others and propose the following splitting technique:

1. Given the concentration vector $\mathbf{C}^n$, compute Q_T and solve the thermal problem:

$$\rho c \frac{T^{n+1} - T^n}{\Delta t} - \kappa \nabla^2 T^{n+1} = Q_T; \tag{4.4.9}$$

2. Given temperature T^{n+1}, compute the kinetic constants $k_I(T^{n+1})$ and diffusivities $D_J(T^{n+1})$ and solve the reaction-diffusion problem:

$$\frac{\mathbf{C}^{n+1} - \mathbf{C}^n}{\Delta t} + \mathbf{div}(\mathbf{D}(\mathbf{C}^{n+1})\nabla \mathbf{C}^{n+1}) = \mathbf{F}(\mathbf{C}^{n+1}). \tag{4.4.10}$$

A sketch of the operations is provided in the Algorithm 3. The code

Input: kinetic and diffusion parameters:
$k_I^0, E_I, \Delta H_I, D_J^0, E_J^d, \kappa, \rho, c$;
Initialize: $\{C\}^1, T^1 \mathrm{tol}, \mathrm{norm} = 1$
Given $\{C\}^n, T^n$
for $n = 1, \ldots, N$ time steps **do**
  Compute $k_I(T^n),\ Q_T(T^n)$;
  Solve the thermal problem:
  $\rho c \partial_t T^{n+1} - \kappa \nabla^2 T^{n+1} = Q_T$;
  Update temperature: $T^{n+1} \leftarrow T^n$;
  Update kinetic constants and diffusivities:
  $k_I(T^{n+1}), D_J(T^{n+1})$;
  while $(\mathrm{norm} \geq \mathrm{tol})$ **do**
    Update reaction vector and diffusion matrix
    $\mathbf{F}_{(k)}^{n+1},\ \mathbf{D}_{(k)}^{n+1}$;
    Form the residual vector: $\{R\}_{(k)}^{n+1}$;
    Solve the linearized reaction-diffusion system:
    $\{C\}_{(k)}^{n+1} \leftarrow \{C\}_{(k)}^{n+1}$
  end
  Update the concentration vector:
  $\{C\}^{n+1} \leftarrow \{C\}^n$;
end

Algorithm 3: Splitting numerical scheme for the simulation of degradation in the accelerated aging tests.

is runned for 800 cycles and the concentration vector $\mathbf{C}$ is computed. We are interested in finding the minimum number of cycles to obtain a vector of degradation products which is comparable with the reference at 20 years $\mathbf{C}^{20\text{ years}}$ in ambiental conditions. We observe that:

$$\mathbf{C}^{\lessapprox 400\text{ cycle}} \approx \mathbf{C}^{20\text{ years}}, \tag{4.4.11}$$

so that for about less than 400 cycles the same amount of chemical products of the ambiental case at 20 years is reached. In the simulated aging conditions, the diffusion process of water is much faster than in the environmental conditions due to the extremal boundary condition which is subjected the H_2O (85% of relative humidity $\mathrm{RH}\%$). Comparing Fig-

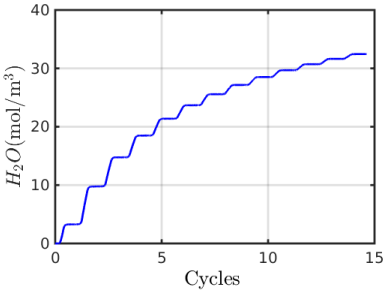

Figure 32: Evolution of the concentration of H_2O in the point P of the EVA layer for accelerated aging conditions in climatic chamber.

ure 32 with (30), we observe that just after 15 cycles we have that the water content in point P has reached the saturation level provided by $H_2O^{20\mathrm{years}}$.

Chapter 5

Advection-diffusion-reaction systems in Brinkman flows

5.1 Problem formulation

The coupled system of interest takes place in a bounded domain $\Omega \subset \mathbb{R}^d$, $d = 2, 3$ with Lipschitz boundary. It can be derived from basic principles of mass, momentum, and energy conservation, and it is written in terms of the fluid velocity $\boldsymbol{u} = (u_1, \dots, u_d)^T$, the rescaled vorticity $\boldsymbol{\omega}$ (vector $(\omega_1, \omega_2, \omega_3)^T$ if $d = 3$, or scalar ω if $d = 2$), the pressure p, and a vector $\boldsymbol{c} = (c_1, \dots, c_m)^T$ of volumetric fraction or total dissolved concentration of m distinct substances: For a.e. $(\boldsymbol{x}, t) \in \Omega_T := \Omega \times [0, T]$,

$$\begin{aligned} \partial_t \boldsymbol{c} + (\boldsymbol{u} \cdot \nabla)\boldsymbol{c} - \mathbf{div}(\boldsymbol{D}(\boldsymbol{c})\nabla \boldsymbol{c}) &= \boldsymbol{G}(\boldsymbol{c}), \\ \sigma \boldsymbol{u} + \sqrt{\mu}\, \mathbf{curl}\, \boldsymbol{\omega} + \nabla p &= \rho \boldsymbol{F}(\boldsymbol{c}), \\ \boldsymbol{\omega} &= \sqrt{\mu}\, \mathbf{curl}\, \boldsymbol{u}, \\ \operatorname{div} \boldsymbol{u} &= 0, \end{aligned} \tag{5.1.1}$$

where ρ, μ are the fluid density and viscosity, respectively $\sigma(\boldsymbol{x})$ is inverse permeability tensor, $\boldsymbol{F}$ represents the force exerted by the species on the fluid motion, encoding also external forces, $\boldsymbol{D}$ is a (generally nonlinear)

cross-diffusion matrix, and $\boldsymbol{G}$ contains the reaction kinetics (representing production and degradation) of the species.

Model (5.1.1) assumes that changes in the chemical concentrations do not influence thermophysical properties of the fluid such as viscosity or density, but rather they are nonlinearly coupled by the source term on the momentum equation. Conversely, we suppose that the viscous flow affects the species dynamics by means of advection only. The model also considers that the interaction of the species takes place in a porous medium composed of a bed of light fixed particles. Equations (5.1.1) are complemented with the following boundary and initial data:

$$(\boldsymbol{c}\boldsymbol{u}^T - \boldsymbol{D}(\boldsymbol{c})\nabla\boldsymbol{c})\boldsymbol{n} = \boldsymbol{0},\ \boldsymbol{u}\cdot\boldsymbol{n} = u_\partial,\ \boldsymbol{\omega}\times\boldsymbol{n} = \boldsymbol{\omega}_\partial\ (\boldsymbol{x},t) \in \partial\Omega\times[0,T],$$
$$\boldsymbol{c} = \boldsymbol{c}_0\ (\boldsymbol{x},t) \in \Omega\times\{0\},$$

representing that no flux occurs across the boundary (the species cannot leave the medium), and that a slip velocity together with a compatible vorticity trace are imposed along the domain boundary. These will be assumed homogeneous in the rest of the presentation.

We proceed to derive a weak formulation for (5.1.1). First, let us introduce the trial spaces where the weak solutions will live, and whose natural regularity is indicated by the formulation below: $\boldsymbol{c} \in L^2(0,T;\mathbf{S})$, $\partial_t\boldsymbol{c} \in L^2(0,T;\mathbf{S}')$, $\boldsymbol{u} \in L^2(0,T;\mathbf{V})$, $\boldsymbol{\omega} \in L^1(0,T;\mathbf{W})$, and $p \in L^2(0,T;Q)$; with $\mathbf{S} := \mathbf{H}^1(\Omega)$, $\mathbf{V} := \mathbf{H}(\mathrm{div};\Omega)$, $\mathbf{W} := \mathbf{H}(\mathbf{curl};\Omega)$ and $Q = L^2_0(\Omega) = \{q \in L^2(\Omega) : \int_\Omega q = 0\}$. The boundary conditions (5.1) suggest the following definition of the test spaces

$$\mathbf{S}_0 = \{\boldsymbol{s} \in \mathbf{S} : \boldsymbol{s} = \boldsymbol{0} \text{ on } \partial\Omega\},\quad \mathbf{V}_0 = \{\boldsymbol{v} \in \mathbf{V} : \boldsymbol{v}\cdot\boldsymbol{n} = 0 \text{ on } \partial\Omega\},$$
$$\mathbf{W}_0 = \{\boldsymbol{\theta} \in \mathbf{W} : \boldsymbol{\theta}\times\boldsymbol{n} = \boldsymbol{0} \text{ on } \partial\Omega\}.$$

The ADR equations are multiplied by $\boldsymbol{s} \in \mathbf{S}_0$ and integrated by parts over the spatial domain, the momentum equation for the flow is tested against $\boldsymbol{v} \in \mathbf{V}_0$ and integrated over Ω, the constitutive relation is tested against $\boldsymbol{\theta} \in \mathbf{W}_0$, and the mass conservation is multiplied by $q \in Q$. which leads to the problem: For $t \in (0,T]$, find $(\boldsymbol{c}(t),\boldsymbol{u}(t),\boldsymbol{\omega}(t),p(t)) \in \mathbf{S}\times\mathbf{V}\times$

$\mathbf{W} \times Q$ such that

$$\begin{aligned}
\int_\Omega [\partial_t \boldsymbol{c}(t) + (\boldsymbol{u}(t)\cdot\nabla)\boldsymbol{c}]\cdot\boldsymbol{s} + \int_\Omega \boldsymbol{D}(\boldsymbol{c}(t))\nabla\boldsymbol{c}(t) : \nabla\boldsymbol{s} &= \int_\Omega \boldsymbol{G}(\boldsymbol{c}(t))\cdot\boldsymbol{s},\\
\int_\Omega \sigma\boldsymbol{u}(t)\cdot\boldsymbol{v} + \sqrt{\mu}\int_\Omega \mathbf{curl}\,\boldsymbol{\omega}(t)\cdot\boldsymbol{v} - \int_\Omega p(t)\,\mathrm{div}\,\boldsymbol{v} &= \int_\Omega \rho\boldsymbol{F}(\boldsymbol{c}(t))\cdot\boldsymbol{v},\\
\sqrt{\mu}\int_\Omega \boldsymbol{u}(t)\cdot\mathbf{curl}\,\boldsymbol{\theta} - \int_\Omega \boldsymbol{\omega}(t)\cdot\boldsymbol{\theta} &= 0,\\
-\int_\Omega q\,\mathrm{div}\,\boldsymbol{u}(t) &= 0,
\end{aligned} \tag{5.1.2}$$

for all $\boldsymbol{s} \in \mathbf{S}_0, \boldsymbol{\theta} \in \mathbf{W}_0, \boldsymbol{v} \in \mathbf{V}_0, q \in Q$. Setting $\boldsymbol{\chi} = (\boldsymbol{c}, \boldsymbol{u}, \boldsymbol{\omega}, p)^T$, the matrix form of (5.1.2) can be recast as follows

$$\begin{pmatrix} \mathcal{A}_{\boldsymbol{c}} & \mathbf{0} & \mathbf{0} & \mathbf{0} \\ \mathbf{0} & \mathbf{0} & \mathbf{0} & \mathbf{0} \\ \mathbf{0} & \mathbf{0} & \mathbf{0} & \mathbf{0} \\ \mathbf{0} & \mathbf{0} & \mathbf{0} & \mathbf{0} \end{pmatrix} \dot{\boldsymbol{\chi}}(t) + \left(\begin{array}{c|ccc} \mathcal{D}-\mathcal{G} & \mathcal{C} & \mathbf{0} & \mathbf{0} \\ \hline -\mathcal{F} & \mathcal{A}_{\boldsymbol{u}} & \mathcal{B}_1 & -\mathcal{B}_2 \\ \mathbf{0} & \mathcal{B}_1^* & -\mathcal{A}_{\boldsymbol{\omega}} & \mathbf{0} \\ \mathbf{0} & -\mathcal{B}_2^* & \mathbf{0} & \mathbf{0} \end{array}\right) \boldsymbol{\chi}(t) = \mathbf{0}, \tag{5.1.3}$$

where dashed lines separate sub-blocks associated to the ADR and Brinkman systems, and the linear and nonlinear operators defining the matrix system are given by:

$$\begin{aligned}
[\mathcal{A}_{\boldsymbol{c}}(\boldsymbol{c}), \boldsymbol{s}] &:= \int_\Omega \boldsymbol{c}\cdot\boldsymbol{s}, \quad [\mathcal{D}(\boldsymbol{c}), \boldsymbol{s}] := \int_\Omega \boldsymbol{D}(\boldsymbol{c})\nabla\boldsymbol{c} : \nabla\boldsymbol{s},\\
[\mathcal{G}(\boldsymbol{c}), \boldsymbol{s}] &:= \int_\Omega \boldsymbol{G}(\boldsymbol{c})\cdot\boldsymbol{s}, \quad [\mathcal{C}(\boldsymbol{c}); \boldsymbol{u}, \boldsymbol{s}] := \int_\Omega (\boldsymbol{u}\cdot\nabla)\boldsymbol{c})\cdot\boldsymbol{s},\\
[\mathcal{A}_{\boldsymbol{u}}(\boldsymbol{u}), \boldsymbol{v}] &:= \int_\Omega \sigma\boldsymbol{u}\cdot\boldsymbol{v}, \quad [\mathcal{B}_1(\boldsymbol{\omega}), \boldsymbol{v}] := \int_\Omega \sqrt{\mu}\,\mathbf{curl}\,\boldsymbol{\omega}\cdot\boldsymbol{v},\\
[\mathcal{B}_2(p), \boldsymbol{v}] &:= \int_\Omega p\,\mathrm{div}\,\boldsymbol{v}, \quad [\mathcal{A}_{\boldsymbol{\omega}}(\boldsymbol{\omega}), \boldsymbol{\theta}] := \int_\Omega \boldsymbol{\omega}\cdot\boldsymbol{\theta}\\
[\mathcal{F}(\boldsymbol{c}), \boldsymbol{v}] &:= \int_\Omega \rho\boldsymbol{F}(\boldsymbol{c})\cdot\boldsymbol{v}.
\end{aligned}$$

Here the diffusion, reaction, and forcing terms are assumed smooth enough: $\boldsymbol{D}$ is positive, coercive, and continuous; $\boldsymbol{G}$ is continuous, uniformly bounded,

and positivity preserving; and $\boldsymbol{F}$ is linear in $\boldsymbol{c}$. More precise conditions on the coefficients will be specified later on. Classical derivations of a priori stability bounds will require an additional regularity for the velocity $\boldsymbol{u} \in L^2(0,T;\mathbf{V}) \cap L^\infty(0,T;L^\infty(\Omega)^d)$ (see e.g. (JD83; RE80) for flow-transport coupling in the context of miscible displacement in porous media).

Alternatively from (5.1.2), we can picture a formulation where an adequate manipulation of the Brinkman equations allows a decoupling between the velocity, vorticity, and pressure blocks, under the assumption of uniformly bounded permeability and homogeneous boundary conditions for velocity and vorticity (see (VARB16)). In that case, (5.1.3) is reformulated as:

$$\begin{pmatrix} \mathcal{A}_{\boldsymbol{c}} & \mathbf{0} & \mathbf{0} & \mathbf{0} \\ \mathbf{0} & \mathbf{0} & \mathbf{0} & \mathbf{0} \\ \mathbf{0} & \mathbf{0} & \mathbf{0} & \mathbf{0} \\ \mathbf{0} & \mathbf{0} & \mathbf{0} & \mathbf{0} \end{pmatrix} \dot{\boldsymbol{\chi}}(t) + \left(\begin{array}{c|c|cc} \mathcal{D}-\mathcal{G} & \mathcal{C} & \mathbf{0} & \mathbf{0} \\ \hline -\mathcal{F}_1 & \mathcal{A}_{\boldsymbol{u}} & \mathbf{0} & \mathbf{0} \\ \hline -\mathcal{F}_2 & \mathbf{0} & -\widehat{\mathcal{A}}_{\boldsymbol{\omega}} & \mathbf{0} \\ -\mathcal{F}_3 & \mathbf{0} & \mathbf{0} & \widehat{\mathcal{A}}_p \end{array}\right) \boldsymbol{\chi}(t) = \mathbf{0}, \tag{5.1.4}$$

where the modified blocks read:

$$\begin{aligned} [\widehat{\mathcal{A}}_{\boldsymbol{\omega}}(\boldsymbol{\omega}), \boldsymbol{\theta}] &:= \int_\Omega \sigma \boldsymbol{\omega} \cdot \boldsymbol{\theta} + \int_\Omega \mu\, \mathbf{curl}\, \boldsymbol{\omega} \cdot \mathbf{curl}\, \boldsymbol{\theta}, \\ [\mathcal{F}_2(\boldsymbol{c}), \boldsymbol{\theta}] &:= \int_\Omega \sqrt{\mu}\rho \boldsymbol{F}(\boldsymbol{c}) \cdot \mathbf{curl}\, \boldsymbol{\theta}, \\ [\widehat{\mathcal{A}}_p(p), q] &:= \int_\Omega \nabla p \cdot \nabla q, \quad [\mathcal{F}_3(\boldsymbol{c}), q] := \int_\Omega \rho \boldsymbol{F}(\boldsymbol{c}) \cdot \nabla q, \\ [\mathcal{F}_1(\boldsymbol{c}), \boldsymbol{v}] &:= \int_\Omega \left(\rho \boldsymbol{F}(\boldsymbol{c}) - \sqrt{\mu}\, \mathbf{curl}\, \tilde{\boldsymbol{\omega}} - \nabla \tilde{p}\right) \cdot \boldsymbol{v}, \end{aligned}$$

and where $\tilde{\cdot}$ denotes an uncoupled quantity. Another crucial difference with respect to (5.1.2), is that the pressure requires higher regularity (now $Q = H^1(\Omega) \cap L^2_0(\Omega)$), and that the velocity is only required in $L^2(0,T;\mathbf{L}^2(\Omega)) \cap L^\infty(0,T;L^\infty(\Omega)^d)$. Both Brinkman formulations lead to symmetric systems, which is a property that may be exploited by specialized preconditioners and iterative solvers.

5.1.1 A general operator splitting

5.1.2 Meshes and finite dimensional spaces

Let $\mathcal{T}_h$ denote a simplicial decomposition of the spatial domain Ω into elements K of maximum size h. For a fixed $h > 0$ we introduce finite dimensional subspaces for the $k-$th order approximation of the unknowns: $\mathbf{S}_h \subset \mathbf{S}$, $\mathbf{V}_h \subset \mathbf{V}$, $\mathbf{W}_h \subset \mathbf{W}$, and $Q_h \subset Q$. The concentration and vorticity finite element spaces assume the form

$$\mathbf{S}_h = \{\boldsymbol{s}_h \in \mathbf{S} : \boldsymbol{s}_h|_K \in [\mathbb{P}_{k+1}]^m(K),\ \forall K \in \mathcal{T}_h\},$$
$$\mathbf{W}_h = \{\boldsymbol{\theta}_h \in \mathbf{W} : \boldsymbol{\theta}_h|_K \in \mathbb{N}_{k+1}(K),\ \forall K \in \mathcal{T}_h\},$$

while, depending on whether the formulation (5.1.3) or (5.1.4) are used, the finite element spaces for the velocity and pressure unknowns are defined as:

$$\mathbf{V}_h = \{\boldsymbol{v}_h \in \mathbf{V} : \boldsymbol{v}_h|_K \in \mathbb{RT}_k(K),\ \forall K \in \mathcal{T}_h\},$$
$$Q_h = \{q_h \in L^2(\Omega) : q_h|_K \in \mathbb{P}_k(K),\ \forall K \in \mathcal{T}_h\},$$

or

$$\mathbf{V}_h = \{\boldsymbol{v}_h \in \mathbf{V} : \boldsymbol{v}_h|_K \in [\mathbb{P}_k(K)]^d,\ \forall K \in \mathcal{T}_h\},$$
$$Q_h = \{q_h \in H^1(\Omega) : q_h|_K \in \mathbb{P}_{k+1}(K),\ \forall K \in \mathcal{T}_h\},$$

respectively. Here $\mathbb{RT}_k$ stands for the local Raviart-Thomas elements of order k ($\mathbf{H}(\mathrm{div};\Omega)$-conforming), $\mathbb{N}_k$ is the local Nédélec element of degree k ($\mathbf{H}(\mathbf{curl};\Omega)$-conforming), and $\mathbb{P}_k$ is the local space of Lagrange finite elements of order k. Spaces $\mathbf{S}_h$ and $\mathbf{W}_h$ are equipped with the following norms as in (VARB16):

$$\|\boldsymbol{s}_h\|^2_{\mathbf{H}^1(\Omega)} := \|\boldsymbol{s}_h\|^2_{\mathbf{L}^2(\Omega)} + \|\nabla \boldsymbol{s}_h\|^2_{\mathbf{L}^2(\Omega)}, \quad \forall \boldsymbol{s}_h \in \mathbf{S}_h,$$
$$|||\boldsymbol{\theta}_h|||^2_{1,\mu} := \|\boldsymbol{\theta}_h\|^2_{\mathbf{L}^2(\Omega)} + \mu\|\mathbf{curl}\,\boldsymbol{\theta}_h\|^2_{\mathbf{L}^2(\Omega)}, \quad \forall \boldsymbol{\theta}_h \in \mathbf{W}_h.$$

Notice that the vorticity norm is $\mu-$dependent. The norms for the spaces $\mathbf{V}_h$ and Q_h defined by the first Brinkman formulation (5.1.3) are:

$$\|\boldsymbol{v}_h\|^2_{\mathbf{H}(\mathrm{div};\Omega)} := \|\boldsymbol{v}_h\|^2_{\mathbf{L}^2(\Omega)} + \|\,\mathrm{div}\,\boldsymbol{v}_h\|^2_{L^2(\Omega)}, \quad \forall \boldsymbol{v}_h \in \mathbf{V}_h,$$

and the natural $L^2(\Omega)-$norm for Q_h. On the other hand, for the second set of Brinkman equations (5.1.4) we consider the usual $\mathbf{L}^2(\Omega)-$ and $H^1(\Omega)-$norms for the spaces $\mathbf{V}_h$ and Q_h, respectively.

The Galerkin method associated to (5.1.3) or (5.1.4) is presented in what follows, using a partitioned solution approach.

5.1.3 Outer ADR-Brinkman splitting schemes

A straightforward splitting method consists in, starting from the initial concentrations distribution, solving the flow equations and then pass the computed velocity to advect the ADR system. For a backward Euler time advancing scheme, and depending on which of the two Brinkman solvers is considered (i.e., using (5.1.3) or (5.1.4)), the following steps are applied at each time step $t^n + 1$.
Solve the Flow problem in (5.1.3):
$(B1)$ Given $\boldsymbol{c}_h^n$, find $(\boldsymbol{u}_h^{n+1}, \boldsymbol{\omega}_h^{n+1}, p_h^{n+1}) \in \mathbf{V}_h \times \mathbf{W}_h \times Q_h$ such that $\forall \boldsymbol{v}_h \in \mathbf{V}_{h,0}, \boldsymbol{\theta}_h \in \mathbf{W}_{h,0}, q_h \in Q_{h,0}$:

$$\begin{aligned}\int_\Omega \sigma \boldsymbol{u}_h^{n+1} \cdot \boldsymbol{v}_h + \sqrt{\mu} \int_\Omega \mathbf{curl}\, \boldsymbol{\omega}_h^{n+1} \cdot \boldsymbol{v}_h - \int_\Omega p_h^{n+1} \operatorname{div} \boldsymbol{v}_h &= \int_\Omega \rho \boldsymbol{F}(\boldsymbol{c}_h^n) \cdot \boldsymbol{v}_h \\ \sqrt{\mu} \int_\Omega \boldsymbol{u}_h^{n+1} \cdot \mathbf{curl}\, \boldsymbol{\theta}_h - \int_\Omega \boldsymbol{\omega}_h^{n+1} \cdot \boldsymbol{\theta}_h &= 0 \\ - \int_\Omega q_h \operatorname{div} \boldsymbol{u}_h^{n+1} &= 0,\end{aligned} \tag{5.1.5}$$

or solve the Flow problem in (5.1.4):
$(B2)$ Given $\boldsymbol{c}_h^n$

- First solve the pure vorticity problem: Find $\boldsymbol{\omega}_h^{n+1} \in \mathbf{W}_h$ such that $\forall \boldsymbol{\theta}_h \in \mathbf{W}_{h,0}$

$$\int_\Omega \sigma \boldsymbol{\omega}_h^{n+1} \cdot \boldsymbol{\theta}_h + \mu \int_\Omega \mathbf{curl}\, \boldsymbol{\omega}_h^{n+1} \cdot \boldsymbol{\theta}_h = \sqrt{\mu} \int_\Omega \rho \boldsymbol{F}(\boldsymbol{c}_h^n) \cdot \mathbf{curl}\, \boldsymbol{\theta}_h, \tag{5.1.6}$$

- Then, solve the pure pressure problem:

$$\int_\Omega \nabla p_h^{n+1} \cdot \nabla q_h = \int_\Omega \rho \boldsymbol{F}(\boldsymbol{c}_h^n) \cdot \nabla q_h \quad \forall Q_h \tag{5.1.7}$$

- Finally recover the velocity vector $\boldsymbol{u}_h^{n+1} \in \mathbf{V}_h$ as:

$$\boldsymbol{u}_h^{n+1} = \sigma^{-1}\left(\rho \boldsymbol{F}(\boldsymbol{c}_h^n) - \sqrt{\mu}\,\mathbf{curl}\,\boldsymbol{\omega}_h^n - \nabla p_h^n\right) \tag{5.1.8}$$

(ADR) Then, given $\boldsymbol{u}_h^{n+1}$ solution of the Brinkman problem, Solve the Advection-Reaction-Diffusion problem: find $\boldsymbol{c}_h^{n+1} \in \mathbf{S}_h$ such that $\forall \boldsymbol{s}_h \in \mathbf{S}_{0,_h}$:

$$\begin{aligned}\int_\Omega \frac{\boldsymbol{c}_h^{n+1} - \boldsymbol{c}_h^n}{\Delta t} \cdot \boldsymbol{s}_h + \int_\Omega (\boldsymbol{u}_h^{n+1} \cdot \nabla)\boldsymbol{c}_h^{n+1} \cdot \boldsymbol{s}_h \\ + \int_\Omega \boldsymbol{D}(\boldsymbol{c}_h^{n+1})\nabla \boldsymbol{c}_h^{n+1} : \nabla \boldsymbol{s}_h = \int_\Omega \boldsymbol{G}(\boldsymbol{c}_h^{n+1}) \cdot \boldsymbol{s}_h.\end{aligned} \tag{5.1.9}$$

Under suitable hypotheses it can be proven that both problems (B1),(B2) and (ADR) admit unique solution respectively $(\boldsymbol{u}_h^{n+1}, \boldsymbol{\omega}_h^{n+1}, p_h^{n+1})$ and $\boldsymbol{c}_h^{n+1}$. The two solution strategies adopting either (B1) or (B2) lead to outer schemes for the Brinkman-ADR problem of the type (B1-ADR) or (B2-ADR). The inner solvers for the ADR equations will be made precise in the sequel. Notice that, whereas the flow problem (B1) or (B2) is linear, this is not the case for the ADR problem, so that at each time step a nested Newton-Raphson iterative scheme has to be employed to find an approximation of $\boldsymbol{c}_h^{n+1}$.

5.1.4 A priori estimates for the energy of the system

Let us recall the discrete Gronwall inequality

Lemma 5.1.1 *If $\phi_0 \leq g_0$ and*

$$\phi_n \leq g_0 + \sum_{k=0}^{n-1} p_k + \sum_{k=0}^{n-1} q_k \phi_k, \quad \forall n \geq 1,$$

then

$$\phi_n \leq \left(g_0 + \sum_{k=0}^{n-1} p_k\right) \exp\left(\sum_{k=0}^{n-1} q_k\right), \quad \forall n \geq 1.$$

The stability of the outer splitting method (B1)-(ADR) described in Section 5.1.3 is established by the following a priori bound, written in terms of the system's discrete energy norm:

$$\|\boldsymbol{\chi}_h^n\|^2 := \|\boldsymbol{u}_h^n\|^2_{\mathbf{H}(\mathrm{div};\Omega)} + |||\boldsymbol{\omega}_h^n|||^2_{1,\mu} + \|p_h^n\|^2_{L^2(\Omega)} + \|\boldsymbol{c}_h^n\|^2_{\mathbf{L}^2(\Omega)}, \quad \forall n \geq 0.$$

Before stating the main result, recall another lemma which will be useful later

Lemma 5.1.2 *Let $\boldsymbol{c}_h^n \in \mathbf{S}_h$ and assume that $\boldsymbol{F}(\boldsymbol{c})$ assumes the form $\boldsymbol{F}(\boldsymbol{c}) = (\boldsymbol{\alpha}\cdot\boldsymbol{c})\mathbf{g}$, for a constant vector $\boldsymbol{\alpha} \in \mathbb{R}^m$ and $\mathbf{g} = -\mathbf{e}_3$. The solution $(\boldsymbol{u}_h^n, \boldsymbol{\omega}_h^n, p_h^n) \in \mathbf{V}_h \times \mathbf{W}_h \times Q_h$ of the Brinkman probem* (5.1.5) *exists and is unique. Moreover there is a constant $C > 0$ independent of μ such that:*

$$\|p_h\|_{L^2(\Omega)} \leq C\|\rho\boldsymbol{F}(\boldsymbol{c}_h^n)\|_{\mathbf{L}^2(\Omega)} = C\rho\|\boldsymbol{\alpha}\|\|\boldsymbol{c}_h^n\|_{\mathbf{L}^2(\Omega)}. \tag{5.1.10}$$

The proof of this result can be found in (VARB16) and it is a consequence of the inf-sup condition: stating that exists a constant $\beta > 0$ such that:

$$\sup_{\substack{\boldsymbol{v}_h \in \mathbf{V}_h \\ \boldsymbol{v}_h \neq \mathbf{0}}} \frac{|[\mathcal{B}_2(q_h), \boldsymbol{v}_h]|}{\|\boldsymbol{v}_h\|_{\mathbf{H}(\mathrm{div};\Omega)}} \geq \beta\|q_h\|_{L^2(\Omega)}, \quad \forall q_h \in Q_h. \tag{5.1.11}$$

Theorem 5.1.3 *Let $\boldsymbol{\chi}_h^n = (\boldsymbol{c}_h^n, \boldsymbol{u}_h^n, \boldsymbol{\omega}_h^n, p_h^n)$, $\forall n = 0, \ldots, N_T$ be the solution of the outer splitting defined by* (5.1.5)-(5.1.9) *in (B1-ADR). Suppose that $\boldsymbol{F}(\boldsymbol{c}) = (\boldsymbol{\alpha}\cdot\boldsymbol{c})\mathbf{g}$, for constant $\boldsymbol{\alpha} \in \mathbb{R}^m$ and $\mathbf{g} = -\mathbf{e}_3$, and assume that there exists $D_{\min} > 0$ such that $\boldsymbol{s}^T(\boldsymbol{D}(\boldsymbol{s})\boldsymbol{s}) \geq D_{\min}\|\boldsymbol{s}\|^2$ for all $\boldsymbol{s}$. Then, there exist a constant $C(\sigma, \rho, \boldsymbol{\alpha}) > 0$ and positive non-decreasing functions $C_0(t^{n+1})$, $C_1(t^{n+1})$, such that, for each time step t^n:*

$$\|\boldsymbol{\chi}_h^{n+1}\|^2 + 2\Delta t D_{\min}^2 \sum_{k=0}^{n} \|\nabla\boldsymbol{c}_h^{k+1}\|^2_{\mathbf{L}^2(\Omega)} \leq C_0(t^{n+1})\|\boldsymbol{c}_h^0\|^2_{\mathbf{L}^2(\Omega)} +$$

$$C_1(t^{n+1}) \sum_{k=0}^{n} \|\boldsymbol{G}(\boldsymbol{c}_h^{k+1})\|^2_{\mathbf{L}^2(\Omega)} + C(\sigma, \rho, \boldsymbol{\alpha})\|\boldsymbol{c}_h^n\|^2_{\mathbf{L}^2(\Omega)}.$$

In particular, if $\|\boldsymbol{G}(\boldsymbol{c})\|_{\mathbf{L}^2(\Omega)} \leq G$ for a given $G \geq 0$, then, at each timestep the

energy norm admits the following bound

$$\|\boldsymbol{\chi}_h^n\|^2 \leq \|\boldsymbol{\chi}_h^0\|^2 \sum_{k=0}^{N_T} C^k(\sigma,\rho,\boldsymbol{\alpha}) C_0(t^{N_T-k}) + C^{N_T}(\sigma,\rho,\boldsymbol{\alpha})\|\boldsymbol{\chi}_h^0\|^2 + G^2 \sum_{k=0}^{N_T} C^k(\sigma,\rho,\boldsymbol{\alpha})(N_T-k) C_1(t^{N_T-k})$$

Proof. Using integration by parts we observe that the convective term in (5.1.9) can be rewritten in the skew-symmetric form:

$$\int_\Omega (\boldsymbol{u}_h^{n+1}\cdot\nabla)\boldsymbol{c}_h^{n+1}\cdot\boldsymbol{s}_h = \frac{1}{2}\int_\Omega (\boldsymbol{u}_h^{n+1}\cdot\nabla)\boldsymbol{c}_h^{n+1}\cdot\boldsymbol{s}_h - \frac{1}{2}\int_\Omega (\boldsymbol{u}_h^{n+1}\cdot\nabla)\boldsymbol{s}_h\cdot\boldsymbol{c}_h^{n+1}.$$

Next, testing equation (5.1.9) with $\boldsymbol{s}_h = \boldsymbol{c}_h^{n+1} \in \mathbf{S}_h$ and using Young's inequality we have:

$$\frac{1}{2}\|\boldsymbol{c}_h^{n+1}\|^2_{\mathbf{L}^2(\Omega)} + \Delta t D_{\min}\|\nabla\boldsymbol{c}_h^{n+1}\|^2_{\mathbf{L}^2(\Omega)} \leq \frac{1}{2}\|\boldsymbol{c}_h^{n}\|^2_{\mathbf{L}^2(\Omega)} + \frac{\Delta t}{2}\|\boldsymbol{G}(\boldsymbol{c}_h^{n+1})\|^2_{\mathbf{L}^2(\Omega)} + \frac{\Delta t}{2}\|\boldsymbol{c}_h^{n+1}\|^2_{\mathbf{L}^2(\Omega)},$$

and summing up for $k = 0,\ldots,n-1$ implies that

$$\frac{1}{2}\|\boldsymbol{c}_h^{n}\|^2_{\mathbf{L}^2(\Omega)} + \Delta t D_{\min}\sum_{k=0}^{n-1}\|\nabla\boldsymbol{c}_h^{k+1}\|^2_{\mathbf{L}^2(\Omega)} \leq \frac{1}{2}\|\boldsymbol{c}_h^{0}\|^2_{\mathbf{L}^2(\Omega)} + \frac{\Delta t}{2}\sum_{k=0}^{n-1}\|\boldsymbol{G}(\boldsymbol{c}_h^{k+1})\|^2_{\mathbf{L}^2(\Omega)} + \frac{\Delta t}{2}\sum_{k=0}^{n-1}\|\boldsymbol{c}_h^{k+1}\|^2_{\mathbf{L}^2(\Omega)}. \tag{5.1.12}$$

Applying Lemma 5.1.1 we can then write:

$$\|\boldsymbol{c}_h^{n}\|^2_{\mathbf{L}^2(\Omega)} \leq \exp(t^n)\left\{\|\boldsymbol{c}_h^{0}\|^2_{\mathbf{L}^2(\Omega)} + \Delta t\sum_{k=0}^{n-1}\|\boldsymbol{G}(\boldsymbol{c}_h^{k+1})\|^2_{\mathbf{L}^2(\Omega)}\right\}, \quad \forall n \geq 1.$$

Using this for $n+1$, and substituting back in the last term of (5.1.12), after collecting terms we obtain that there are two functions $C_0(t^{n+1}), C_1(t^{n+1}) >$

0 such that the following estimate holds:

$$\|\boldsymbol{c}_h^{n+1}\|^2_{\mathbf{L}^2(\Omega)} + 2\Delta t D_{\min}\sum_{k=0}^{n}\|\nabla \boldsymbol{c}_h^{k+1}\|^2_{\mathbf{L}^2(\Omega)} \leq C_0(t^{n+1})\|\boldsymbol{c}_h^0\|^2_{\mathbf{L}^2(\Omega)} + C_1(t^{n+1})\sum_{k=0}^{n}\|\boldsymbol{G}(\boldsymbol{c}_h^{k+1})\|^2_{\mathbf{L}^2(\Omega)}. \tag{5.1.13}$$

On the other hand, regarding the Brinkman problem, we proceed to test (5.1.5) against

$$\boldsymbol{v}_h = \boldsymbol{u}_h^{n+1} + c_1\sqrt{\mu}\,\mathbf{curl}\,\boldsymbol{\omega}_h^{n+1} \in \mathbf{V}_{0,h}, \quad \boldsymbol{\theta}_h = -\boldsymbol{\omega}_h^{n+1} \in \mathbf{W}_{0,h},$$
$$q_h = -p_h^{n+1} - c_2\,\mathrm{div}\,\boldsymbol{u}_h^{n+1} \in Q_h,$$

where c_1 and c_2 are positive constants to be determined. Summing up in (5.1.5) we have:

$$\sigma\|\boldsymbol{u}_h^{n+1}\|^2_{\mathbf{L}^2(\Omega)} + \int_\Omega \sigma c_1\sqrt{\mu}\boldsymbol{u}_h^{n+1}\cdot\mathbf{curl}\,\boldsymbol{\omega}_h^{n+1} + \int_\Omega \sqrt{\mu}\,\mathbf{curl}\,\boldsymbol{\omega}_h^{n+1}\cdot\boldsymbol{u}_h^{n+1} +$$
$$c_1\mu\|\mathbf{curl}\,\boldsymbol{\omega}_h^{n+1}\|^2_{\mathbf{L}^2(\Omega)} - \int_\Omega p_h^{n+1}\,\mathrm{div}\,\boldsymbol{u}_h^{n+1} - \int_\Omega p_h^{n+1}c_1\sqrt{\mu}\,\mathrm{div}\,\mathbf{curl}\,\boldsymbol{\omega}_h^{n+1} -$$
$$\int_\Omega \sqrt{\mu}\boldsymbol{u}_h^{n+1}\cdot\mathbf{curl}\,\boldsymbol{\omega}_h^{n+1} + \|\boldsymbol{\omega}_h^{n+1}\|^2_{\mathbf{L}^2(\Omega)} + \int_\Omega p_h^{n+1}\,\mathrm{div}\,\boldsymbol{u}_h^{n+1} +$$
$$c_2\|\,\mathrm{div}\,\boldsymbol{u}_h^{n+1}\|^2_{\mathbf{L}^2(\Omega)} = \int_\Omega \rho\boldsymbol{F}(\boldsymbol{c}_h^n)\cdot\boldsymbol{u}_h^{n+1} + \int_\Omega c_1\sqrt{\mu}\rho\boldsymbol{F}(\boldsymbol{c}_h^n)\cdot\mathbf{curl}\,\boldsymbol{\omega}_h^{n+1},$$

and then applying Young's inequality gives:

$$c_1\sqrt{\mu}\int_\Omega \sigma\boldsymbol{u}_h^{n+1}\cdot\mathbf{curl}\,\boldsymbol{\omega}_h^{n+1} \geq -\frac{\sigma_{\min}}{2}\|\boldsymbol{u}_h^{n+1}\|^2_{\mathbf{L}^2(\Omega)} - \frac{c_1^2\sigma_{\max}^2}{2\sigma_{\min}}\mu\|\,\mathbf{curl}\,\boldsymbol{\omega}_h^{n+1}\|^2_{\mathbf{L}^2(\Omega)},$$

and

$$\int_\Omega \rho\boldsymbol{F}(\boldsymbol{c}_h^{n+1})\cdot\boldsymbol{u}_h^{n+1} \leq \frac{\sigma_{\min}}{4}\|\boldsymbol{u}_h^{n+1}\|^2_{\mathbf{L}^2(\Omega)} + \frac{\rho^2}{\sigma_{\min}}\|\boldsymbol{\alpha}\|^2\|\boldsymbol{c}_h^n\|^2_{\mathbf{L}^2(\Omega)},$$
$$\int_\Omega c_1\sqrt{\mu}\rho\boldsymbol{F}(\boldsymbol{c}_h^n)\cdot\mathbf{curl}\,\boldsymbol{\omega}_h^{n+1} \leq \frac{c_1^2\mu}{2}\|\,\mathbf{curl}\,\boldsymbol{\omega}_h^{n+1}\|^2_{\mathbf{L}^2(\Omega)} + \frac{\rho^2}{2}\|\boldsymbol{\alpha}\|^2\|\boldsymbol{c}_h^n\|^2_{\mathbf{L}^2(\Omega)}.$$

Because $\operatorname{div}\mathbf{curl}$ is the zero operator, we have that $\boldsymbol{F}(\boldsymbol{c}_h^n) = (\boldsymbol{\alpha}\cdot\boldsymbol{c}_h^n)\mathbf{g}$, and collecting terms we obtain:

$$c_1\left\{1-\frac{c_1}{2}\left(\frac{\sigma_{\max}^2}{\sigma_{\min}}+1\right)\right\}\mu\|\mathbf{curl}\,\boldsymbol{\omega}_h^{n+1}\|^2_{\mathbf{L}^2(\Omega)}+\|\boldsymbol{\omega}_h^{n+1}\|^2_{\mathbf{L}^2(\Omega)}+$$
$$\frac{\sigma_{\min}}{4}\|\boldsymbol{u}_h^{n+1}\|^2_{\mathbf{L}^2(\Omega)}+c_2\|\operatorname{div}\boldsymbol{u}_h^{n+1}\|^2_{\mathbf{L}^2(\Omega)}\leq\rho^2\|\boldsymbol{\alpha}\|^2\left(\frac{1}{\sigma_{\min}}+\frac{1}{2}\right)\|\boldsymbol{c}_h^n\|^2_{\mathbf{L}^2(\Omega)}.$$

Notice that the term involving the norm of pressure has disappeared. Taking $c_1=\frac{\sigma_{\min}}{(\sigma_{\max}^2+\sigma_{\min})}, c_2=\frac{\sigma_{\min}}{4}$ we obtain that there exists a constant $\widetilde{C}(\sigma,\rho,\boldsymbol{\alpha})>0$ such that:

$$\|\boldsymbol{u}_h^{n+1}\|^2_{\mathbf{L}^2(\Omega)}+\|\operatorname{div}\boldsymbol{u}_h^{n+1}\|^2_{L^2(\Omega)}+\|\boldsymbol{\omega}_h^{n+1}\|^2_{\mathbf{L}^2(\Omega)}$$
$$+\mu\|\mathbf{curl}\,\boldsymbol{\omega}_h^{n+1}\|^2_{\mathbf{L}^2(\Omega)}\leq\widetilde{C}(\sigma,\rho,\boldsymbol{\alpha})\|\boldsymbol{c}_h^n\|^2_{\mathbf{L}^2(\Omega)}.$$

The next step consists in recovering an estimate for the norm of the solution of the Brinkman problem involving the pressure norm. This is done via Lemma 5.1.2, from which we obtain that there is a constant $C(\sigma,\rho,\boldsymbol{\alpha})>0$ such that:

$$\|\boldsymbol{u}_h^n\|^2_{\mathbf{H}(\operatorname{div};\Omega)}+|||\boldsymbol{\omega}_h^n|||^2_{1,\mu}+\|p_h^n\|^2_{L^2(\Omega)}\leq C(\sigma,\rho,\boldsymbol{\alpha})\|\boldsymbol{c}_h^n\|^2_{\mathbf{L}^2(\Omega)}. \quad (5.1.14)$$

Combining estimates (5.1.13) and (5.1.14) we have the desired result. □

5.2 Dedicated partitioned schemes for the ADR equations

We now address the numerical solution of the nonlinear ADR problem (5.1.9). Based on the structure of the nonlinear diffusion matrix $\boldsymbol{D}(\boldsymbol{c})$ and of the reaction vector $\boldsymbol{G}(\boldsymbol{c})=(G_1(\boldsymbol{c}),\ldots,G_m(\boldsymbol{c}))$, diverse techniques can be employed. Let $\{\boldsymbol{\varphi}_i : i=1,\ldots,N_{\mathbf{S}_h}\}$ be the vector-valued basis of shape functions of the finite element space for the concentration $\mathbf{S}_h$, where $N_{\mathbf{S}_h}=\dim(\mathbf{S}_h)$. Then we denote the finite element approximation of the concentration vector as:

$$\boldsymbol{c}_h(\boldsymbol{x},t^n)=\sum_{i=1}^{N_{\mathbf{S}_h}}\mathbf{C}_i(t^n)\boldsymbol{\varphi}_i(\boldsymbol{x})=\sum_{i=1}^{M_{\mathbf{S}_h}}\sum_{j=1}^{m}C_i^j(t^n)\boldsymbol{\varphi}_i^j(\boldsymbol{x}), \quad (5.2.1)$$

where $M_{\mathbf{S}_h} = \dfrac{N_{\mathbf{S}_h}}{m}$ and C_i^j represents the j-th component of $\boldsymbol{c}_h$ at the mesh node i and we regrouped the basis vectors as $\boldsymbol{\varphi}_i^1 = (\varphi_i, \cdots, 0)^T$, ..., $\boldsymbol{\varphi}_i^m = (0, \cdots, \varphi_i)^T$.
The algebraic form of (5.1.9) is derived by substituting in the weak formulation the expression (5.2.1) and the analogous form for the test function. First we will focus on a monolithic solver for the ADR system based on a Newton method with full Jacobian.

5.2.1 A fully implicit Newton-Raphson method

From (5.1.9) the following nonlinear algebraic system must be solved at each time-step t^{n+1}:

$$\left(\frac{A_{\boldsymbol{c}}}{\Delta t} + C(\boldsymbol{u}_h^{n+1}) + D(\mathbf{C}^{n+1})\right)\mathbf{C}^{n+1} = \widetilde{\boldsymbol{G}}(\mathbf{C}^{n+1}) + \frac{1}{\Delta t}\mathbf{C}^n \tag{5.2.2}$$

where the global nodal concentration vector in $\mathbb{R}^{N_{\mathbf{S}_h}}$ and the reaction vector are:

$$(\mathbf{C}^n)_i = \mathbf{C}_i^n, \quad (\widetilde{\boldsymbol{G}}(\mathbf{C}))_i = \int_\Omega \boldsymbol{G}\left(\sum_{k=1}^{N_{\mathbf{S}_h}} \mathbf{C}_k \boldsymbol{\varphi}_k\right)\boldsymbol{\varphi}_i \quad i = 1, \ldots, N_{\mathbf{S}_h}, \tag{5.2.3}$$

and matrices $A_{\boldsymbol{c}}$, C, D in $\mathbb{R}^{N_{\mathbf{S}_h}} \times \mathbb{R}^{N_{\mathbf{S}_h}}$ are given by:

$$\begin{aligned}
(A_{\boldsymbol{c}})_{ij} &= \int_\Omega \boldsymbol{\varphi}_j \cdot \boldsymbol{\varphi}_i, \quad (C)_{ij} = \int_\Omega \left(\boldsymbol{u}_h^{n+1} \cdot \nabla\right)\boldsymbol{\varphi}_j \cdot \boldsymbol{\varphi}_i, \\
(D(\mathbf{C}))_{ij} &= \int_\Omega \boldsymbol{D}\left(\sum_{k=1}^{N_{\mathbf{S}_h}} \mathbf{C}_k \boldsymbol{\varphi}_k\right)\nabla\boldsymbol{\varphi}_j : \nabla\boldsymbol{\varphi}_i.
\end{aligned} \tag{5.2.4}$$

Notice that the convection matrix C depends on the velocity vector $\boldsymbol{u}_h^{n+1}$, solution of the Brinkman problem computed at the previous stage of the splitting scheme so that it is constant with respect to the unknown concentration vector $\boldsymbol{c}_h^{n+1}$. The nonlinearity of system (5.2.2) resides in the diffusion matrix D and in the reaction vector $\widetilde{\boldsymbol{G}}$ which are functions of the unknown vector $\boldsymbol{c}_h^{n+1}$. We introduce the monolithic ADR residual

vector:

$$\mathbf{R}^n(\mathbf{C}) := \left(\frac{A_{\boldsymbol{c}}}{\Delta t} + C(\boldsymbol{u}_h^{n+1}) + D(\mathbf{C})\right)\mathbf{C} - \widetilde{\boldsymbol{G}}(\mathbf{C}) - \frac{A_{\boldsymbol{c}}}{\Delta t}\mathbf{C}^n,$$

and realize that solving (5.2.2) is equivalent to solve $\mathbf{R}^n(\mathbf{C}^{n+1}) = \mathbf{0}$. With this purpose, we employ the Newton-Raphson iterative procedure: Suppose that at time t^n and k-th iteration of the Newton-Raphson method, we are given an approximation $\mathbf{C}^{n+1,k}$ of the concentration vector $\mathbf{C}^{n+1}$, then we solve the following linear system in the correction $\delta\mathbf{C}$ and update as:

$$\left(\frac{A_{\boldsymbol{c}}}{\Delta t} + C(\boldsymbol{u}_h^{n+1}) + \widetilde{D}(\mathbf{C}^{n+1,k}) - \frac{\partial\widetilde{\boldsymbol{G}}}{\partial\mathbf{C}}(\mathbf{C}^{n+1,k})\right)\delta\mathbf{C} = -\mathbf{R}^n(\mathbf{C}^{n+1,k}),$$
$$\mathbf{C}^{n+1,k+1} = \mathbf{C}^{n+1,k} + \delta\mathbf{C},$$

where the matrices $\widetilde{D}$ and $\partial\widetilde{\boldsymbol{G}}/\partial\mathbf{C}$ arise form the linearization of the diffusion matrix and the reaction vector, respectively, and are given by:

$$\begin{aligned}(\widetilde{D}(\mathbf{C}))_{ij} &= D_{ij}(\mathbf{C}) + \sum_{k=1}^{N_{\mathbf{S}_n}}\left(\int_\Omega \frac{\partial}{\partial\boldsymbol{c}}\boldsymbol{D}(\mathbf{C})\boldsymbol{\varphi}_j\nabla\boldsymbol{\varphi}_k : \nabla\boldsymbol{\varphi}_i\right)\mathbf{C}_k,\\ (\frac{\partial\widetilde{\boldsymbol{G}}}{\partial\mathbf{C}}(\mathbf{C}))_{ij} &= \int_\Omega \boldsymbol{\varphi}_j^T\nabla\boldsymbol{G}(\mathbf{C})\boldsymbol{\varphi}_i\end{aligned} \tag{5.2.5}$$

and the matrix $\dfrac{\partial}{\partial\boldsymbol{c}}\boldsymbol{D}(\mathbf{C})\boldsymbol{\varphi}_j$ is a shorthand notation for $\displaystyle\sum_{s=1}^{m}\frac{\partial\boldsymbol{D}}{\partial c_s}(\mathbf{C})\boldsymbol{\varphi}_j^s$. The Newton-Raphson system (**??**) for the full monolithic ADR can be reformulated as a variational problem for the finite element correction vector $\delta\boldsymbol{c}_h$, leading to the following solver for the ADR system:

(ADR1): Given a velocity $\boldsymbol{u}_h^{n+1}$, a solution $\boldsymbol{c}_h^n$ of the ADR at time t^n, and the approximate solution $\boldsymbol{c}_h^{n+1,k}$ at the k-th iteration of the Newton-Raphson method for the full monolithic ADR system, find $\delta\boldsymbol{c}_h \in \mathbf{S}_{h,0}$ such that:

$$\left(\frac{1}{\Delta t}\mathcal{A}_{\boldsymbol{c}} + \mathcal{C}(\boldsymbol{u}_h^{n+1}) + d\mathcal{D}_{\boldsymbol{c}_h^{n+1,k}} - d\mathcal{G}_{\boldsymbol{c}_h^{n+1,k}}\right)\delta\boldsymbol{c}_h = -\mathcal{R}^n(\boldsymbol{c}_h^{n+1,k}), \tag{5.2.6}$$

and update $\boldsymbol{c}_h^{n+1,k+1} = \boldsymbol{c}_h^{n+1,k} + \delta\boldsymbol{c}_h$, until $\|\delta\boldsymbol{c}_h\|_{\mathbf{L}^2(\Omega)} \leq$ tol.

The linear and bilinear operators in the variational problem (5.2.6) are given by:

$$
\begin{aligned}
[\mathcal{R}^n(\boldsymbol{c}), \boldsymbol{s}] &:= \frac{1}{\Delta t}[\mathcal{A}_{\boldsymbol{c}}(\boldsymbol{c} - \boldsymbol{c}^n), \boldsymbol{s}] + [\mathcal{C}(\boldsymbol{c}); \boldsymbol{u}_h^{n+1}, \boldsymbol{s}] + [\mathcal{D}(\boldsymbol{c}), \boldsymbol{s}] - [\mathcal{G}(\boldsymbol{c}), \boldsymbol{s}], \\
[d\mathcal{D}_{\boldsymbol{c}}(\delta\boldsymbol{c}), \boldsymbol{s}] &:= \int_\Omega \boldsymbol{D}(\boldsymbol{c})\nabla\delta\boldsymbol{c} : \nabla\boldsymbol{s} + \int_\Omega \frac{\partial}{\partial \boldsymbol{c}}\boldsymbol{D}(\boldsymbol{c})\delta\boldsymbol{c}\, \nabla\boldsymbol{c} : \nabla\boldsymbol{s}, \\
[d\mathcal{G}_{\boldsymbol{c}}(\delta\boldsymbol{c}), \boldsymbol{s}] &:= \int_\Omega \boldsymbol{s}^T \nabla\boldsymbol{G}(\boldsymbol{c})\delta\boldsymbol{c}.
\end{aligned}
\tag{5.2.7}
$$

We stress that in problem (5.2.6) we require that the unknown $\delta\boldsymbol{c}_h = \boldsymbol{c}_h^{n+1,k+1} - \boldsymbol{c}_h^{n+1,k}$ is in $\mathbf{S}_{h,0}$, because it must be zero at the boundaries where the Dirichlet conditions apply. To obtain an adequate initial guess $\boldsymbol{c}_h^{n+1,0}$ we can solve, at the beginning of the Newton-Raphson scheme, a simplified linear problem, typically with $\boldsymbol{D}(\boldsymbol{c}_h^n)$ and $\boldsymbol{G}(\boldsymbol{c}_h^n)$.

The (ADR1) solver for the full ADR system using Newton-Raphson method is combined with a flow solver (B1) or (B2), leading to a global solution scheme for the problem, denoted as (B1/B2-ADR1). The steps of the solution strategy of our problem using the (B1/B2-ADR1) are summarized in Algorithm 4.

Data: σ, μ, ρ, $\boldsymbol{\alpha}$, $\boldsymbol{D}$, $\boldsymbol{G}$, Δt, N, tol ;
Initialize: $\boldsymbol{u}_h^0$, $\boldsymbol{\omega}_h^0$, p_h^0, $\boldsymbol{c}_h^0$;
for $n = 1, \dots, N$ time steps **do**
  Given $\boldsymbol{c}_h^n$, **solve** the Brinkman system (B1):

$$\begin{pmatrix} \mathcal{A}_{\boldsymbol{u}} & \mathcal{B}_1 & \mathcal{B}_2 \\ \mathcal{B}_1^* & -\mathcal{A}_{\omega} & \mathbf{0} \\ -\mathcal{B}_2^* & \mathbf{0} & \mathbf{0} \end{pmatrix} \begin{pmatrix} \boldsymbol{u}_h^{n+1} \\ \boldsymbol{\omega}_h^{n+1} \\ p_h^{n+1} \end{pmatrix} = \begin{pmatrix} \mathcal{F}_1(\boldsymbol{c}_h^n) \\ \mathbf{0} \\ \mathbf{0} \end{pmatrix};$$

  or its split counterpart (B2):

  - $\widehat{\mathcal{A}}_{\boldsymbol{\omega}} \boldsymbol{\omega}_h^{n+1} = \mathcal{F}_2(\boldsymbol{c}_h^n)$,
  - $\widehat{\mathcal{A}}_p p_h^{n+1} = \mathcal{F}_3(\boldsymbol{c}_h^n)$,
  - $\boldsymbol{u}_h^{n+1} \leftarrow \mathcal{A}_{\boldsymbol{u}}^{-1} \mathcal{F}_1(\boldsymbol{c}_h^n)$;

  Update: $\boldsymbol{u}_h^{n+1} \leftarrow \boldsymbol{u}_h^n$; $\boldsymbol{\omega}_h^{n+1} \leftarrow \boldsymbol{\omega}_h^n$; $p_h^{n+1} \leftarrow p_h^n$;
  Given $\boldsymbol{u}_h^{n+1}$, **solve** the full ADR system via Newton-Raphson (ADR1):
  Initialize: $\boldsymbol{c}_h^{n+1,0}$;
  while $\|\delta \boldsymbol{c}\|_{\mathbf{L}^2(\Omega)} \geq$ tol **do**
    Solve the linearized ADR equations monolithically:

$$\left(\frac{1}{\Delta t} \mathcal{A}_{\boldsymbol{c}} + \mathcal{C}(\boldsymbol{u}_h^{n+1}) + d\mathcal{D}_{\boldsymbol{c}_h^{n+1,k}} - d\mathcal{G}_{\boldsymbol{c}_h^{n+1,k}} \right) \delta \boldsymbol{c}_h = -\mathcal{R}^n(\boldsymbol{c}_h^{n+1,k}),$$

    Update: $\boldsymbol{c}_h^{n+1,k+1} \leftarrow \boldsymbol{c}_h^{n+1,k} + \delta \boldsymbol{c}_h$;
  end
  Update: $\boldsymbol{c}_h^{n+1} \leftarrow \boldsymbol{c}_h^n$;
end

Algorithm 4: Staggered procedure (B1/B2-ADR1) for the Brinkman problem solved with either (B1) or (B2) and the full ADR problem solved with (ADR1).

5.2.2 Inner splitting of the ADR system

When the diffusion matrix $\boldsymbol{D}$ is constant and the reaction term $\boldsymbol{G}(\boldsymbol{c})$ leads to highly stiff systems, it is convenient to split the ADR dynamics into a pure advection-diffusion phase and into a pure reaction phase. This implies we solve problem (5.1.9) separating the nonlinear term due to reaction $\boldsymbol{G}(\boldsymbol{c})$, which defines a nonlinear system of ODEs, from the (typically more regular and smooth) advection-diffusion process. This method is denoted (ADR2) and consists in solving the ADR system in two steps

(ADR2): – Pure advection-diffusion phase: Given $\boldsymbol{u}_h^{n+1}$ and $\boldsymbol{c}_h^n$, find $\boldsymbol{c}_h^{n+1,*}$ in $\mathbf{S}_h$ solution of the linear problem:

$$\int_\Omega \frac{\boldsymbol{c}_h^{n+1,*} - \boldsymbol{c}_h^n}{\Delta t} \cdot \boldsymbol{s}_h + \int_\Omega (\boldsymbol{u}_h^{n+1} \cdot \nabla)\boldsymbol{c}_h^{n+1,*} \cdot \boldsymbol{s}_h + \int_\Omega \boldsymbol{D}\nabla \boldsymbol{c}^{n+1,*} : \nabla \boldsymbol{s}_h = 0 \qquad \forall \boldsymbol{s}_h \in \mathbf{S}_{0,h}. \tag{5.2.8}$$

– Pure reaction phase: Setting $\boldsymbol{c}_h^n = \boldsymbol{c}_h^{n+1,*}$, solve the nonlinear problem:

$$\int_\Omega \frac{\boldsymbol{c}_h^{n+1} - \boldsymbol{c}_h^n}{\Delta t} \cdot \boldsymbol{s}_h = \int_\Omega \boldsymbol{G}(\boldsymbol{c}_h^{n+1}) \cdot \boldsymbol{s}_h \qquad \forall \boldsymbol{s}_h \in \mathbf{S}_{0,h}. \tag{5.2.9}$$

Problems (5.2.8) and (5.2.9) are discretized using the same notations (5.2.4) and (5.2.3) for matrices and vectors as in the previous section. The nonlinear algebraic system equivalent to the pure reaction phase (5.2.9), that must be solved at each time iteration t^{n+1} is given by:

$$\frac{A_{\boldsymbol{c}}}{\Delta t}\mathbf{C}^{n+1} = \frac{A_{\boldsymbol{c}}}{\Delta t}\mathbf{C}^n + \widetilde{\mathbf{G}}(\mathbf{C}^{n+1}), \tag{5.2.10}$$

where matrices and vectors $A_{\boldsymbol{c}}$, $\mathbf{C}^n$ and $\widetilde{\mathbf{G}}$ are defined in (5.2.4), (5.2.3). System (5.2.10) can be solved iteratively using the Newton-Raphson method. With this aim we define the residual $\mathbf{R}^{*,n}$ of the pure reaction phase as

$$\mathbf{R}^{*,n} := \frac{A_{\boldsymbol{c}}}{\Delta t}\mathbf{C}^{n+1} - \frac{A_{\boldsymbol{c}}}{\Delta t}\mathbf{C}^n - \widetilde{\mathbf{G}}(\mathbf{C}^{n+1}),$$

and again we notice that solving (5.2.10) is equivalent to solve $\mathbf{R}^{*,n}(\mathbf{C}^{n+1}) = \mathbf{0}$. Given an approximate solution of the system (5.2.10) $\mathbf{C}^{n+1,k}$ at iteration k, one solves the Newton-Raphson system for the pure reaction problem:

$$\left(\frac{A_{\boldsymbol{c}}}{\Delta t} - \frac{\partial \widetilde{\boldsymbol{G}}}{\partial \mathbf{C}}(\mathbf{C}^{n+1,k})\right)\delta\mathbf{C} = -\mathbf{R}^{*,n}(\mathbf{C}^{n+1,k}), \qquad \mathbf{C}^{n+1,k+1} = \mathbf{C}^{n+1,k} + \delta\mathbf{C}. \tag{5.2.11}$$

System (5.2.11) can be rewritten as a variational problem for the finite element correction $\delta \boldsymbol{c}_h$. Given $\boldsymbol{c}_h^n$ and the approximate solution $\boldsymbol{c}_h^{n+1,k}$ at $k-$th iteration, the problem is to find $\delta \boldsymbol{c}_h \in \mathbf{S}_{0,h}$ such that:

$$\left(\frac{\mathcal{A}_{\boldsymbol{c}}}{\Delta t} - d\mathcal{G}_{\boldsymbol{c}_h^{n+1,k}} \right) \delta \boldsymbol{c}_h = -\mathcal{R}^{*,n}(\boldsymbol{c}_h^{n+1,k}).$$

The operator $d\mathcal{G}_{\boldsymbol{c}}$ is given in (5.2.7), while the linear operator corresponding to the pure-reaction residual vector is:

$$[\mathcal{R}^{n,*}(\boldsymbol{c}), \boldsymbol{s}] := \frac{1}{\Delta t}[\mathcal{A}_{\boldsymbol{c}}(\boldsymbol{c} - \boldsymbol{c}^n), \boldsymbol{s}] - [\mathcal{G}(\boldsymbol{c}), \boldsymbol{s}].$$

Notice that if the reaction vector $\boldsymbol{G}$ is zero and the diffusion matrix is constant, then the (ADR2) solver reduces to a pure linear advection-diffusion problem (5.2.8). A global solver for the Brinkman-ADR problem is then obtained combining one of the two Brinkman solvers (B1) or (B2) and (ADR2). These solution strategies are summarized in Algorithm 5.

Data: σ, μ, ρ, $\boldsymbol{\alpha}$, $\boldsymbol{D}$, $\boldsymbol{G}$, Δt, N, tol ;
Initialize: $\boldsymbol{u}_h^0$, $\boldsymbol{\omega}_h^0$, p_h^0, $\boldsymbol{c}_h^0$;
for $n = 1, \ldots, N$ time steps **do**
  Given $\boldsymbol{c}_h^n$, **solve** the Brinkman system (B1):

$$\begin{pmatrix} \mathcal{A}_{\boldsymbol{u}} & \mathcal{B}_1 & \mathcal{B}_2 \\ \mathcal{B}_1^* & -\mathcal{A}_\omega & \mathbf{0} \\ -\mathcal{B}_2^* & \mathbf{0} & \mathbf{0} \end{pmatrix} \begin{pmatrix} \boldsymbol{u}_h^{n+1} \\ \boldsymbol{\omega}_h^{n+1} \\ p_h^{n+1} \end{pmatrix} = \begin{pmatrix} \mathcal{F}_1(\boldsymbol{c}_h^n) \\ \mathbf{0} \\ \mathbf{0} \end{pmatrix};$$

  or its split counterpart (B2):

  - $\widehat{\mathcal{A}}_{\boldsymbol{\omega}} \boldsymbol{\omega}_h^{n+1} = \mathcal{F}_2(\boldsymbol{c}_h^n)$,
  - $\widehat{\mathcal{A}}_p p_h^{n+1} = \mathcal{F}_3(\boldsymbol{c}_h^n)$,
  - $\boldsymbol{u}_h^{n+1} \leftarrow \mathcal{A}_{\boldsymbol{u}}^{-1} \mathcal{F}_1(\boldsymbol{c}_h^n)$;

  Update: $\boldsymbol{u}_h^{n+1} \leftarrow \boldsymbol{u}_h^n$; $\boldsymbol{\omega}_h^{n+1} \leftarrow \boldsymbol{\omega}_h^n$; $p_h^{n+1} \leftarrow p_h^n$;
  Given $\boldsymbol{u}_h^{n+1}$, **solve** the advection-diffusion phase:

$$\left(\mathcal{A}_{\boldsymbol{c}} + \mathcal{C}(\boldsymbol{u}_h^{n+1}) + \mathcal{D}\right) \boldsymbol{c}_h^{n+1,*} = \mathbf{0} \,;$$

  Initialize: $\boldsymbol{c}_h^{n+1,0} = \boldsymbol{c}_h^{n+1,*}$;
  Solve the pure reaction phase via Newton-Raphson:
  while $\|\delta \boldsymbol{c}_h\|_{\mathbf{L}^2(\Omega)} \geq \text{tol}$ **do**
    Solve the linearized reaction problem:

$$\left(\frac{\mathcal{A}_{\boldsymbol{c}}}{\Delta t} - d\mathcal{G}_{\boldsymbol{c}_h^{n+1,k}}\right) \delta \boldsymbol{c}_h - \mathcal{R}^{*,n}(\boldsymbol{c}_h^{n+1,k});$$

    Update: $\boldsymbol{c}_h^{n+1,k+1} \leftarrow \boldsymbol{c}_h^{n+1,k+1} + \delta \boldsymbol{c}_h$;
  end
  Update:
  $\boldsymbol{c}_h^{n+1} \leftarrow \boldsymbol{c}_h^n$;
end

Algorithm 5: Staggered procedure (B1/B2-ADR2) for the Brinkman problem solved with either (B1) or (B2) and the full ADR problem solved with (ADR2).

5.3 Numerical tests

This section contains a collection of numerical examples serving as validation of the coupling strategies discussed in Section 5.1.3, and illustrat-

ing the behavior of the model in applications of wide interest.

5.3.1 Double-diffusion in porous cavities

First, we perform a series of computations with a double-diffusive model governing the interaction between the concentration of brine (field c_1), temperature (encoded in c_2), and immiscible flow in saturated porous media (see (Ac13; QSM16)). The problem under consideration is a square cavity $\Omega = (0,1)^2$ filled by a fluid-saturated porous medium. The left and right vertical walls are maintained at different uniform temperatures and concentrations respectively $c_2^{\text{left}} = c_1^{\text{left}} = 0$ and $c_2^{\text{right}} = c_1^{\text{right}} = 1$. The horizontal walls are assumed adiabatic and insulated (that is, no-flux boundary conditions are set for the ADR system). Slip velocity conditions (i.e., zero normal velocities) and zero vorticity are imposed everywhere on the boundary, and the coupled system adopts the form (5.1.1) where diffusion, reaction, permeability, and forcing terms are defined as:

$$\boldsymbol{D}(\boldsymbol{c}) = \begin{pmatrix} \dfrac{1}{\mathrm{Le}\,\mathrm{Pr}} & 0 \\ 0 & \dfrac{R_k}{\mathrm{Pr}} \end{pmatrix}, \ \boldsymbol{G}(\boldsymbol{c}) = \mathbf{0}, \ \sigma = \frac{1}{\mathrm{Da}}, \ \boldsymbol{F}(\boldsymbol{c}) = \mathrm{Gr}(c_2 + \mathrm{N}c_1)\mathbf{g},$$

respectively. The remaining coefficients assume the values $\mathrm{Da} =$, $\mathrm{Gr} =$, $N =$, $R_k =$, $\mathrm{Pr} =$, $\mathrm{Le} =$, $\mathbf{g} = (0,-1)^T$, $\mu =$, $\rho = 1$.

The buoyancy term N can be considered as a measure of the strength of the coupling between the flow and the ADR problem. Moreover, once $\boldsymbol{u}$ is given, the ADR equations conforms a linear problem in which the reaction vector is zero, therefore representing a suitable benchmark to test the efficiency of the splitting method (B1)/(B2)-(ADR2).

In order to investigate the robustness of the proposed (B1-ADR2) splitting method with respect to the coupling strength, we fix the parameters $\mathrm{Le} = 10$, $\mu = \Lambda = 1$, $\mathrm{Da} =$1E-3, $R_k = 1$, $\mathrm{Pr} = 0.71$, $\epsilon = 0.5$, $\mathrm{Ra} = 100$, $\mathrm{Gr} = \mathrm{Ra}/(\mathrm{PrDa})$, we use a timestep $\Delta t =$1E-3 and a structured grid of meshsize $h = 1/100$, and let the buoyancy term N vary. By $\boldsymbol{\chi}_h^{\text{MONO}}$ and $\boldsymbol{\chi}_h^{\text{SPLIT}}$ we will denote the finite element solution (at the final time $T = 0.5$) generated by the fully monolithic approach, and the operator splitting method (B1-ADR2), respectively. A comparison is then per-

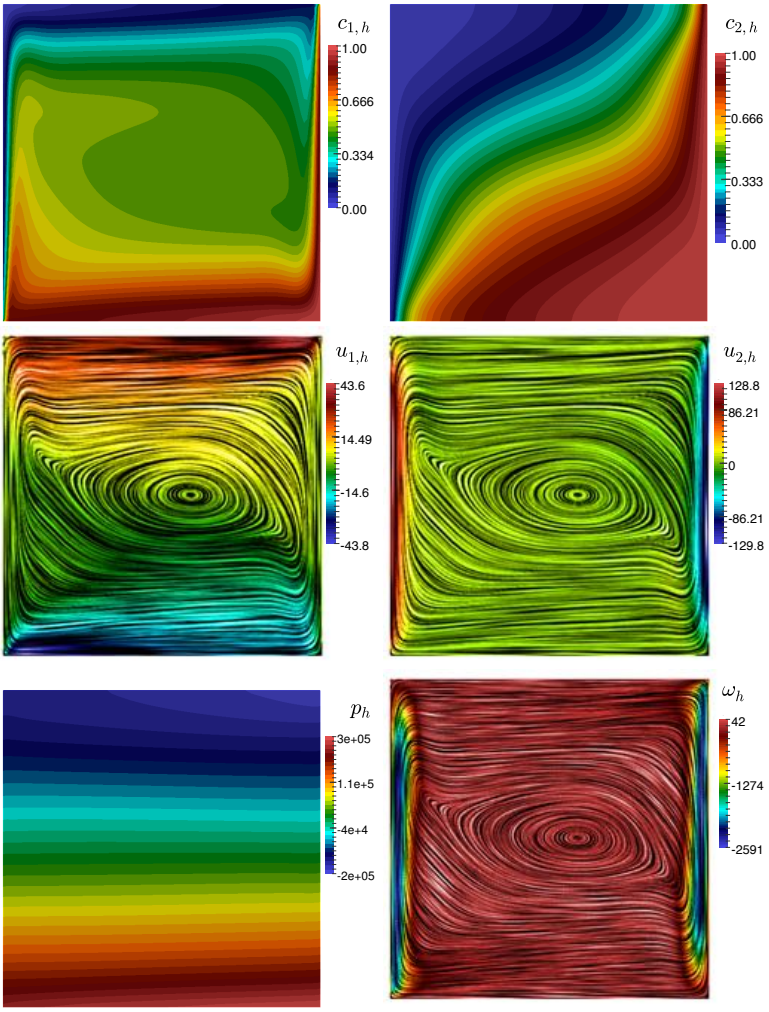

Figure 33: Example 1A. Double diffusion in a porous cavity, 2D case. Approximate solutions at the final time (brine concentration, temperature, pressure, velocity components, and vorticity).

formed in terms of the evolution of global errors defined as the L^2- norm of the difference between the two solutions $\varepsilon_h(\boldsymbol{\chi}) = \|\boldsymbol{\chi}_h^{\text{MONO}} - \boldsymbol{\chi}_h^{\text{SPLIT}}\|$,

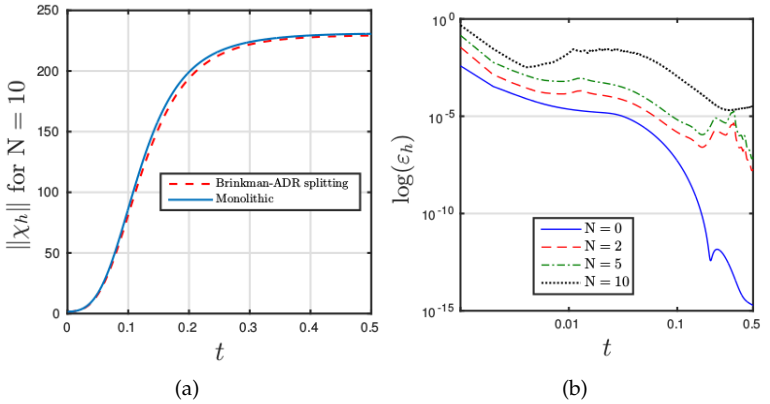

Figure 34: Example 1A. (a) Evolution of the norm of the solution $\boldsymbol{\chi}_h$ in the Double diffusion problem with high bouyancy term $\mathrm{N} = 10$ using both the Monolithic and the proposed (B1)-(ADR2) splitting. Evolution of the error $\varepsilon(\boldsymbol{\chi}_h)$ between the solution obtained using the Monolithic and the Splitting method (B1)-(ADR2) for $\mathrm{N} = \{0, 2, 5, 19\}$.

where the approximation produced by the monolithic method is considered as a reference solution. In Figure 34 we report the temporal evolution of $\varepsilon_h(\boldsymbol{\chi})$ for different values of the buoyancy $\mathrm{N} \in \{0, 2, 5, 10\}$. As N increases, the error grows, implying that the coupling strength affects substantially the quality of the solution generated by the segregated solver. For reference we also depict each individual field of the numerical solution generated with the splitting method, shown at the final time $T = 0.5$, in Figure 33.

The results of the finite element model proposed are compared with published results on the purely thermal problem (decoupled thermal and mass $\mathrm{N} = 0$). Consider the square domain $\Omega = (0, 1)^2$ and set the boundary conditions as:

$$c_1 = c_2 = 1 : \ x = 0, \quad c_1 = c_2 = 0 : \ x = 1, \quad \boldsymbol{u} = \mathbf{0} : \ \partial\Omega.$$

We fix the parameters $\mathrm{N} = 0$, $\mathrm{Le} = 10$, $\mu = \Lambda = 1$, $R_k = 1$, $\mathrm{Pr} = 0.71$, $\epsilon = 0.5$, $\mathrm{Ra} = 100$, $\mathrm{Gr} = \mathrm{Ra}/(\mathrm{PrDa})$ and let vary $\mathrm{Da} \in \{10^{-1}, 10^{-3}, 10^{-5}\}$

and $\mathrm{Ra} \in \{100, 200\}$. The comparisons are based on the average Nusselt and Sherwood numbers:

$$\overline{\mathrm{Nu}} = -\int_0^1 \frac{\partial c_1}{\partial x}|_{x=0}\, \mathrm{d}y, \quad \overline{\mathrm{Sh}} = -\int_0^1 \frac{\partial c_2}{\partial x}|_{x=0}\, \mathrm{d}y. \tag{5.3.1}$$

The (B1-ADR2) scheme is used on a regular mesh containing 20000 triangles, considering a timestep of $\Delta t = 0.01$ and the system is run until $T = 2$. The computed numbers are collected in Table 3.

Da	Ra	Ref. $\overline{\mathrm{Nu}}$	Comp. $\overline{\mathrm{Nu}}$	Ref. $\overline{\mathrm{Sh}}$	Comp. $\overline{\mathrm{Sh}}$
10^{-1}	100	1.52	1.52	5.56	5.60
	200	2.07	2.10	7.32	7.50
10^{-3}	100	2.96	3.01	12.33	11.90
	200	4.43	4.64	17.58	16.57
10^{-5}	100	3.11	3.13	13.40	13.25
	200	4.96	5.01	19.52	19.25

Table 3: Example 1A. Average Nusselt and Sherwood numbers $\overline{\mathrm{Nu}}$ and $\overline{\mathrm{Sh}}$ obtained with the (B1-ADR2) splitting in the case of decoupled mass and heat transfer processes ($\mathrm{N} = 0$, $\mathrm{Le} = 10$) and comparison against reference results published in Shao et al. (QSM16).

Next we carry out a simulation of double-diffusion-driven natural convection in a porous 3D enclosure. The problem setting follows (JK13b). The splitting method used is (B2)-(ADR2) with the second Brinkman solver.

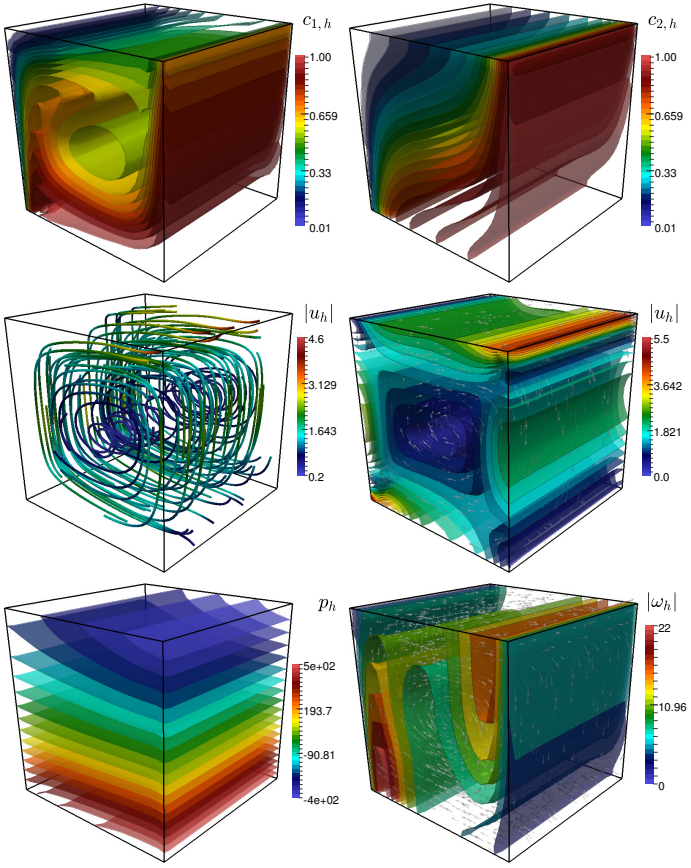

Figure 35: Example 1B. Double diffusion in a porous enclosure, 3D case. Approximate solutions at the final time (brine concentration, temperature, pressure, velocity streamlines, velocity magnitude, and vorticity magnitude).

5.3.2 Exothermic reaction-diffusion in porous media

Let us now consider a rectangular domain $\Omega = (0, L) \times (0, H)$ and endow (5.1.1) with the following specification of diffusion, reaction, permeability and forcing terms, respectively:

$$\boldsymbol{D}(\boldsymbol{c}) = \begin{pmatrix} 1 & 0 \\ 0 & \mathrm{Le} \end{pmatrix}, \ \boldsymbol{G}(\boldsymbol{c}) = \mathrm{Da}\, f(c_1) \begin{pmatrix} -1 \\ 1 \end{pmatrix}, \ \sigma = \frac{1}{\mathrm{Da}}, \ \boldsymbol{F}(\boldsymbol{c}) = (\gamma_T - c_1)\mathbf{g}, \tag{5.3.2}$$

where $f(c_1) = 36c_1(\kappa + 7c_1)(1 - c_1)^2$ and $\mathbf{g} = (0, -1)^{\mathrm{T}}$. Denoting c_1 and c_2 respectively as concentration of solutal and temperature inside the fluid, the dynamical system defined by (5.1.1) and (5.3.2) represents a two-dimensional porous medium with the gravity field along the streamwise direction, in which solutal and thermal density have compeating behavior. Let us consider initial conditions are concentrated near the top of the rectangular region:

$$c_i^0(x, y) = \begin{cases} 0.999 + \zeta_i(0.001) & \text{if } H - \epsilon \leq y \leq H, \\ 0 & \text{otherwise} \end{cases}, \quad i = 1, 2, \tag{5.3.3}$$

where ζ_1, ζ_2 are random variabes uniformly distributed in the interval $[0, 1]$. The resulting chemical front moves downwards invading the fresh reactants. Instability results from the competition between solutal and thermal effects through the kinetic term $f(c_1)$ and the buoyancy term $(\gamma_T - c_1)\mathbf{g}$. Downward traveling fronts are buoyantly unstable and develop solutal density fingers in time. Numerical values for (5.3.2) are

$$H = 1000, L = 2000, \Delta t = 40, T_f = 8000, Le = 8, Da = 0.001, \gamma_T = 5$$

Because the diffusion matrix is constant and the reaction term is highly nonlinear, we numerically solve this problem using the splitting (B1)-(ADR2).

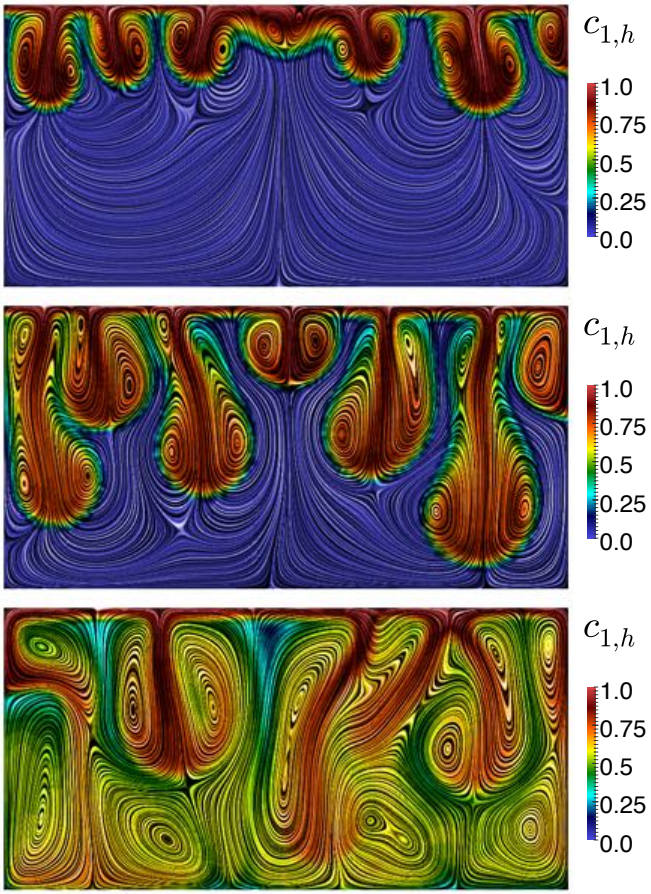

Figure 36: Example 2. Exothermic fingers within porous media. Snapshots of concentration c_1 at different times.

The domain is discretized into 26848 elements with 13675 vertices. The number of degrees of freedom for the Brinkman problem is 81045, while for the ADR is 27350. In Figure 37 we report on the CPU times for solving the Brinkman-ADR problem defined by (5.3.2) using the (B1-ADR2) solver with the inner splitting of the ADR problem into a pure

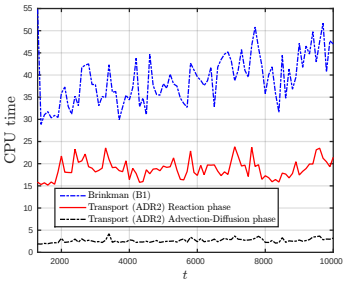

Figure 37: Example 2. Evolution of the required CPU time for the solution of the Brinkman problem using (B1) and for the ADR problem using the sub-splitting into a pure Advection-Diffusion phase and a pure Reaction phase (ADR2) at each time step. Number of Newton-Raphson iteration needed to reach convergence in the pure Reaction phase with a fixed tolerance tol$= 1e-10$.

advection-diffusion phase and into a pure reaction phase (ADR2). We notice that the computational cost of the nonlinear, pure reaction phase is much higher than that of the linear advection-diffusion phase. As a matter of fact, the rate of convergence of the Newton-Raphson iterative procedure to solve the former is only linear in the sense that $\|\boldsymbol{c}_h^{n+1,k+1} - \boldsymbol{c}_h^{n+1,k}\|_{\mathbf{L}^2(\Omega)} \approx$1E-$k$ (i.e. to reach k digits of precision in the solution of the pure reaction problem approximately k Newton-Raphson iterations are needed), as shown in Figure 37. The evolution of the norms of the gradient of the concentration, is shown in Figure 38.

In correspondence with the developing of finger instabilities, there is a peak in $\|\nabla \boldsymbol{c}_h\|_{\mathbf{L}^2(\Omega)}$ and a subsequent decay towards a spatially homogeneous configuration.

5.3.3 Bioconvection of oxytactic bacteria

Let us consider a rectangular box where both bacteria and oxygen coexist within a porous array of fixed particles, filled with an incompressible fluid. After removing the top lid of the box, an interaction between bacteria and the diffusion of oxygen into the liquid onsets the formation of high bacterial concentrations moving towards the bottom of the box. As

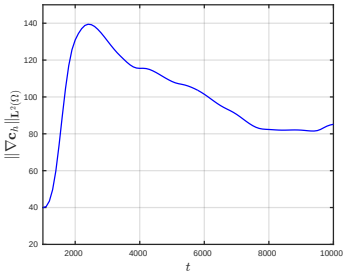

Figure 38: Example 2. Evolution of the norm of the gradient $\|\nabla \boldsymbol{c}_h\|_{\mathbf{L}^2(\Omega)}$.

proposed in (HP96), an adequate model for this phenomenon is (5.1.1) with a cross-diffusion term, where we identify the concentration of bacteria with the field c_1 and that of oxygen with c_2 and

$$\boldsymbol{D}(\boldsymbol{c}) = \begin{pmatrix} D_1 & -\alpha r(c_2)c_1 \\ 0 & D_2 \end{pmatrix}, \ \boldsymbol{G}(\boldsymbol{c}) = \begin{pmatrix} 0 \\ -\beta r(c_2) \end{pmatrix}, \ \boldsymbol{F}(\boldsymbol{c}) = \gamma c_1 \mathbf{g}, \quad \sigma = \frac{1}{\mathrm{Sc}}, \tag{5.3.4}$$

where $r(c_2) = \frac{1}{2}(1 + (c_2 - c_2^*)/\sqrt{(c_2 - c_2^*)^2 + \varepsilon^2})$, $\mathbf{g} = (0, -1)^{\mathrm{T}}$ and $c^* = 0.3$ is a fixed threshold and ε^2 is a regularizing parameter.

It is known (see (HP96)) that for suitable parameters, the solution of the ADR problem (c_1, c_2) converges to a homogeneous in x steady state solution of the following system:

$$\Delta c_1 = \alpha \nabla \cdot [c_1 r(c_2) \nabla c_2], \quad \delta \Delta c_2 = \beta r(c_2) c_1,$$

where $\delta = D_2/D_1$. Consider a rectangular domain $\Omega = [0, 2] \times [0, 1]$ and initial conditions given by:

$$c_1^0(x, y) = \begin{cases} 1 \text{ if } y \geq 0.501 - 0.01(\sin((x - 0.5)\pi), \\ 0.5 \text{ otherwise} \end{cases}, \ c_2^0(x, y) = 1$$

Fixing parameters $\beta = 10$, $\delta = 1$, $\gamma = 418$ and $\mathrm{Sc} = 7700$ and varying α leads to such a quasi-stationary solution. We used the Brinkman-ADR splitting (B1)-(ADR1) to solve this problem numerically running

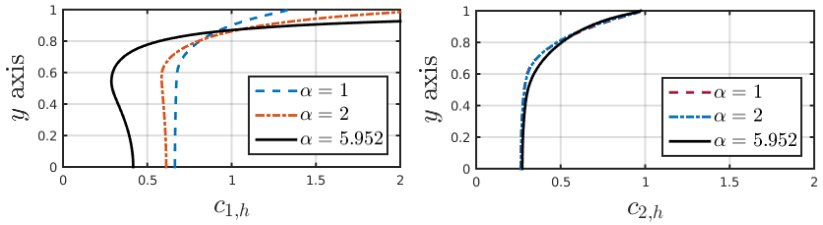

Figure 39: Example 3A. Vertical profiles of (left) cell density $c_{1,h}$ and (right) oxygen $c_{2,h}$ at $t = 0.22$ for $\beta = 10$, $\delta = 1$, $\gamma = 418$, Sc $= 7700$, and $\alpha = \{1, 2, 5.952\}$.

the code untill convergence to a seady-state solution, using $\Delta t = 10^{-3}$. The vertical profiles of the cell c_1 density and oxygen c_2 at $t = 0.22$ for $\alpha = \{1, 2, 5.952\}$ are shown in Figure 39.

As the value of α increases (β and δ fixed), the cell density near the surface increases, the cells vacate the lower regions of the chamber more rapidly, and less overall oxygen consumption occurs in these regions. These are in qualitative agreement with Figure 7 in (JK13a).

For $\alpha = 10, \beta = 10, \gamma = 1000, \delta = 5$ and Sc $= 500$ we run the code using (B1)-(ADR1) solver. The solution of the ADR shows bioconvection patterns evolving in time. At around $t = 0.2$ the solution starts developing instabilities, at $t = 0.25$ a drop of bacterial concentration c_1 starts falling down and hits the bottom of the chamber at $t = 0.3$.

In Figure 41 (left) is reported the scaled norm of the solution $\|\boldsymbol{\chi}_h\|^2$. It is evident that $\|\boldsymbol{\chi}_h\|^2$ has a pick in correspondence of the developing of instabilities of the solution due to spatial inhomogeneity. In Figure 41 (right) is shown the number of Newton-Raphson iteration to find a solution of the ADR monolithic system in solver (ADR1) with an error less than a tolerance tol $= 10^{-13}$. We can observe an increase of the number of iteration when the solution starts to be unstable due to the strongest nonlinearity behaviour of the system.

The second round of simulations is performed on a 3D setting. We consider a cylindrical geometry of radius 1 and height 0.75, discretized

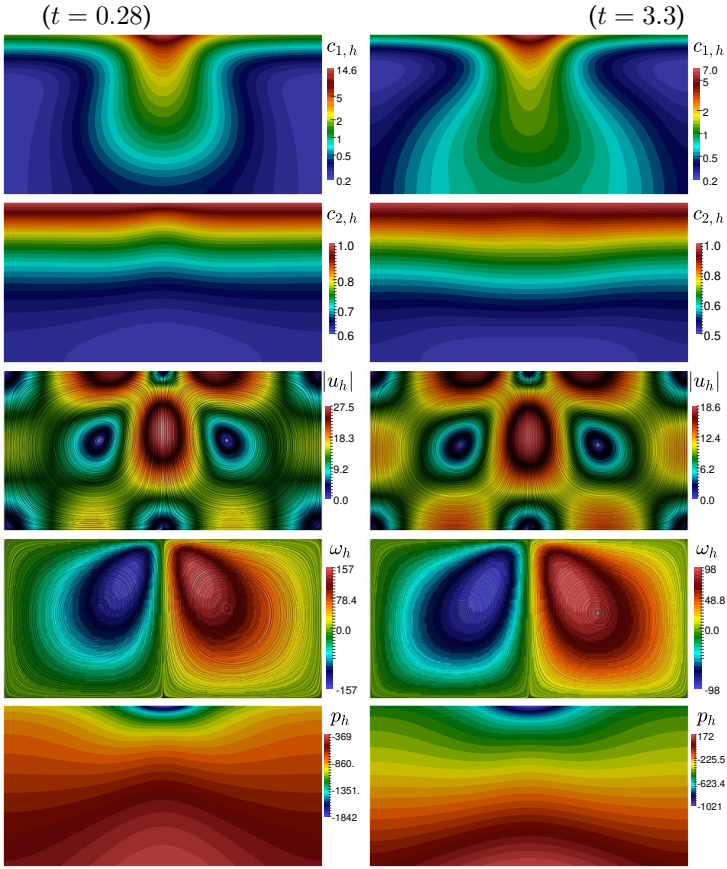

Figure 40: Example 3A. Snapshots at mid (top) and advanced (bottom) times of cell density, oxygen concentration, velocity magnitude, vorticity, and pressure.

into a tetrahedral mesh of 169392 cells and 29109 points. The configuration of the governing equations and specification of constant and variable coefficients is given as follows: $\alpha = 0.25$, $\beta = 1.5$, $\gamma = 1500$, $D_1 = 0.005$, $D_2 = 0.4$, $S = 7700$, $\sigma = S^{-1} \times 1\,\mathrm{E}\,6$, $s^\star = 0.3$, $\mu = 2$. A fixed timestep of $\Delta t = 5\,$E-4 is used, and we test the capabilities of differ-

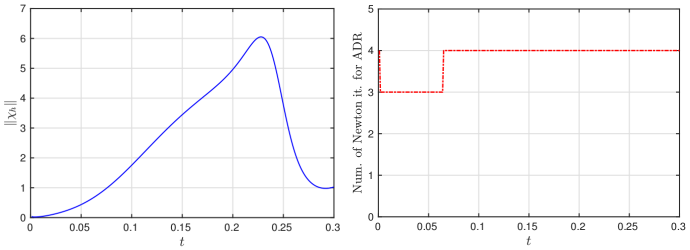

Figure 41: Example 3A. Plot of the (rescaled) norm of the solution χ_h over time (left) and number of Newton-Raphson iterations in the solution of the ADR system using (ADR1) solver (right).

ent partitioned coupling methods (B1)/(B2)-(ADR1) based on the monolithic and the splitting Brinkman solvers (B1) and (B2) defined by (5.1.3) and (5.1.4), respectively. For the first coupling (B1)-(ADR1), the solve involves the preliminary assembly of the Brinkman system (arising from a finite element discretization using lowest order Raviart-Thomas approximation of velocity, first degree Nédélec elements for vorticity, and piecewise constants for pressure) representing 678020 degrees of freedom, and the assembly of the ADR equations, where the piecewise linear discretization of the bacteria and oxygen concentrations leads to a system of 58218 unknowns. The second coupling strategy (B2)-(ADR1) has a Brinkman solve split into a vorticity matrix of size 193724 (also using Nédélec finite elements), a pressure solution with 29109 degrees of freedom, and a matrix-vector multiplication to project the reconstructed velocity on the Raviart-Thomas space. This second coupling (B2) results in a much more attractive strategy, especially in view of 3D cases, as the vorticity is a vector field. As a reference, let us point out that the monolithic solver (B1) requires the assembly and solution (at each Newton step) of a system with 736238 degrees of freedom. We simulate the evolution of the system starting from an initial uniform oxygen concentration $c_2 = 1$ and an initial distribution of bacteria packed in a ball of radius 0.2 and placed near the top of the vessel. Snapshots of the concentration of bacteria and the associated flow patterns, computed with the first

staggered solution method, are portrayed in Figure 43. We observe that as the bacteria propagate downwards, the velocity and vorticity fields indicate recirculating zones following the high gradients of c_1, whereas the pressure exhibits smooth transitions from high to low values on the bottom and top of the domain, respectively. As soon as the high bacteria concentration reaches the bottom of the vessel (ocurrying approximately at $t = 0.2$), the dynamics of the system implies a slightly loosleier coupling between flow and transport. This is particularly noticed in the top right plot of Figure 42, where the CPU times for assembly and solution of the Brinkman and ADR systems displays a slight step down happening around $t = 0.2$. The timings reported in the top panels of the figure encompass the RHS assembly and solution for the Brinkman equations, and the assembly of the stiffness matrix and solution of the ADR equations. On top of these values, the initial assembly of the stiffness matrix of the Brinkman problem and the RHS of the ADR equations represents an average of additional 124.91 time units for the first partitioned solver (B1), and 28.31 time units for the second decoupling strategy (B2). In general, the CPU time for the flow solution is roughly half that for the transport. We also observe that for the second coupling the CPU usage for the total solution is approximately 75% lower than the one in the first coupling. The second row of Figure 42 presents the history of bacteria concentration, oxygen quantity, and vorticity magnitude computed on the point $(x_0, y_0, z_0) = (0.6, 0.6, 0.6)$, indicating that the solution itself differs from one coupling to the other. In particular, the second coupling (B2) produces a slower decay of the bacteria concentration and vorticity fronts.

As last example case, we study the solution of the bioconvection system defined by (5.1.1) and (5.3.4) with parameters:

$$\alpha = 5, \beta = 20, \gamma = 2 \times 1e3, D_1 = 5, D_2 = 1, Sc = 500,$$

in a rectangular region $\Omega = [-3, 3] \times [0, 1]$. As initial data, we consider homogeneous initial data with a random perturbation in the cell concentration

$$c_1^0(x, y) = 0.8 + \zeta(0.2), \quad c_2^0(x, y) = 1,$$

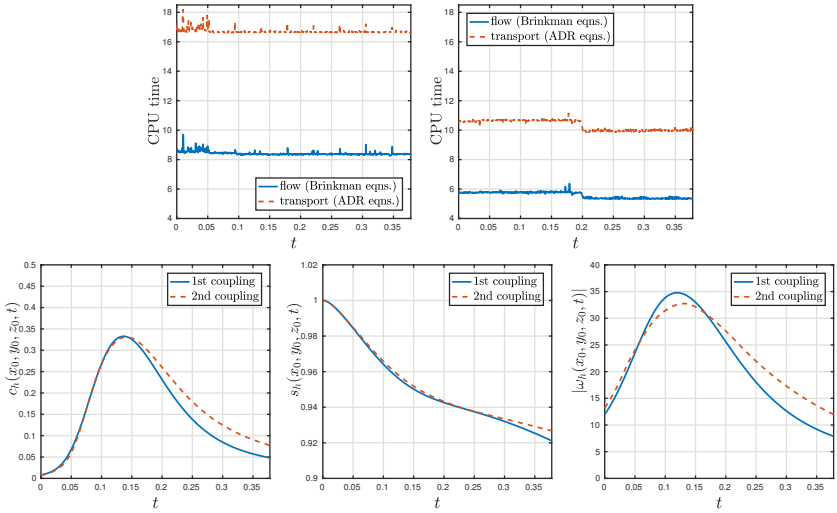

Figure 42: Example 3B. Evolution of the required CPU time (adiemensional units) for the solution of the flow and transport problems at each time step (solid and dashed lines, respectively), for the first (B1)-(ADR1) and second (B2)-(ADR1) splitting algorithms (top left and top right plots, respectively). The bottom panels show the evolution of the bacteria concentration, oxygen, and vorticity magnitude on a single point near the domain center.

where ζ is a random variable uniformly distributed in the interval $[0, 1]$. Figure 44,45, 46, 47 show the time evolution of c_1 cells and c_2 oxygen, $|\boldsymbol{u}|$ magnitude of the velocity, ω and p pressure the computed solution using the splitting (B1)-(ADR1). We observe already at time $t = 0.16$ several instabilities in the cell density of bacteria. At $t = 0.32$ instabilities, amplifying the random irregularities of the initial data, are developing into four falling plumes.

$(t = 0.05)$

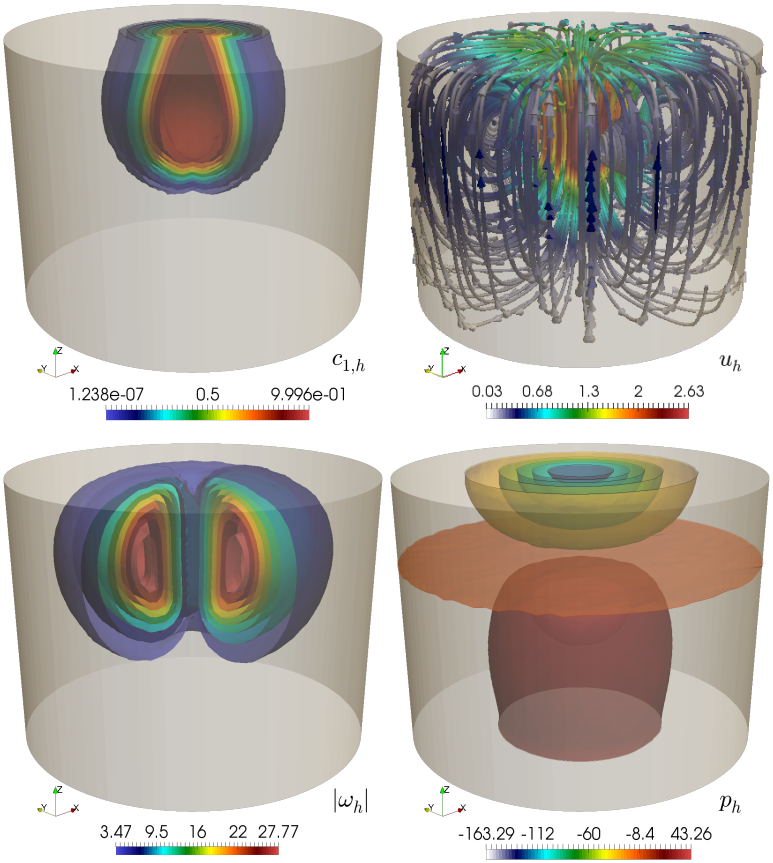
$c_{1,h}$
1.238e-07 0.5 9.996e-01
u_h
0.03 0.68 1.3 2 2.63
$|\omega_h|$
3.47 9.5 16 22 27.77
p_h
-163.29 -112 -60 -8.4 43.26

$(t = 0.2)$

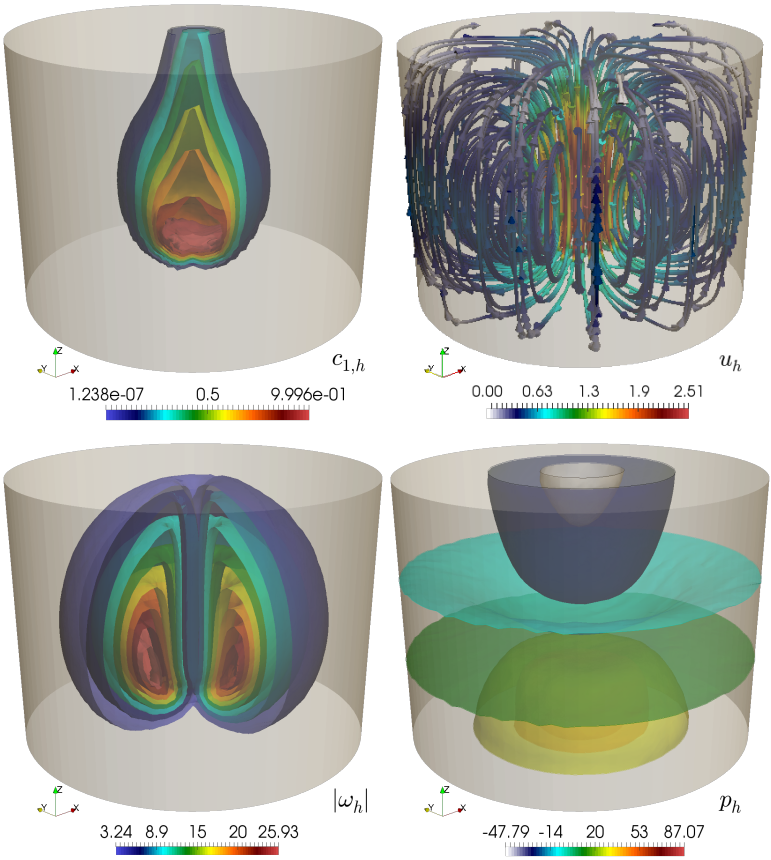
$c_{1,h}$
1.238e-07 0.5 9.996e-01
u_h
0.00 0.63 1.3 1.9 2.51
$|\omega_h|$
3.24 8.9 15 20 25.93
p_h
-47.79 -14 20 53 87.07

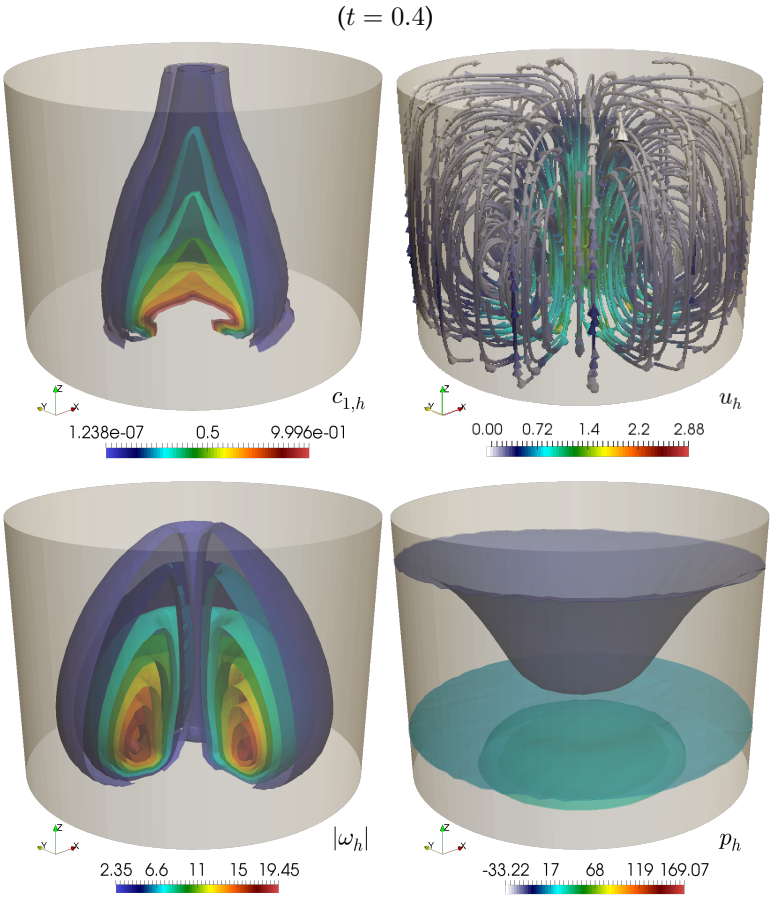

Figure 43: Example 3B. Snapshots at three instances of cell density (left), velocity patterns and vorticity magnitude (middle columns), and pressure distribution (right panels).

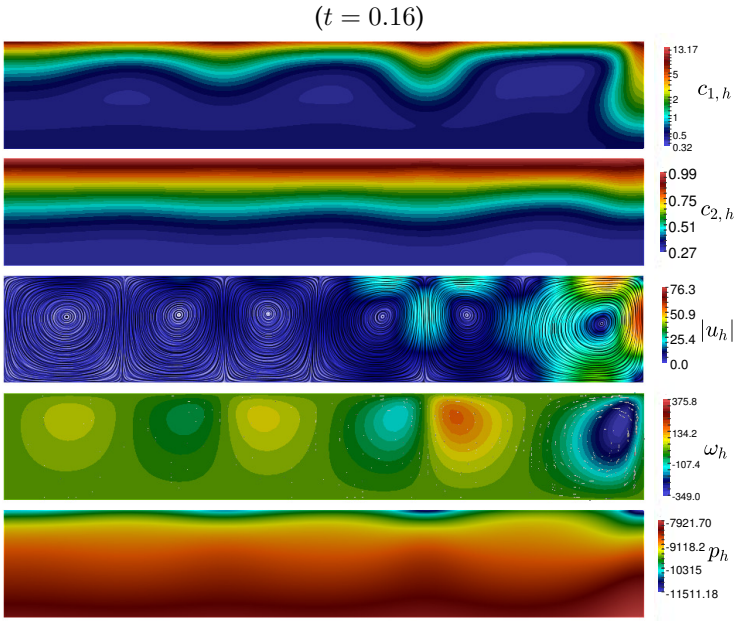

Figure 44: Example 4. Patterns generated by the bioconvection of bacteria towards oxygen concentration at time $t = 0.16$.

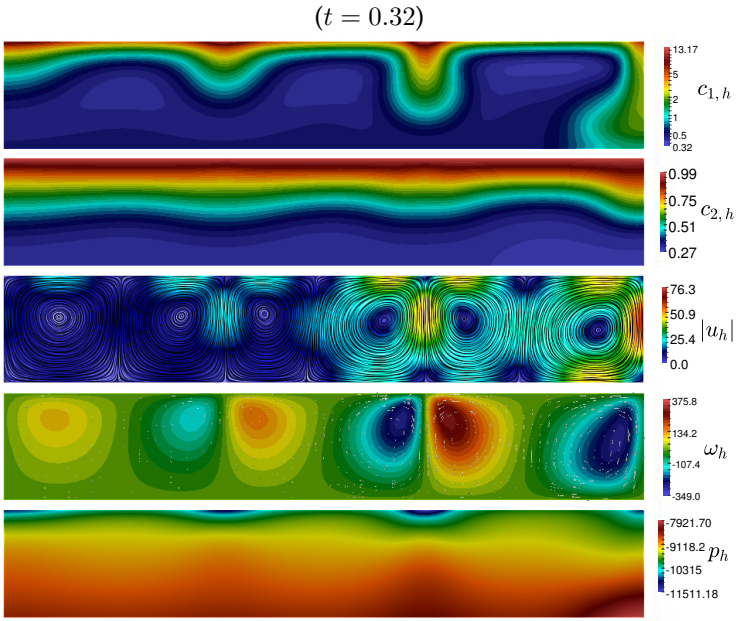

Figure 45: Example 4. Patterns generated by the bioconvection of bacteria towards oxygen concentration at time $t = 0.32$.

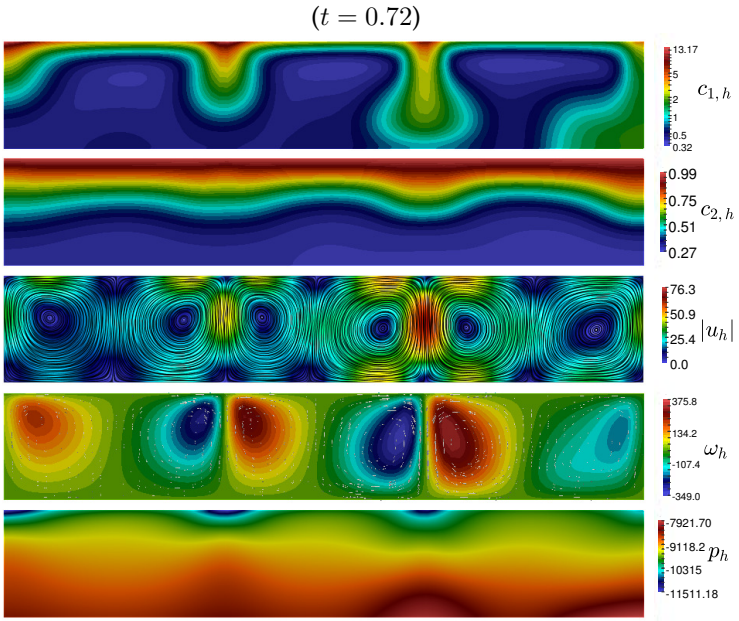

Figure 46: Example 4. Patterns generated by the bioconvection of bacteria towards oxygen concentration at time $t = 0.72$.

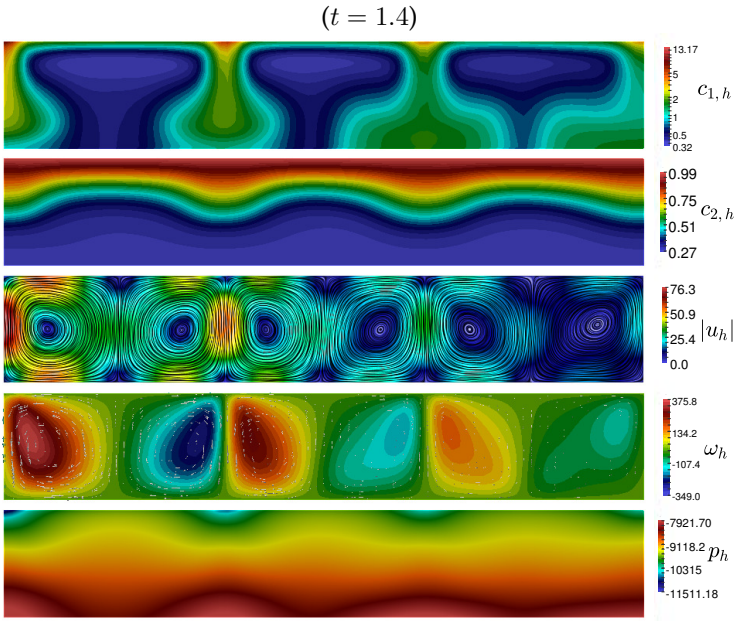

Figure 47: Example 4. Patterns generated by the bioconvection of bacteria towards oxygen concentration at time $t = 1.4$.

Chapter 6

Conclusions

This thesis deals with the development of novel numerical methods for the solution of a large class of problems in the field of generalized thermo-diffusion in visco-elasticity and in advection-reaction-diffusion systems in Brinkman flows. The nonlinearities involved in those mathematical systems, as well as the presence of dynamical behaviours characterized by very different time scales can lead to numerical problems that are difficult to treat using fully coupled monolithic approaches. To deal with these problems efficiently, splitting-operator time integration techniques are explored in order to decouple the dynamics of the various physical phenomena. The analysis has played a new incisive role to make simulations and predictions in many applicative problems in which a multi-physic approach is needed to capture fully coupled effects.

- A novel constituive model in the framework of fractional calculus has been proposed for modelling the thermo-rheologically complex behavior of visco-elastic polymeric materials. The theory of Mittag-Leffler special functions has been employed in the accurate description of the time relaxation behaviour of the material. An internal material clock has been introduced to model the thermo-rheological complexity of materials in which the time-temperature superposition principle does not apply. For the finite element formulation of the thermo-visco-elastic problem has been used the

Grünwald-Letnikov approximation of the fractional derivative leading to an additional load vector which represents the memory of the material in the discretized system of equations resulting from the finite element formulation.

- A comprehensive finite element computational framework for the simulation of thermo-diffusive phenomena taking place along polymeric layers of photovoltaic laminates has been proposed. While the thermo-mechanical problem takes place in the 3D space of the laminate, moisture diffusion occurs in a 2D domain represented by the polymeric layers. Therefore, a geometrical multi-scale solution strategy has been adopted by solving the partial differential equations governing the thermo-elasticity problem in the three-dimensional space, and the partial differential equation for moisture diffusion in the two dimensional domains. By exploiting a staggered scheme, the thermo-mechanical problem is solved first via a fully implicit solution scheme in space and time, with a specific treatment of the polymeric layers as zero-thickness interfaces whose constitutive response is governed by a novel thermo-visco-elastic cohesive zone model based on fractional calculus. Then, temperature T inside the polymeric layer, found at the previous step, is used to calculate the diffusivity $D(T)$ of the moisture diffusion process in 2D. The proposed methodology has been successfully applied to the simulation of the qualification tests for the durability of photovoltaic modules required by the International Electrotechnical Commission (61215), namely the damp heat test and the humidity freeze test.

- A computational framework based on the finite element method has been proposed to simulate the chemical reactions and diffusion processes occurring in the degradation of Poly(ethylene-co-vinyl acetate) (EVA) used as encapsulant in photovoltaic (PV) modules due to aging. The derived finite element procedure, specifically distinguished for the case of environmental degradation or accelerated aging, represents a comprehensive tool for the prediction of

the spatio-temporal evolution of the chemical species in the encapsulant, and the assessment of the lost of physico-chemical properties due to aging. Simulations were carried out to find the solution of the degratation process after 20 years of environmental exposure. This reference solution has been compared with that obtained from simulations of accelerated aging tests in climatic chambers. In the last case a splitting strategy has been adopted to decouple the heat transfer process in the EVA, which is a fast dynamics due to the high temperature ranges the module is subjected in climatic chambers, from the slow chemical degradation process taking place in the material. The method has been revealed very efficient to quantitatively compare the degradation resulting from any environmental condition to that from accelerated aging tests, providing a tool to design new testing protocols tailored for specific climate zones.

- A set of coupling strategies has been introduced for the partitioned solution of advection-reaction-diffusion equations interacting with viscous flows in porous media governed by Brinkman equations in their velocity-vorticity-pressure formulation. The flow equations follow a discretization with, either a family of $\mathbb{RT}_0 - \mathbb{N}_1 - \mathbb{P}_0$ finite elements, or via a split between two elliptic solvers for vorticity and pressure plus a postprocessing yielding velocity. In turn, the advection-reaction-diffuson system is solved with a primal finite element method using piecewise linear approximations of the species concentration, and a splitting of reaction and diffusion steps is conducted in different ways, according to the coupling strength exhibited by each particular application. Both accuracy and robustness of the proposed schemes have been demonstrated by means of several numerical tests, involving bioconvection of oxytactic bacteria.

6.1 Future developments

The splitting techniques used in the present dissertation will be extensively used for applications in bio-mechanics. The accurate modelling and computational simulations of active soft tissues and excitable deformable cells represents a major field of research due to the complexity of the involved interactions. The coupling between the propagation of electrical potential and large deformations of the cardiac tissue is ruled by a system of partial differential equations that is going to be described briefly.

Let $\mathbf{x} \in \Omega$ denote the current position of a particle that occupied the position $\mathbf{X} \in \Omega_0$ in the initial undeformed configuration of the cardiac tissue, and $\mathbf{u} = \mathbf{x} - \mathbf{X}$ will stand for the displacement field. Then,

$$\mathbf{F} = \mathbf{I} + \nabla \mathbf{x} = \mathbf{I} + \nabla \mathbf{u}, \quad F_{ij} = \frac{\partial x_i}{\partial X_j} = \delta_{ij} + \frac{\partial u_i}{\partial X_j}$$

where δ_{ij} denotes the Kronecker delta and $\mathbf{F}$ is the deformation gradient tensor, measuring strain between the deformed and undeformed states. The symbol ∇ denotes the gradient of a quantity with respect to the material coordinates $\mathbf{X}$. Let $J = \det(\mathbf{F})$ denote the jacobian of $\mathbf{F}$. It is assumed (NQRB12) that $\mathbf{F}$ can be decomposed as $\mathbf{F} = \mathbf{F}_e \mathbf{F}_a$. Let $\mathbf{a}_l$, $\mathbf{a}_t$ be the fiber sheet longitudinal and transversal directions respectively, and γ_l, γ_t are scalar fields accounting for the electrical activation. The active strain assumes the form:

$$\mathbf{F}_a = \mathbf{I} + \gamma_l \mathbf{a}_l \otimes \mathbf{a}_l + \gamma_t \mathbf{a}_t \otimes \mathbf{a}_t.$$

Given the special constitutive form of $\mathbf{F}_a$, under transverse anisotropy, we can readily write:

$$J_a = (1 + \gamma_l)(1 + \gamma_t),$$

the variables γ_t depends on:

$$\gamma_t = -\frac{\gamma_l}{1 + \gamma_l}.$$

The Piola stress tensor $\mathbf{P}$ is:

$$\mathbf{P} = \mu J_a \mathbf{F}\mathbf{F}_a^{-1}\mathbf{F}_a^{-T} - Jp\mathbf{F}^{-T},$$

where p is the Lagrange multiplier arising from the imposition of the incompressibility constraint $J = 1$ (conservation of mass) and which is usually interpreted as the hydrostatic pressure field. The conductivity of the tissue is represented by the tensor $\mathbf{D}$ given by:

$$\mathbf{D} = \sigma_l \mathbf{a}_l \otimes \mathbf{a}_l + \sigma_t \mathbf{a}_t \otimes \mathbf{a}_t,$$

where σ_l, σ_t are intracellular and extracellular conductivities along the directions $\mathbf{a}_l$ and $\mathbf{a}_t$. Let v be the transmembrane potential, w the calcium concentration and γ_l activation variables. The weak formulation of the coupled electro-mechanical model reads (all integrals in $d\mathbf{X}$) (NQRB12; CFG12):

$$\begin{aligned}
\mu \int_{\Omega_0} J_a \mathbf{F}\mathbf{F}_a^{-1}\mathbf{F}_a^{-T} : \nabla \mathbf{v} - \int_{\Omega_0} Jp\mathbf{F}^{-T} : \nabla \mathbf{v} = 0 \\
\int_{\Omega_0} (J-1)q = 0 \\
\int_{\Omega_0} \partial_t (Jv)\xi + \int_{\Omega_0} J\mathbf{F}^{-1}\mathbf{D}\mathbf{F}^{-T}\nabla v \cdot \nabla \xi - \int_{\Omega_0} JI\xi - \int_{\Omega_0} JI_{app}\xi = 0 \\
\int_{\Omega_0} \partial_t (Jw)\phi - \int_{\Omega_0} JH\phi = 0
\end{aligned}$$

The electrophysiological functions are:

$$\begin{aligned}
I(v,w) &= c_1 v(v-a)(1-v) - c_2 vw \\
H(v,w) &= b(v - dw),
\end{aligned}$$

where coefficients are $a = 0.13, b = 0.013, c_1 = 0.26, c_2 = 0.1, d = 1.0$ and the components of the diffusion matrix $\mathbf{D} = \text{diag}(D1, D2)$ are $D_1 = D_2 = 1e-3$ (which corresponds to fibers $\mathbf{a}_l = \mathbf{e}_1, \mathbf{a}_t = \mathbf{e}_2$). The function I_{app} is a given impulse. The link between the electrophysiological

variables v and w and γ_l is (CFG12):

$$f_{Ca}(w) = \frac{1}{2} + \frac{1}{\pi}\text{atan}\left(\beta_c \log\left(\frac{w}{c_0} + 1e-5\right)\right)$$
$$\lambda_{Ca} = \frac{f_{Ca}(c^*) - 1}{f_{Ca}(c^*) - \gamma_0^{\max}}$$
$$\gamma_0 = \gamma_0^{\max}\frac{\lambda_{Ca}}{(1 + f_{Ca}(w))}$$

and finally $\gamma_l = \gamma_0 - 1$. where: $\beta_c = 6, c_0 = 3.2\times 1e-1, c^* = 1e-1, \gamma_0^{\max} = 0.8$.

A progress with respect to the State-of-the-Art requires a novel framework which incorporates the modelling of biological cell-cell interactions within a multi-field approach. Cardiomyocytes transfer tractions and electic signals across their boundaries (CIY01), (MML12). Current propagation of electrical impulse between cells is ruled by clusters of intercellular proteic channels, namely gap junctions that are voltage and time-dependent and can induce effects on the overall cellular dynamics.

Two myocytes i and j are assumed to occupy domains Ω_i and Ω_j in the reference configurations. Ω_i and Ω_j are separated by an internal boundary Γ. Consider the normal and tangential displacement gaps at the interface $g^n_{i,j} = (\mathbf{u}_i - \mathbf{u}_j)\cdot\mathbf{e}_n$ and $g^t_{i,j} = (\mathbf{u}_i - \mathbf{u}_j)\cdot\mathbf{e}_t$ and the corresponding $g^n_{j,i} = -g^n_{i,j}$ and $g^n_{j,i} = -g^t_{i,j}$, where $\{\mathbf{e}_n, \mathbf{e}_t\}$ is a local frame associated to Γ. The following mixed boundary conditions at the interface are assumed:

$$\begin{cases} \mathbf{P}.\mathbf{N}_{i,j} + \mathbf{T}_{i,j} &= \mathbf{0} \\ \mathbf{P}.\mathbf{N}_{i,j} + \mathbf{T}_{j,i} &= \mathbf{0} \end{cases} \text{ on } \quad \Gamma, \tag{6.1.1}$$

where $\mathbf{T} = \mathbf{T}_{i,j} = -\mathbf{T}_{j,i}$ is the cohesive traction. Decomposing the traction on the local frame $\{\mathbf{e}_n, \mathbf{e}_t\}$ we have $\mathbf{T} = T^n\mathbf{e}_n + T^t\mathbf{e}_t$ The normal component of traction is:

$$T^n_{i,j} = \begin{cases} \varepsilon g^n_{i,j}, & \text{if } g^n_{i,j} < 0 \\ T_{n,max}\left(\dfrac{g^n_{i,j}}{g_{n,max}}\right), & \text{if } 0 < g^n_{i,j} < 1 \\ 0, & \text{if } g^n_{i,j} > 1 \end{cases}, \tag{6.1.2}$$

and the tangential component of traction is:

$$T^t_{i,j} = -\mu \tanh\left(\frac{g^t_{i,j}}{a_t}\right)|T^n_{i,j}|. \tag{6.1.3}$$

The electric variables solution respectively of the left and right problem are v_i, w_i and v_j, w_j. The following Robin mixed boundary conditions are assumed (CIY01):

$$\begin{cases} \mathbf{D}\dfrac{\partial v}{\partial \mathbf{n}_{i,j}} + D^n(v_i - v_j) = 0 \\ \mathbf{D}\dfrac{\partial v}{\partial \mathbf{n}_{j,i}} + D^n(v_j - v_i) = 0 \end{cases} \quad \text{on} \quad \Gamma. \tag{6.1.4}$$

The phenomenological constitutive law for the diffusivity across the boundary D^n is given by:

$$D^n_{i,j} = a_1 + a_2\left(\frac{1}{1 + e^{-a_3 - a_4\Delta v_{i,j}}} - \frac{1}{1 + e - a_3 + a_4\Delta v_{i,j}}\right) \tag{6.1.5}$$

and $a_1 = 0.2225, a_2 = 0.8, a_3 = 5, a_4 = 4.25$ and $\Delta v_{i,j} = |v_i - v_j|$.

A Structure-Structure interaction solution strategy is adopted to solve this problem. From the numerical viewpoint this leads to the definition of two variational problems, one for each structure, describing the coupled electro-mechanical problem for the singular cell. At the interface between cells are assumed mixed Robin boundary conditions for electrical voltage and mechanical transduction. In Fig. 48 is shown the evolution of the deformed domains and of the electric potential v passing from the left to the right myocyte.

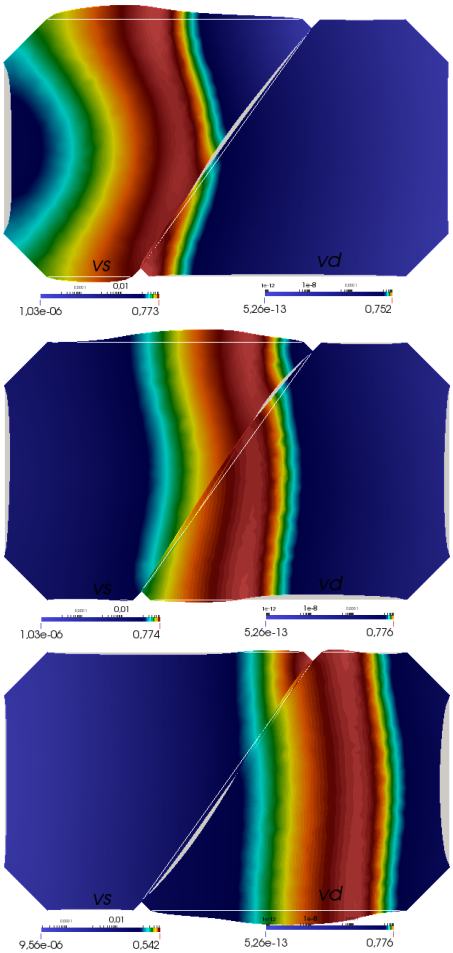

Figure 48: Evolution of the deformed domains Ω_l and Ω_r ad of the transmembrane potential v for different times $t = 342, t = 486, t = 661$.

Appendix A

The expression of the matrices entering the discretized weak forms (3.3.4) and (3.3.5) are:

$$[M_e^{uu}]_{aIbJ} = \int_{R_e} \rho \Phi_b \Phi_a \mathrm{d}V \tag{A.0.1a}$$

$$[K_e^{uu}]_{aIbK} = \int_{R_e} C_{IJKL} \frac{\partial \Phi_b}{\partial x_L} \frac{\partial \Phi_a}{\partial x_J} \mathrm{d}V \tag{A.0.1b}$$

$$[K_e^{u\theta}]_{abK} = \int_{R_e} \Phi_a \beta \delta_{KL} \frac{\partial \Phi_b}{\partial x_L} \mathrm{d}V \tag{A.0.1c}$$

$$\{F_e^u\}_{aI} = \int_{\partial R_e} t_I^* \Phi_a \mathrm{d}A \tag{A.0.1d}$$

$$[M_e^{\theta\theta}]_{ab} = \int_{R_e} \rho c \Phi_b \Phi_a \mathrm{d}V \tag{A.0.1e}$$

$$[K_e^{\theta\theta}]_{ab} = \int_{R_e} k \frac{\partial \Phi_a}{\partial x_L} \frac{\partial \Phi_b}{\partial x_L} \mathrm{d}V \tag{A.0.1f}$$

$$[C_e^{\theta u}]_{bKa} = -\int_{R_e} T_0 \beta \delta_{KL} \frac{\partial \Phi_b}{\partial x_L} \Phi_a \mathrm{d}V \tag{A.0.1g}$$

$$\{F_e^\theta\}_a = \int_{\partial R_e} q^* \Phi_a \mathrm{d}A \tag{A.0.1h}$$

for $1 \leq a, b \leq N$ and $1 \leq I, J, K \leq 3$. The vector $\{f_e^u\}$ and $\{f_e^\theta\}$ in

components read:

$$\{f_e^u\}_{bK} = -\int_{S_e} t_J([[U_L]], \langle\Theta\rangle)\Psi_a\Delta_{aJbK}\mathrm{d}A \tag{A.0.2a}$$

$$\{f_e^\theta\}_b = \int_{S_e} q([[U_L]], \langle\Theta\rangle)\Psi_a\Delta_{ab}\mathrm{d}A \tag{A.0.2b}$$

for $1 \leq b \leq 2S$ and $1 \leq K \leq 3$ where it is remarkable to note that $[C_e^{\theta u}] = -T_0[K_e^{u\theta}]^T$. The expression of the matrices in (3.3.6) are:

$$[K_e] = [P]^T \begin{bmatrix} [K_e^{uu}] & [K_e^{u\theta}] \\ 0 & [K_e^{\theta\theta}] \end{bmatrix} [P] \tag{A.0.3a}$$

$$[C_e] = [P]^T \begin{bmatrix} 0 & 0 \\ [C_e^{\theta u}] & [C_e^{\theta\theta}] \end{bmatrix} [P] \tag{A.0.3b}$$

$$[M_e] = [P]^T \begin{bmatrix} [M_e^{uu}] & 0 \\ 0 & 0 \end{bmatrix} [P] \tag{A.0.3c}$$

$$\{F_e\} = [P]^T \begin{pmatrix} \{F_e^u\} \\ \{F_e^\theta\} \end{pmatrix} \tag{A.0.3d}$$

$$\{f_e\} = [P]^T \begin{pmatrix} \{f_e^u\} \\ \{f_e^\theta\} \end{pmatrix} \tag{A.0.3e}$$

The matrices entering the discretized weak form related to moisture diffusion have the following expression:

$$[B_e]_{ab} = \int_{S_e} D\frac{\partial\Psi_a}{\partial x_I}\frac{\partial\Psi_b}{\partial x_I}\mathrm{d}A \tag{A.0.4a}$$

$$[A_e]_{ab} = \int_{S_e} \Psi_a\Psi_b\mathrm{d}A \tag{A.0.4b}$$

The components of the tangent operator in Eq.(3.4.9) are:

$$\begin{aligned} \left[\frac{\partial\{f_e^u\}_{aI}}{\partial\{U_e\}_{bK}}\right]_{(k)}^{n+1} &= \left[-\frac{\partial}{U_{bK}}\int_{S_e} t_J\Psi_a\Delta_{aJbK}\mathrm{d}A\right]_{(k)}^{n+1} = \\ -\int_{S_e}\Psi_c\Delta_{cLbK}&\left[\frac{\partial t_J}{\partial[[U_L]]}\right]_{(k)}^{n+1}\Psi_a\Delta_{aJbK}\mathrm{d}A \end{aligned} \tag{A.0.5}$$

$$\begin{aligned} \left[\frac{\partial\{f_e^u\}_{aI}}{\partial\{\Theta_e\}_b}\right]_{(k)}^{n+1} &= \left[-\frac{\partial}{\Theta_b}\int_{S_e} t_J\Psi_a\Delta_{aJbK}dA\right]_{(k)}^{n+1} = \\ -\int_{S_e}\Psi_k M_{kb}&\left[\frac{\partial t_J}{\partial\langle\Theta\rangle}\right]_{(k)}^{n+1}\Psi_a\Delta_{aJbK}\mathrm{d}A \end{aligned} \tag{A.0.6}$$

$$\left[\frac{\partial\{f_e^\theta\}_a}{\partial\{\Theta_e\}_b}\right]_{(k)}^{n+1} = \left[\frac{\partial}{\Theta_b}\int_{S_e} q\Psi_d\Delta_{da}\mathrm{d}A\right]_{(k)}^{n+1} = \int_{S_e}\Psi_k M_{kb}\left[\frac{\partial q}{\partial\langle\Theta\rangle}\right]_{(k)}^{n+1}\Psi_d\Delta_{da}\mathrm{d}A \tag{A.0.7}$$

and

$$\left[\frac{\partial\{f_e^\theta\}_a}{\partial\{U_e\}_{bI}}\right]_{(k)}^{n+1} = \left[\frac{\partial}{U_{bI}}\int_{S_e} q\Psi_d\Delta_{da}dA\right]_{(k)}^{n+1} = \int_{S_e}\Psi_i\Delta_{iLbI}\left[\frac{\partial q}{\partial[[U_L]]}\right]_{(k)}^{n+1}\Psi_d\Delta_{da}\mathrm{d}A \tag{A.0.8}$$

where:

$$\left[\frac{\partial t_J}{\partial[[U_L]]}\right] = \begin{bmatrix} K_1(t,\langle\Theta\rangle)\chi_1 & 0 & 0 \\ 0 & K_2(t,\langle\Theta\rangle)\chi_2 & 0 \\ 0 & 0 & K_3(t,\langle\Theta\rangle)\chi_3 \end{bmatrix} \tag{A.0.9a}$$

$$\left[\frac{\partial t_I}{\partial\langle\Theta\rangle}\right] = \frac{\partial}{\partial\langle\Theta\rangle}(K_I(t,\langle\Theta\rangle))\chi_I \tag{A.0.9b}$$

$$\left[\frac{\partial q}{\partial\langle\Theta\rangle}\right] = -k_0\left(1-\frac{[[U_3]]}{\delta_3^c}\right)\chi_3 \tag{A.0.9c}$$

$$\left[\frac{\partial q}{\partial[[U_L]]}\right] = \begin{pmatrix} 0 \\ 0 \\ -k_0\left(1-\dfrac{1}{\delta_3^c}\right)\langle\Theta\rangle\ \chi_3 \end{pmatrix} \tag{A.0.9d}$$

χ_I $(1 \le I \le 3)$ being the characteristic function such that $\chi_I = \chi_{\{[[U_I]]\in J_I\}}$.

$[M]_{ab}$ for $(1 \le a \le S(e), 1 \le b \le 2S(e))$ is the mean operator computing the average temperature across the EVA layer, i.e.:

$$[M_e]_{ab}\Theta_b = \langle\Theta_b\rangle\,. \tag{A.0.10}$$

References

[61215] IEC 61215:2005. Crystalline silicon terrestrial photovoltaic (PV) modules-Design qualification type and approval. *International Electrochemical Commission*, 2015. 40, 58, 60, 61, 82, 126

[Ac13] S. Kaya A. Çibik. Finite element analysis of a projection-based stabilization method for the Darcy-Brinkman equations in double-diffusive convection. *Appl. Numer. Math.*, 64:35–49, 2013. 9, 104

[AE03] Klas Adolfsson and Mikael Enelund. Fractional derivative viscoelasticity at large deformations. *Nonlinear Dynamics*, 33(3):301–321, 2003. 13

[AQ03] A. Veneziani A. Quarteroni. Analysis of a geometrical multiscale model based on the coupling of ODE and PDE for blood flow simulations. *Multiscale Modeling & Simulation*, 1(2):173–195, 2003. 42

[AS02] L. Gaul A. Schmidt. Finite element formulation of viscoelastic constitutive equations using fractional time derivatives. *Nonlinear Dynamics*, 29(1):37–55, 2002. 7, 13, 25

[Bag91] Ronald L. Bagley. The thermorheologically complex material. *International Journal of Engineering Science*, 29(7):797–806, 1991. 5, 13, 17

[Bow09] Allan F. Bower. *Applied Mechanics of Solids*. CRC Press, 1 edition, 2009. 5, 12, 14

[BR] P. Carstensen B. RAnby. Free radicals in polyolefins initiated with ultraviolet and ionising radiation. *Irradiation of polymers*, 18. 69

[BR08] G. Van Assche T. Artoos B. Van Mele B. Rimez, H. Rahier. The thermal degradation of poly(vinyl acetate) and poly(ethylene-co-vinyl acetate), Part II: Modelling the degradation kinetics, Polymer Degradation and Stability. *Solar Energy Materials and Solar Cells*, 93:1222–1230, 2008. 68

[Bri08] H. F Brinson; L. C. Brinson. *Polymer engineering science and viscoelasticity : an introduction*. Springer, 2008. 15

[CBW14] J.P. Whiteley C.G. Bell, H.M. Byrne and S.L. Waters. Heat or mass transfer at low Péclet number for Brinkman and Darcy flow round a sphere. *Int. J. Heat Mass Transf.*, 68:247–258, 2014. 9

[CFG12] C. Cherubini, S. Filippi, and A. Gizzi. Electroelastic unpinning of rotating vortices in biological excitable media. *Phys. Rev. E*, 85, 2012. 129, 130

[Chr13] R.M. Christensen. *Theory of Viscoelasticity: Second Edition*. Dover Civil and Mechanical Engineering. Dover Publications, 2013. 5, 6, 16

[CIY01] Spangler R.A. Chen-Izu Y., Moreno A.P. Opposing gates model for voltage gating of gap junction channels. *AMERICAN JOURNAL OF PHYSIOLOGY-CELL PHYSIOLOGY*, 281(5):C1604–C1613, 2001. 130, 131

[C.L01] E. Hernández-García P.H. Haynes C.López, Z. Neufeld. Chaotic advection of reacting substances: Plankton dynamics on a meandering jet . *Phys. Chem. Earth B*, 26:313, 2001. 9

[DLWZ15] Anxin Ding, Shuxin Li, Jihui Wang, and Lei Zu. A three-dimensional thermo-viscoelastic analysis of process-induced residual stress in composite laminates. *Composite Structures*, 129:60 – 69, 2015. 13

[EEB15] M. A. Ezzat and A. A. El-Bary. Memory-dependent derivatives theory of thermo-viscoelasticity involving two-temperature. *Journal of Mechanical Science and Technology*, 29(10):4273–4279, 2015. 22

[EL99] Mikael Enelund and George A. Lesieutre. Time domain modeling of damping using anelastic displacement fields and fractional calculus. *International Journal of Solids and Structures*, 36(29):4447 – 4472, 1999. 13, 14

[EU10] Köntges M. Brendel R. Eitner U., Kajari-schröder S. Non-linear mechanical properties of ethylene-vinyl acetate (eva) and its relevance to thermomechanics of photovoltaic modules. In *25th European Photovoltaic Solar Energy Conference, Valencia, Spain, 6–10 September 2010, 4AV.3.115*, 2010. 5, 12, 14

[FA92] T.A. Egerton J.R. White F. Armero, J.C. Simo. A new unconditionally stable fractional step method for non-linear coupled thermomechanical problems. *Int. J. Numer. Meth. Eng.*, 35(4):737–766, 1992. 1, 3

[Fab14] Mauro Fabrizio. Fractional rheological models for thermomechanical systems. dissipation and free energies. *Fractional Calculus and Applied Analysis*, 17(1):206–223, 2014. 13

[FL02] Alan D. Freed and Arkady I. Leonov. A thermodynamic theory of solid viscoelasticity. part 1: Linear viscoelasticity. 2002. 14

[FN14a] D. David D.C. Dauskardt F.D. Novoa, D.C. Miller. Environmental mechanisms of debonding in photovoltaic backsheets. *Solar Energy Materials and Solar Cells*, 120(A):87–93, 2014. 63, 64

[FN14b] D. David DC.. Dauskardt F.D. Novoa, D.C. Miller. Environmental mechanisms of debonding in photovoltaic backsheets. *Energy Mater. Sol. C*, 120(A):87–93, 2014. 68

[FP92] A.W. Czanderna F.J. Pern. Characterization of ethylene vinyl acetate (EVA) encapsulant: Effects of thermal processing and weathering degradation on its discoloration. *Solar Energy Materials and Solar Cells*, 25:(1-2):3–23, 1992. 68

[FW52] John D Ferry and Malcolm L Williams. Second approximation methods for determining the relaxation time spectrum of a viscoelastic material. *Journal of Colloid Science*, 7(4):347 – 353, 1952. 17

[GA15] M. Musto G. Alfano. A fractional rate-dependent cohesive-zone model. *International Journal for Numerical Methods in Engineering*, 52:1039–1058, 2015. 42

[Gat14] Gabriel N. Gatica. *A Simple Introduction to the Mixed Finite Element Method: Theory and Applications*. SpringerBriefs in Mathematics. Springer International Publishing, 1 edition, 2014. 10

[GC14] V. Franzitta M. Trapanese G. Ciulla, V. Lo Brano. Assessment of the Operating Temperature of Crystalline PV Modules Based on Real Use Conditions. *International Journal of Photoenergy*, page 11, 2014. 77

[Gei11] Juergen Geiser. *Iterative Splitting Methods for Differential Equations*. Chapman and Hall/CRC Numerical Analysis and Scientific Computing Series. Chapman and Hall/CRC, 2011. 1, 3

[GFA10] M.E. Gurtin, E. Fried, and L. Anand. *The Mechanics and Thermodynamics of Continua*. Cambridge University Press, 2010. 4, 6

[GM10] Saprunov B. Emri I. Gergesova M., Zupani B. The closed form ttp shifting (cfs) algorithm. *Journal of Rheology*, 55(1), 2010. 5, 14

[GN94] W. G. Glöckle and T. F. Nonnenmacher. Fractional relaxation and the time-temperature superposition principle. *Rheologica Acta*, 33(4):337–343, 1994. 5, 14, 16

[HA13] J. Azaiez H. Alhumade. Reversible reactive flow displacements in homogeneous porous media. *Proc. WCE*, pages 1–6, 2013. 9

[HP96] A.J. Hillesdon and T.D. Pedley. Bioconvection in suspensions of oxytactic bacteria: linear theory. *J. Fluid Mech.*, 324:223–259, 1996. 9, 112

[HS96] Gerhard A. Holzapfel and Juan C. Simo. A new viscoelastic constitutive model for continuous media at finite thermomechanical changes. *International Journal of Solids and Structures*, 33(20):3019 – 3034, 1996. 14

[JD83] M.F. Wheeler J.R. Douglas, R. Ewing. The approximation of the pressure by a mixed method in the simulation of miscible displacement. *RAIRO Anal. Numér.*, 17:17–33, 1983. 89

[JK13a] R. Jecl L. Škerget J. Kramer, J. Ravnik. Three-dimensional double-diffusive natural convection with opposing buoyancy effects in porous enclosure by boundary element method. *Int. J. Comput. Methods Exp. Meas.*, 1(2):103–115, 2013. 9, 113

[JK13b] R. Jecl L. Škerget J. Kramer, J. Ravnik. Three-dimensional double-diffusive natural convection with opposing buoyancy effects in porous enclosure by boundary element method. *Int. J. Comput. Methods Exp. Meas.*, 1(2):103–115, 2013. 9, 107

[Kem06] M.D. Kempe. Modeling of rates of moisture ingress into photovoltaic modules. *Solar Energy Materials & Solar Cells*, 90:2720–2738, 2006. 68, 69

[Kem14] D. Kempe. Modeling of rates of moisture ingress into photovoltaic modules. *Solar Energy Materials and Solar Cells*, 90(16):2720–2738, 2014. 8, 41, 49, 60, 61, 62, 63, 65

[KF12] Samer Wehbe Katicha and G. W. Flintsch. Fractional viscoelastic models: master curve construction, interconversion, and numerical approximation. *Rheologica Acta*, 51(8):675–689, 2012. 16

[KM12] Kamran A. Khan and Anastasia H. Muliana. Fully coupled heat conduction and deformation analyses of nonlinear viscoelastic composites. *Composite Structures*, 94(6):2025–2037, 2012. 22

[Koe84] R.C. Koeller. Application of fractional calculus to the theory of viscoelasticity. *J. Appl. Mech.*, 51:229–307, 1984. 13

[LP94] E.J. Fernandez L.D. Plante, P.M. Romano. Viscous fingering in chromatography visualized via magnetic resonance imaging. *Chem. Engrg. Sci.*, 49(14):2229–2241, 1994. 9

[LP00] J.C. Song L.E. Payne. Spatial decay for a model of double-diffusive convection in Darcy and Brinkman flows. *Z. Angew. Math. Phys.*, 51:867–880, 2000. 9

[LR04] N.N. Kolesnikova G.E. Zaikov L.V. Ruban, O.V. Sychugova. Kinetic features of the nonisothermal oxidative degradation of ethylene vinyl acetate copolymers. *Journal of Applied Polymer Science*, 91:1958–1961, 2004. 70

[Mai10] F. Mainardi. An Introduction to Mathematical Models. *Imperial College Press, London, UK*, 2010. 5, 7, 13, 16, 25, 41, 47

[MDP11] A. Valenza M. Di Paola, A. Pirrotta. Visco-elastic behavior through fractional calculus: An easier method for best fitting experimental results. *Mechanics of Materials*, 43:799–806, 2011. 5, 13, 25, 41

[MDP13] M. Zingales M. Di Paola, F.P. Pinnola. A discrete mechanical model of fractional hereditary materials. *Meccanica*, 48:1573–1586, 2013. 5, 41, 47

[MM97] D.A. Vasquez M. Marlow, Y. Sasaki. Spatiotemporal behavior of convective Turing patterns in porous media . *J. Chem. Phys.*, 107(13):5205–5211, 1997. 9

[MML12] Aratyn-Schaus Y. et al. McCain M. L., Lee H. Cooperative coupling of cell-matrix and cell-cell adhesions in cardiac muscle. *PROCEEDINGS OF THE NATIONAL ACADEMY OF SCIENCES OF THE UNITED STATES OF AMERICA*, 109(25):9881–9886, 2012. 130

[MP11] U. Eitner M. Paggi, S. Kajari-Schörder. Thermomechanical deformations in photovoltaic laminates. *Advanced Structured Materials*, 46:772–782, 2011. 40, 62

[MP15] A. Sapora M. Paggi. An accurate thermoviscoelastic rheological model for ethylene vinyl acetate based on fractional calculus. *International Journal of Photoenergy, article:7*, 2015. 13, 14, 15, 17, 19, 35, 37, 41, 47, 62

[MVI12] J.-F. Penneau N. Chatagnon D. Binesti M. V. Iseghem, A. Plotton. Failure modes after damp heat tests on PV modules. *Proceedings of 27th European Photovoltaic Solar Energy Conference and Exhibition*, pages 3546–3548, 2012. 40

[Nor10] Norrish Type II Reaction (Norrish Type II Process, Norrish Type II Photoreaction, Yang Cyclization). 465:2067–2071, 2010. 70

[Now86] W. Nowacki. *Thermoelasticity*. Pergamon Press, 1986. 4, 43

[NQRB12] F. Nobile, A. Quarteroni, and R. Ruiz-Baier. An active strain electromechanical model for cardiac tissue. *International Journal for Numerical Methods in Biomedical Engineering*, 28(1):52–71, 2012. 128, 129

[PDS+11] M. Pander, S. Dietrich, S. H. Schulze, U. Eitner, and M. Ebert. Thermo-mechanical assessment of solar cell displacement with respect to the viscoelastic behaviour of the encapsulant. In *2011 12th Intl. Conf. on Thermal, Mechanical Multi-Physics Simulation and Experiments in Microelectronics and Microsystems*, pages 1–6, April 2011. 5, 12, 14, 17

[Per96] F.J. Pern. Factors that affect the EVA encapsulant discoloration rate upon accelerated exposure. *Solar Energy Materials and Solar Cells*, 41:587–615, 1996. 68

[Per97] F.J. Pern. Ethylene vinyl acetate (EVA) encapsulants for photovoltaic modules: degradation and discoloration mechanisms and formulation of improved photostability. *Die Angewandte Makromolekulare Chemie*, 252(4523):195–216, 1997. 68

[PH15] K.A. Weiss P. Hlsmann. Simulation of water ingress into PV-modules: IEC-testing versus outdoor exposure. *Solar Energy*, 115:347–353, 2015. 69

[Pip12] A.C. Pipkin. *Lectures on Viscoelasticity Theory*. Applied Mathematical Sciences. Springer New York, 2012. 16

[PL16] M. Paggi P. Lenarda. A geometrical multi-scale numerical method for coupled hygro-thermo-mechanical problems in photovoltaic laminates. *Comput Mech.*, 57:947–963, 2016. 68

[QSM16] A. Younes Q. Shao, M. Fahs and A. Makradi. A high-accurate solution for Darcy-Brinkman double-diffusive convection in saturated porous media. *Numer. Heat Transfer B*, 69(1):26–47, 2016. 9, 104, 107

[RB13] M. Kaliske R. Behnke, R. Fleischhauer. A thermomechanical interface element formulation for finite deformations. *Computational Mechanics*, 52:1039–1058, 2013. 8, 42

[RE80] M.F. Wheeler R. Ewing. Galerkin methods for miscible displacement problems in porous media. *SIAM J. Numer. Anal.*, 17:351–365, 1980. 89

[RS11] Y. T. H. Jianfei R. Scherer, S. L. Kalla. The grünwaldletnikov method for fractional differential equations. *Comp. Math. Appl.*, 62(3):902–917, 2011. 7, 25

[RY10] T.A. Egerton J.R. White R. Yang, P.A. Christensen. Degradation products formed during UV exposure of polyethylene-ZnO nanocomposites. *Solar Energy*, 95(9):1533–1541, 2010. 70

[She04] The theory of generalized thermoelastic diffusion. *International Journal of Engineering Science*, 42(56):591– 608, 2004. 4, 6

[SK04] A. De Wit S. Kalliadasis, J. Yang. Fingering instabilities of exothermic reaction-diffusion fronts in porous media. *J. Fluid Mech.*, 16(5):1395–1409, 2004. 9

[SMH11] R. K. Saxena, A. M. Mathai, and H. J. Haubold. Mittag-leffler functions and their applications. *Journal of Applied Mathematics*, 2011(298628), 2011. 14, 16

[UE11] M. Köntges H. Altenbach U. Eitner, S. Kajari-Schröder. Thermal stress and strain of solar cells in photovoltaic modules. *Advanced Structured Materials*, 15:453–468, 2011. 17, 40

[VA16] D. Mora R. Ruiz-Baier V. Anaya, M. Bendahmane. On a primal-mixed vorticity-based formulation for reaction-diffusion-Brinkman systems. *in preparation*, 2016. 9

[VARB16] D. Mora V. Anaya and R. Ruiz-Baier. Pure vorticity formulation and Galerkin discretization for the Brinkman equations. *IMA J. Numer. Anal.(in preparation)*, 2016. 89, 90, 93

[Voi14] T. Voigtmann. Nonlinear glassy rheology. *Current Opinion in Colloid and Interface Science*, 19(6):549 –560, 2014. 17

[WS01] Zhang Wei and Nobuyuki Shimizu. Fe formulation for the viscoelastic body modeled by fractional constitutive law. *Acta Mechanica Sinica*, 17(4):354–365, 2001. 25

Unless otherwise expressly stated, all original material of whatever nature created by Pietro Lenarda and included in this thesis, is licensed under a Creative Commons Attribution Noncommercial Share Alike 2.5 Italy License.

Check creativecommons.org/licenses/by-nc-sa/2.5/it/ for the legal code of the full license.

Ask the author about other uses.